Monte Carlo Dose Calculations in Advanced Radiotherapy

by

Karl Kenneth Bush
B.Sc., University of Victoria, 2003
M.Sc., University of Victoria, 2006

A Dissertation Submitted in Partial Fulfillment of the
Requirements for the Degree of

DOCTOR OF PHILOSOPHY

in the Department of Physics and Astronomy

University of Victoria

Monte Carlo Dose Calculations in Advanced Radiotherapy

by

Karl Kenneth Bush
B.Sc., University of Victoria, 2003
M.Sc., University of Victoria, 2006

Supervisory Committee

Dr. S. Zavgorodni, Co-Supervisor (Department of Physics and Astronomy)

Dr. A. Jirasek, Co-Supervisor (Department of Physics and Astronomy)

Dr. W. Beckham, Member (Department of Physics and Astronomy)

Dr. M. Lefebvre, Member (Department of Physics and Astronomy)

Dr. M. Adams, Member (Department of Electrical and Computer Engineering)

Supervisory Committee

Dr. S. Zavgorodni, Co-Supervisor

Dr. A. Jirasek, Co-Supervisor

Dr. W. Beckham, Member

Dr. M. Lefebvre, Member

Dr. M. Adams, Member

Abstract

The remarkable accuracy of Monte Carlo (MC) dose calculation algorithms has led to the widely accepted view that these methods should and will play a central role in the radiotherapy treatment verification and planning of the future. The advantages of using MC clinically are particularly evident for radiation fields passing through inhomogeneities, such as lung and air cavities, and for small fields, including those used in today's advanced intensity modulated radiotherapy techniques. Many investigators have reported significant dosimetric differences between MC and conventional dose calculations in such complex situations, and have demonstrated experimentally the unmatched ability of MC calculations in modeling charged particle disequilibrium. The advantages of using MC dose calculations do come at a cost. The nature of MC dose calculations require a highly detailed, in-depth representation of the physical system (accelerator head geometry/composition, anatomical patient geometry/composition and particle interaction physics) to allow accurate modeling of external beam radiation therapy treatments. To perform such simulations is computationally demanding and has only recently become feasible within mainstream radiotherapy practices. In addition, the output of the accelerator head simulation can be highly sensitive to inaccuracies within a model that may not be known with sufficient detail.

The goal of this dissertation is to both improve and advance the implementation of MC dose calculations in modern external beam radiotherapy. To begin, a novel method is proposed to fine-tune the output of an accelerator model to better represent the measured output. In this method an intensity distribution of the electron beam incident on the model is inferred by employing a simulated annealing algorithm. The method allows an investigation of arbitrary electron beam intensity distributions and is not restricted to the commonly assumed Gaussian intensity.

In a second component of this dissertation the design, implementation and evaluation of a technique for reducing a latent variance inherent from the recycling of phase space particle tracks in a simulation is presented. In the technique a random azimuthal rotation about the beam's central axis is applied to each recycled particle, achieving a significant reduction of the latent variance.

In a third component, the dissertation presents the first MC modeling of Varian's new RapidArc delivery system and a comparison of dose calculations with the Eclipse treatment planning system. A total of four arc plans are compared including an oropharynx patient phantom containing tissue inhomogeneities.

Finally, in a step toward introducing MC dose calculation into the planning of treatments such as RapidArc, a technique is presented to feasibly generate and store a large set of MC calculated dose distributions. A novel 3-D dyadic multi-resolution (MR) decomposition algorithm is presented and the compressibility of the dose data using this algorithm is investigated. The presented MC beamlet generation method, in conjunction with the presented 3-D data MR decomposition, represents a viable means to introduce MC dose calculation in the planning and optimization stages of advanced radiotherapy.

Table of Contents

List of Tables

List of Figures

Abbreviations and Acronyms

AAA	Anisotropic Analytical Algorithm
AAPM	American Association of Physicists
AE	Electron Cutoff Energy for Explicit Electron Interaction Modeling
AKDE	Adaptive Kernel Density Estimation
AP	Photon Cutoff Energy for Explicit Photon Interaction Modeling
APR	Azimuthal Particle Recycling
ASCII	American Standard Code for Information Interchange
CAX	Central Axis
CC	Collapsed Cone
CH	Condensed History
CM	Component Module
CPU	Central Processing Unit
c.s.	Coordinate System
CSDA	Continuous Slowing Down Approximation
CT	Computed Tomography
CTV	Clinical Target Volume
DBS	Directional Bremsstrahlung Splitting
DICOM	Digital Imaging and Communications in Medicine
$\mathbf{d}_{MAX}$	Depth of Maximum Dose
dMLC	Dynamic Multi-Leaf Collimator

DNA	Deoxyribonucleic Acid
DVH	Dose Volume Histogram
ECUT	Electron Cutoff Energy
EGS	Electron Gamma Shower
EPID	Electronic Portal Imaging Device
ETE	Estimated Trial and Error
FWHM	Full Width Half Maximum
GB	Gigabyte
GTV	Gross Tumor Volume
IEC	International Electrotechnical Commission
IMAT	Intensity Modulated Arc Therapy
IMRT	Intensity Modulated Radiation Therapy
KERMA	Kinetic Energy Released in Material
Linac	Linear Accelerator
MC	Monte Carlo
MERT	Modulated Electron Radiation Therapy
MIMiC	Multileaf Intensity Modulating Collimator
MLC	Multi-Leaf Collimator
MU	Monitor Units
NCI	National Cancer Institute
NRC	National Research Counsil
NRCYCL	Number of Recyclings
NTCP	Normal Tissue Complication Probability
OAR	Organs at Risk
PB	Pencil Beam
PC	Primary Collimator

PCUT Photon Cutoff Energy

PDD Percentage Depth Dose

PDF Probability Density Function

PS$_A$ Phase Space A

PS$_B$ Phase Space B

PSF Phase Space File

PTV Planning Tumor Volume

RMSE Root Mean Square Error

RT Radiation Therapy

SAD Source to Axis Distance

SPR Standard Particle Recycling

SSD Source to Surface Distance

TBI Total Body Irradiation

TCP Tumor Control Probability

TERMA Total Energy Released in Material

TPS Treatment Planning System

UTCP Uncomplicated Tumor Control Probability

VCU Virginia Commonwealth University

VIMC Vancouver Island Monte Carlo

VMAT Volumetric Modulated Arc Therapy

VMC Voxel Monte Carlo

Acknowledgements

I am indebted to my supervisor Dr. Sergei Zavgorodni for his endless dedication toward helping me develop as a student. He has not only helped me achieve my goals but has also given me the confidence to set my goals high. His wealth of knowledge and scientific expertise is astounding to say the least. I seem to walk away from every conversation with Sergei with the guidance and encouragement needed to tackle the problem at hand. Whether in his office or roped up on the side of a mountain I have learned so much from Sergei. It is truly an honour to be his student and friend. I can only hope to one day mentor students in the way that he has mentored me.

I am also indebted to Dr. Wayne Beckham for his role and support throughout my time at the BC Cancer Agency. His leadership inspires all who have the privilege to work with him. The sign of a great leader is someone who is never demanding anything of others yet inspires others to demand greatness from themselves. Wayne is always looking out for the best interests of others and has always encouraged me to pursue my research interests. His depth of experience, logic and professionalism in helping others is astonishing. I am truly thankful to have had the opportunity to work for Wayne.

I would also like to thank cooperative education student Reid Townson for his excellent work on related Monte Carlo projects and Chistopher Locke for his major contributions to software we use so often.

March, 2009 *Karl Bush*
Victoria, BC

Chapter 1

Introduction to External Beam Radiation Therapy

1.1 The Goal of Modern Radiation Therapy

An estimated 39% of Canadian females and 44% of Canadian males will develop cancer during their lifetimes. On average, 1-in-4 Canadians will die of the disease [NCIC, 2009]. Cancer incidence in Canadian men is slowly decreasing (due to a decreasing incidence of lung cancer in men) while cancer incidence rates in Canadian women is slowly increasing (due to an increasing incidence of lung cancer in women). British Columbia maintains the lowest cancer mortality rates in Canada for both men and women with an estimated 20,500 new cases diagnosed and 9,200 deaths from the disease in 2008 [NCIC, 2009]. In approximately half of new cancer cases, external beam radiation therapy (RT) is prescribed. Elevated local tumour control is commonly achieved through the combination of RT with surgical removal of the cancerous material, chemotherapy, immunotherapy, hormone treatments and/or transplantation techniques.

The goal of external beam radiation therapy is to induce the *mitotic death* and/or *apoptosis* of malignant tumour cells through the application of *ionizing radiations* (photon, electron and proton) while minimizing the damage to surrounding normal (healthy) tissues. Mitotic death is commonly believed to occur from irreparable radiation induced damage to the structure of the deoxyribonucleic acid (DNA) backbone of malignant cell nuclei. This damage leads to death occurring during the subsequent division(s) of the cell. *Apoptosis*, the programmed death process of a cell, may also be induced from the ionizing radiation contributing further to tumour cell death. The prognoses for several of the most prevalent histological cancers, when treated with the aim of curing the disease, are presented in Table 1.1. In cases of a terminal prognoses, external beam radiation may also be applied as a *palliative* therapy. In such treatments an irradiation may be delivered to alleviate pain by temporarily suppressing tumour growth.

Table 1.1: Surveillance Epidemiology and End Results (SEER) data for 1, 5 and 10 year survival rates and proportion of occurance for common cancers from 1975 - 2005. [Ries et al., 2007]

Site	Cases	%	Survival Rate (%)		
			1-Year	5-Year	10-Year
			Percent	Percent	Percent
All sites	1,584,884	100.0	79.5	64.4	58.6
Prostate	275,280	17.4	100.0	97.6	91.7
Breast (female, in situ)	44,875	2.8	100.0	100.0	100.0
Breast (female, invasive)	257,888	16.3	97.8	87.1	79.2
Lung	201,067	12.7	42.6	15.5	11.0
Colon/Rectum	182,589	11.5	83.3	63.6	57.7
Melanoma	55,039	3.5	97.1	90.0	87.9
Urinary Bladder	67,528	4.3	91.5	81.9	77.4
Non-Hodgkin Lymphoma	65,932	4.2	74.2	56.3	47.0
Uterine Corpus	48,642	3.1	93.5	84.7	82.6
Leukemia (all ages)	42,678	2.7	67.0	47.2	38.1
Kidney and Renal Pelvis	32,583	2.1	80.8	65.5	57.9

Presently, external photon beams are most commonly used in radiotherapy treatments. Electron beams are often used in the treatment of shallow tumours. Proton beams offer distinct advantages in localizing dose delivery over photon and electron beams but are presently limited in use by the expense of the proton accelerator.

1.2 The Modern Medical Linear Accelerator

An overview of the production of x-rays within a medical linear accelerator (linac) such as that shown in Figure 1.1 will now be presented.

1.2.1 Accelerating Electrons

The acceleration of electrons in the medical linac is achieved through the application of microwaves that have been confined and structured by the use of a waveguide. The input microwaves are generated through use of a klystron and are typically in the 3000 MHz or S-band range (2-4 MHz range)[Karzmark, 1984]. Both traveling wave and standing wave designs are used in medical linac designs although the latter is

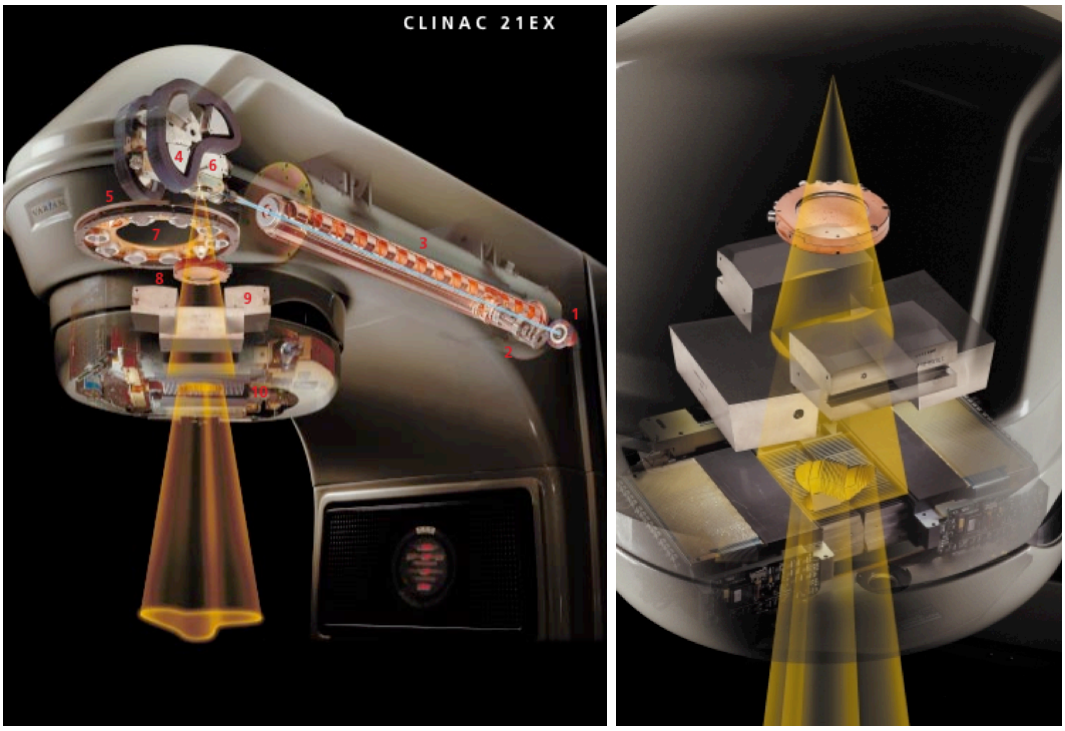

Figure 1.1: The Varian Clinac 21EX accelerator *(left)* and treatment head components *(right)*. [Varian Medical Systems]

more common as of recently due to the compact nature of the design. The accelerator used for the body of research in this dissertation is of standing wave design.

The waveguide implemented in standing wave accelerator design consists of a series of cylindrical accelerating cavities of lengths varying from 2.5 cm to 5.0 cm corresponding to the half wavelengths of the input microwaves (see Figure 1.2). To establish the standing wave both a forward traveling wave and backward traveling wave are arranged, each of which is reflected at the ends of the waveguide. Using this design the moving electric field maxima from each wave are forward aligned 1/4 of the time, reverse aligned 1/4 of the time, and cancel each other out 1/2 the time (zero-field), as shown in Figure 1.3. Because the zero-field cavities do not contribute to particle acceleration it is possible to reposition these cavities off axis, out of the particle path but still able to couple power between adjacent cavities. By doing so the overall length of the accelerator can be significantly reduced. The electric field

directions in a standing wave accelerator with offset zero-field cavities are shown in Figure 1.4. In order to prevent electrical arcing between disks in the waveguide the entire accelerating cavity is kept under vacuum.

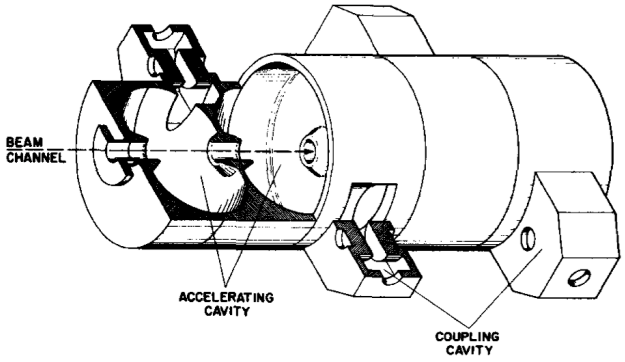

Figure 1.2: A cutout of a medical accelerator waveguide [Karzmark, 1984].

By varying the aperture and length of the cavities initially traversed, the continuum of injected electron velocities, delivered from an electron gun, are concentrated into discrete bunches during the bunching phase of their acceleration. Beyond the bunching phase, the velocity of the electrons remains approximately constant and near the speed of light. The waveguide cavities are therefore made uniform for the remainder of the acceleration period. As bunching technology improves, a greater proportion of the incident electrons are able to be captured and bunched. Current technology allows roughly one third of the incident electrons to be successfully captured, bunched, and accelerated over the length of the waveguide [Karzmark, 1984].

The range of clinically useful photon and electron beam energies is governed by the penetration, or *depth dose*, properties of the beam in water (which can be approximated as human tissue in terms of the attenuation properties) as well as the lateral spread of scattered electrons within a patient. The probability of neutron production in the accelerator head is also a factor in limiting the upper end of clinically useful photon and electron energies. In Figure 1.5, the percentage depth dose

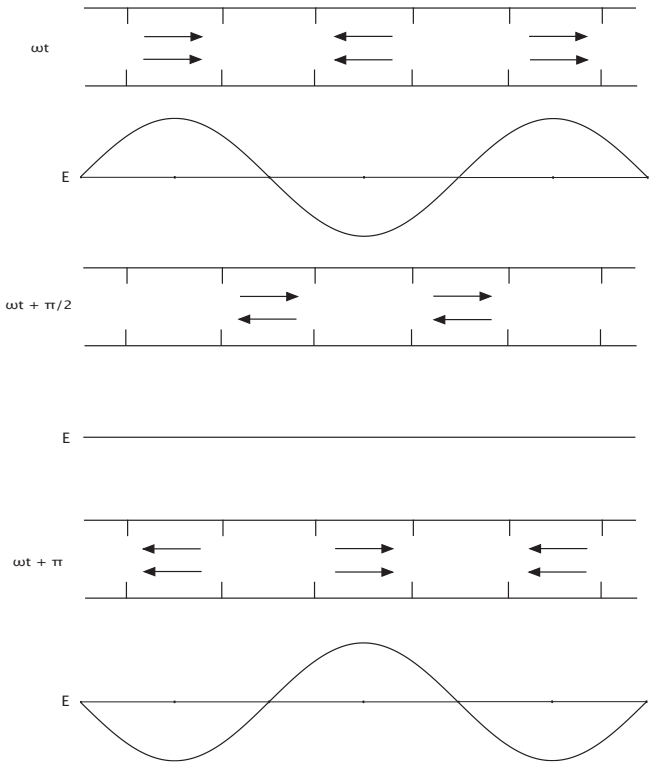

Figure 1.3: A simplified view of the electric field directions in a standing wave accelerator at three different times [Karzmark, 1984].

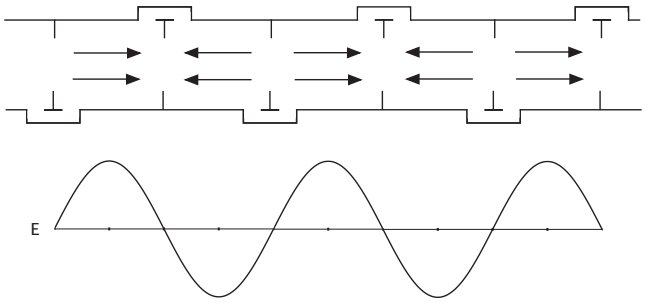

Figure 1.4: A simplified view of the electric field directions in a standing wave accelerator with the zero-field cavities offset [Karzmark, 1984].

(PDD) curves for a selection of photon *(top)* and electron *(bottom)* energies in water are shown. From the upper figure, the motivation for use of photons below 25 MeV becomes apparent as a higher penetration depth delivers unwanted higher doses deep into the patient. The depth of maximum dose deposition (d_{MAX}) also begins to increase beyond that required to reach the tumor volume in a patient of common girth. Using a similar argument, the lower figure can be used to justify the common clinical range for electron beams.

1.2.2 The Production of X-Rays

Electrons emerging from the accelerating waveguide are directed toward the electron target by means of bending and steering magnets. In the case of the Varian Clinac series of accelerators used in this research the electrons are directed 270^o toward the target (see Figure 1.6). The purpose of this is two-fold: to filter out and prevent low energy contaminant electrons from hitting the target, and to allow a more compact accelerator design. In this figure, energy selection slits S1 and S2 are used to limit the range of electron energies able to pass through the bending magnet.

X-rays are produced from the accelerated electron beam predominantly through the *bremsstrahlung* process within a slab of Tungsten placed in the electron beam's path. Tungsten is chosen for both its high atomic number (high-Z) and resistance to heat deformation. The ability to resist heat deformation is important since in a typical Tungsten target only $\sim$1% of the incident electron energy emerges as bremsstrahlung photons. The remaining energy is lost to heat in the target. This heat must be dissipated by the accelerator via the accelerator's cooling system. Copper can be fused to the downstream face of the Tungsten slab and placed in thermal contact with the accelerator's cooling system to aid in heat dissipation and reduce secondary electron production.

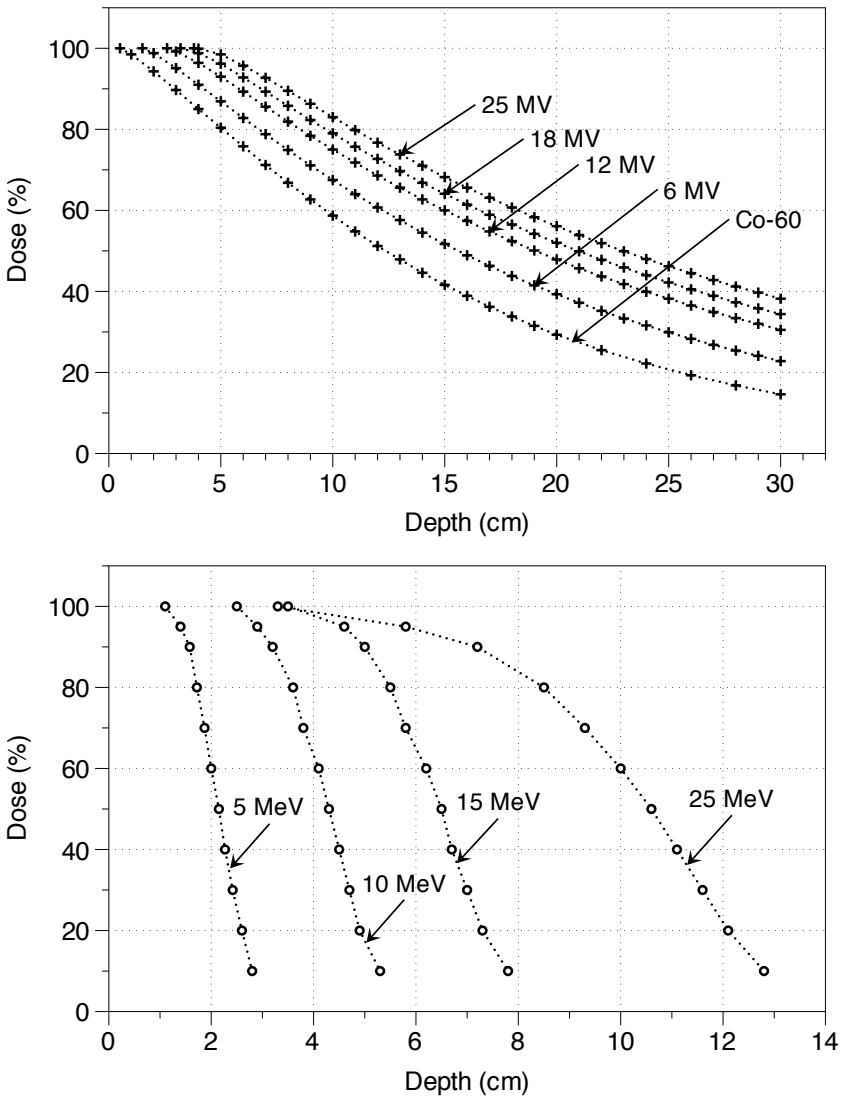

Figure 1.5: Percentage depth dose measurements for a 10.0×10.0 cm^2 field of 25.0 MV, 18.0 MV, 12 MV, 6 MV and Co-60 produced photons in water *(top)*. Percentage depth dose measurements for a 10.0×10.0 cm^2 field of 25.0 MeV, 15.0 MeV, 10.0 MeV and 5.0 MeV electrons in water *(bottom)*. (Data from British Journal of Radiology [Day and Aird, 1996])

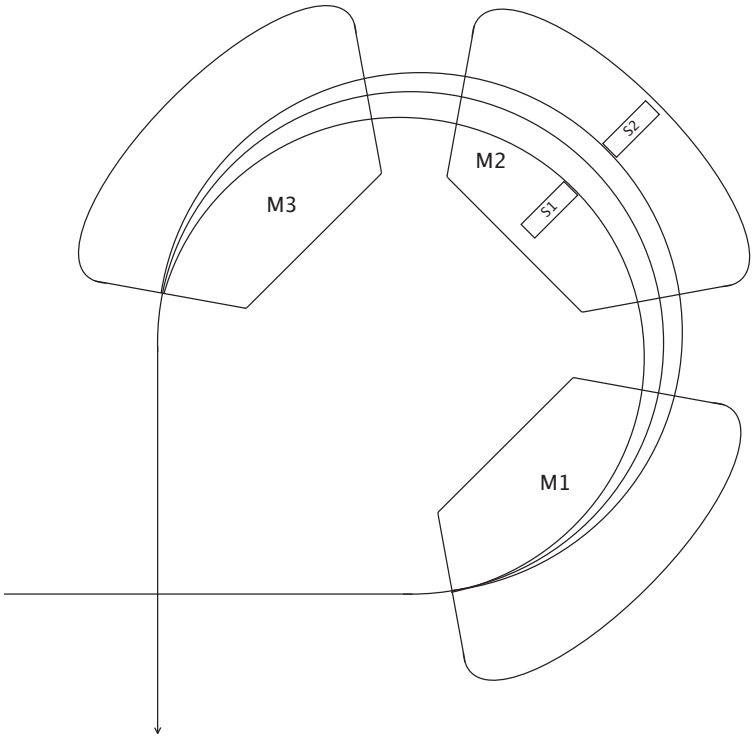

Figure 1.6: Schematic of the 3-piece bending magnet used to redirect the electron beam 270° toward the target. Energy selection slits S1 and S2 can be adjusted radially inward or outward to change the accepted range of electron energies [Karzmark et al., 1992].

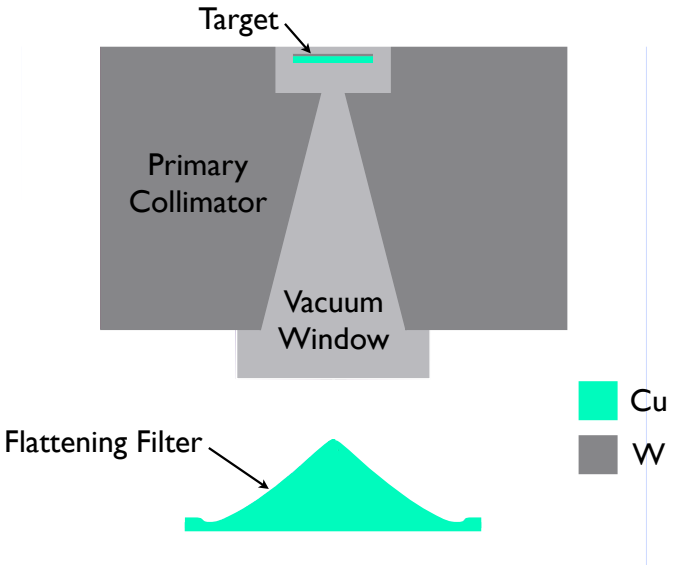

Figure 1.7: Geometry and locations of the electron target (W and Cu fused), primary collimator (W), vacuum window (Be filled) and flattening filter (Cu) for shaping and flattening the 6 MV photon beam within the Clinac 21EX accelerator.

1.2.3 Shaping, Flattening and Monitoring the Beam

Primary collimation of the photons emerging from the bremsstrahlung target is performed using a Tungsten collimator with a conical bore. Photons with trajectories within the bore are free to pass through the collimator unattenuated. The conical beam exiting the primary collimator is cylindrically symmetric about the beam's central axis.

Bremsstrahlung photons emerging from the electron target and primary collimator are highly *forward peaked*, that is, the beam contains a significantly higher intensity of high energy photons directed along the beam's central axis (a product of the angular bremsstrahlung cross-section). The combination of target thickness/composition with flattening filter shape/composition gives rise to the spectral and penetration properties of the beam. A large number of publications have focused on this subject [Larsen et al., 1978; Lane and Paliwal, 1975; Huang et al., 1986; Flock and Shragge, 1987; Constantinou and Sternick, 1984; Boge et al., 1975; Nordell and Brahme, 1984;

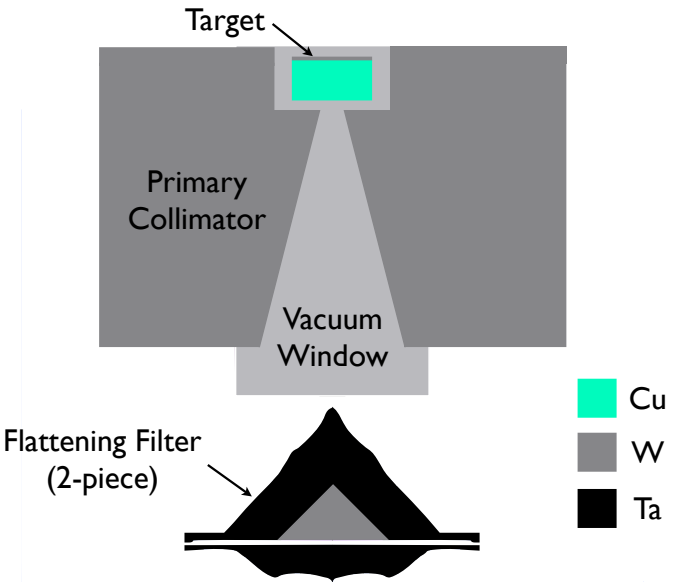

Figure 1.8: Geometry and locations of the electron target (W and Cu fused), primary collimator (W), vacuum window (Be filled) and flattening filter (Steel with Tantalum core) for shaping and flattening the 18 MV photon beam within the Clinac 21EX accelerator. A thicker slab of Copper is fused to the target to increase heat dissipation for the additional heating from the higher energy electrons.

Podgorsak et al., 1974, 1975; Reinstein and Orton, 1981; Taumann, 1981]. When designing the ideal combination of target and filter one must consider many factors including, most importantly, the clinical effectiveness/usefulness of the beam. Factors of clinical importance include the absorbed skin/surface dose contribution, electron contamination, penetration depth properties, neutron production, and beam *flatness*[1] for varying field size. Recent research has investigated the complete removal of the flattening filter to elevate the dose output in situations where beam flatness is not advantageous such as in intensity modulated radiation therapy (IMRT) [Vassiliev et al., 2007, 2006; Titt, Vassiliev, Pönisch, Kry and Mohan, 2006; Titt, Vassiliev, Pönisch, Dong, Liu and Mohan, 2006; Mesbahi and Nejad, 2008; Mesbahi, 2007; Mesbahi et al., 2007; Kry et al., 2008, 2007]. Sample target–primary collimator–flattening filter orientations are displayed for 6 MV and 18 MV incident electrons in Figures 1.7 and

[1]Beam flatness refers to the flatness of a lateral measured dose profile in the high dose region

1.8.

The medical linac can be made to produce a therapeutic electron beam in lieu of the photon mode described above. In electron mode the electron target is rotated out of position and the flattening filter is replaced by an electron scattering foil system. The scattering foil system is constructed of two scattering foils, the first of which is typically constructed from a thin sheet of high-Z material and is designed to spread the electron beam from the waveguide. The second foil, located downstream of the first foil, is used to flatten the electron beam and may be constructed from a thicker low-Z foil with a higher Z region fused to the foil in the region of the beam's central axis.

The beam's cylindrical symmetry, instantaneous dose rate and integral dose rate are all monitored using a gas filled transmission style ionization chamber. The chamber is divided into sectors to allow acquisition of beam balancing symmetry measurements. These measurements allow the feedback of alignment corrections to electron beam steering magnets located upstream within the bending magnet and accelerating waveguide structures.

Secondary beam collimation occurs on the flattened beam (photon and electron) using paired sets of Tungsten blocks *(JAWS)* and is intended to provide large area collimation of the beam to approximate treatment field sizes. The Clinac 21 EX contains 2 sets of parallel opposed JAWS capable of collimating the field into rectangular fields. Each jaw is limited to $\pm$ 20.0 cm of travel from the beam's central axis thereby allowing a maximum field size of 40.0×40.0 cm^2 at a distance of 100 cm from the target. The conical field produced by the primary collimator is constructed such that a 35.0×35.0 cm^2 square field is the maximum field size able to fit within the conical field at a distance of 100 cm from the target. Clipping in the corner regions of field sizes greater than 35.0×35.0 cm^2 is therefore observed (see Figure 1.9).

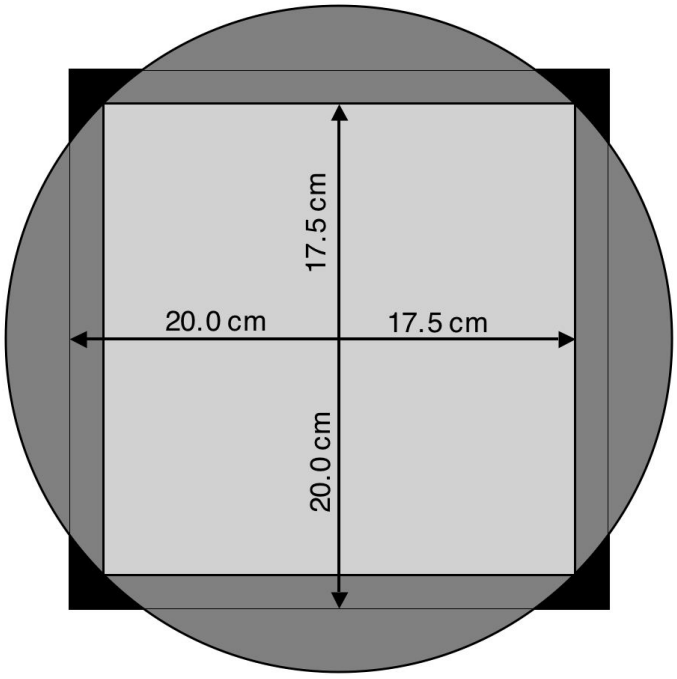

Figure 1.9: Field clipping occurring for fields greater than 35.0×35.0 cm^2 as a result of the conical bore in the primary collimator. In this figure the innermost field is 35.0×35.0 cm^2 and outermost field is 40.0×40.0 cm^2 in a plane located 100.0 cm from the target. The clipped area is displayed in black.

1.2.4 The Multi-Leaf Collimator

Finer collimation of the photon beam can be achieved using a multi-leaf collimator (MLC) device. The MLC is comprised of two sets (banks) of machined Tungsten leaves driven independently by a set of motors. The Tungsten leaves (located downstream of the secondary collimator) from the Varian Millennium MLC are shown in Figure 1.10.

Figure 1.10: A Varian Millennium multi-leaf collimator shown with arbitrary leaf arrangement. [Varian Medical Systems, Palo Alto, CA]

MLC leaf banks may also consist of wider leaves in the periphery region of the field in addition to the equal width leaves shown in Figure 1.10. Wider leaves reduce the modulation capability of the MLC but also reduce the number of seams through which radiation may "leak" (known as inter-leaf leakage).

For radiotherapy delivery of some brain cancers (astrocytomas, glioblastoma multiforme, gliomas, etc.), specialized MLC's can be used in a process known as *stereotactic radiosurgery*. Such devices consist of narrow leaf banks ($\leq$ 2.5 mm width) driven by precision motors capable of highly precise delivery of radiation.

In accelerators such as the Elekta SL20[2] the MLC is located above the secondary collimator. In its design the MLC replaces one set of the secondary collimating jaws (along the direction of leaf travel) resulting in a more compact treatment head.

1.3 KERMA and Absorbed Dose

The energy transfer from a photon field to a medium can be regarded as a two step process:

(i) Interaction of the photon field with atoms in the medium, resulting in a transfer of energy, setting one or more charged particles in motion.

(ii) Transfer of energy from the moving charged particles to the medium through excitations and secondary ionizations of atoms in the medium.

The quantity characterizing step *(i)* is *KERMA* or Kinetic energy released per unit mass,

$$K = \frac{dE_{\text{tr}}}{dm}, \tag{1.1}$$

where dE_{tr} is the energy transferred from photons to the primary electrons in elemental mass of the medium dm. The quantity characterizing the interactions of step *(ii)*, along the range of the primary electron, is the *absorbed dose*. *KERMA* along with *absorbed dose* are measured in units of J/kg or Gy (Gray) where 1 Gy=1 J/kg.

TERMA or Total energy released per unit mass, quantifies the energy of the primary photons that is both imparted to secondary charged particles and retained by the scattered photons. In other words, TERMA is the energy removed from the primary beam per unit mass of medium.

1.4 The Importance of Accuracy in Radiation Delivery

Research efforts over the past decade have focused on techniques to minimize the normal tissue exposure during an external beam radiation therapy treatment. The

[2]Elekta, Stockholm, Sweden.

importance of accuracy in radiation delivery is most apparent by observing the probability of local tumour control and normal tissue complications as a function of the absorbed radiation dose in tissue. Predictive models derived from average population radiation therapy responses are shown in Figure 1.11. From this figure, tumour control probability (TCP) is shown to sharply rise starting from a particular absorbed dose. The normal tissue complication probability (NTCP) rises sharply at a slightly higher absorbed dose. A desirable radiotherapy plan is one that maximizes TCP while minimizing NTCP. The highly sensitive nature of the TCP and NTCP dose responses combined with the potentially small differences in dose response curves demonstrate the need for accuracy in radiation delivery. Small differences in absorbed dose can be seen to have substantial effects on the treatment's TCP and NTCP outcomes. The uncomplicated tumour control probability (UTCP) is also plotted in Figure 1.11. UTCP represents the probability of achieving local tumour control while having no complications and is simply calculated as TCP×(1-NTCP).

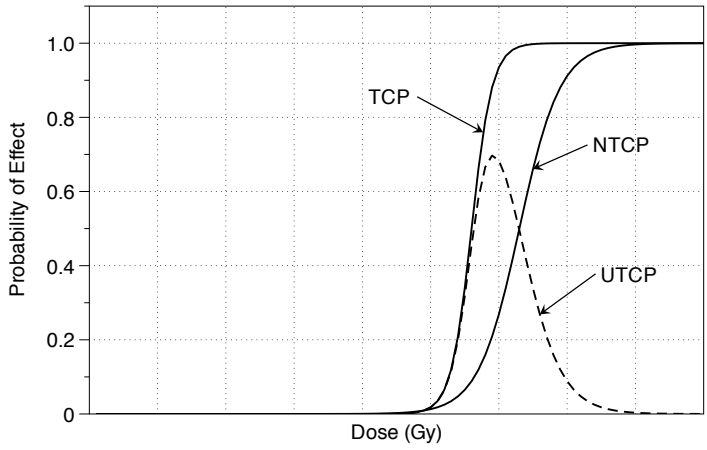

Figure 1.11: Predictive models of tumour control probability (TCP), normal tissue complication probability (NTCP), and uncomplicated tumour control probability (UTCP) with absorbed dose to tissue.

It should be noted that the standard deviations of TCP and NTCP predictive models has been estimated as high as 15-20%. In addition, the shapes and positions

of the curves may vary between patients and/or tissue type. Recent radiobiological research is aimed at improving the understanding of factors affecting the TCP and NTCP functions of various patient and tissue response classes. A better understanding of patient dose response may allow adjustments of prescribed treatment doses based on individual patient dose response evaluation.

1.5 Advanced External Beam Delivery Techniques

In the context of this thesis, traditional external beam photon radiotherapy delivery shall be defined as the application of 1 - 7 photon beams of uniform intensity across the field[3] with the optional use of a wedge (physical or dynamic) and/or field compensator[4]. A field conforming to the clinical treatment volume is achieved through the use of heavy alloy shielding placed in the beam, or more recently through the use of the MLC to create a conformal radiation field. Several advancements to traditional external beam radiotherapy have been made in the recent decades. Several of these advancements are presented in the following sections.

1.5.1 Intensity Modulated Radiation Therapy

By the mid-1990's, advances in technology and software allowing the calculation and delivery of non-uniform fluence maps on 3-D patient volumes, together with the development of the modern MLC, enabled the clinical implementation of a class of delivery techniques known as intensity modulated radiation therapy (IMRT). It has been said that IMRT represents one of the most important technical advances in RT since the advent of the medical linear accelerator [IMRT Collaborative Working Group, 2001]. In IMRT, the photon field intensity can be modulated, through movement of the MLC leaves, to deliver a highly sculpted dose of radiation. The movement can occur while the beam is on (dynamic MLC) [Boyer and Yu, 1999; Webb, 1998], or while

[3]Uniform in the sense that no modulation of the beam intensity has occurred.

[4]An attenuator used to flatten non-uniform dose contour lines resulting from patient anatomy/geometry.

the beam is off by forming a series of static apertures (segmental MLC) [de Gersem et al., 2001; Earl et al., 2003; Shepard et al., 2002; Webb, 2004; Yu, 2006].

The modulation can be determined through a process of *inverse treatment planning*. In inverse treatment planning, an objective (prescribed) dose distribution is first constructed within a patient model defining the prescribed dose to the clinical treatment volume (CTV) and surrounding organs at risk (OAR). The number of fields and gantry angles are defined and each (open field) beam is divided into a number of segments (beamlets). A search of beamlet weights is performed to determine the optimal beamlet weights (fluence map) such that the sum of weighted beamlet dose distributions is in optimal agreement with the objective dose distribution, for the given number of fields and gantry angles [Brahme, 1988; Chui and Spirou, 2001; Thieke et al., 2002]. This technique is commonly referred as *fluence based optimization*. For dynamic MLC treatments, the MLC leaf sequence must be derived from the ideal fluence map [Shepard et al., 2002]. In general, the resulting MLC leaf sequence may not be physically deliverable and may require approximation [Que, 1999]. The resulting fluence map is commonly referred to as the *deliverable fluence map* [Webb, 1991].

Conclusions formed from the National Cancer Institute's (NCI), Intensity Modulated Radiation Therapy Collaborative Working Group [IMRT Collaborative Working Group, 2001] state that, compared to conformal radiotherapy, IMRT has been found to:

(i) Reduce normal tissue radiation exposure

(ii) Decrease treatment efficiency by delivering less dose per MU

(iii) Increase the total-body dose received by the patient during delivery

(iv) Increase stress on the linac from increased heating and movement of the MLC

Recent research has also investigated the plausibility of using the MLC for modulated electron radiation therapy (MERT) [Klein et al., 2008; Jin et al., 2008; Gauer et al., 2008; Al-Yahya et al., 2007].

1.5.2 Helical Tomotherapy

Helical tomotherapy is an IMRT technique in which radiation is delivered using a narrow slit beam (approximately 2 cm $\times$ 20 cm) during a continuous helical motion about the patient [Mackie et al., 1993]. The treatment is analogous to that of helical computed tomography imaging. Nomos Corporation[5] developed the multileaf intensity-modulating collimator (MIMiC) as part of the Peacock delivery system for tomotherapy delivery. The MIMiC device consists of 2 banks of 20 binary leaves able to modulate the field by driving the leaves open or closed during the helical path of the treatment head [Khan, 2003]. A computed tomography (CT) imaging device is also mounted to the rotating ring gantry allowing acquisition of the patient's anatomical geometry while laying on the treatment couch. Today, helical tomotherapy is delivered on a dedicated tomotherapy machine using the Tomo-Therapy HI-ART II system (Tomotherapy, Madison, WI). A schematic diagram of the helical tomotherapy unit is shown in Figure 1.12.

Helical tomotherapy represents a second generation tomotherapy design following serial tomotherapy [Khan, 2003]. Using serial tomotherapy the radiation treatment arc is delivered 360^o about the patient with a fixed patient couch. The couch is then translated before subsequent arcs are delivered. In this way, serial tomotherapy is analogous to traditional CT imaging. Serial tomotherapy treatment effectiveness was found to be highly sensitive to couch position accuracy. That is, small inaccuracies in axial positioning of the patient for each delivered arc led to large dose inhomogeneities within the CTV. Incorporation of a helical treatment head path was found to reduce inhomogeneities by allowing a more continuous delivery of dose along the axis of

[5]Nomos Corporation, Sewickley, Pennsylvania

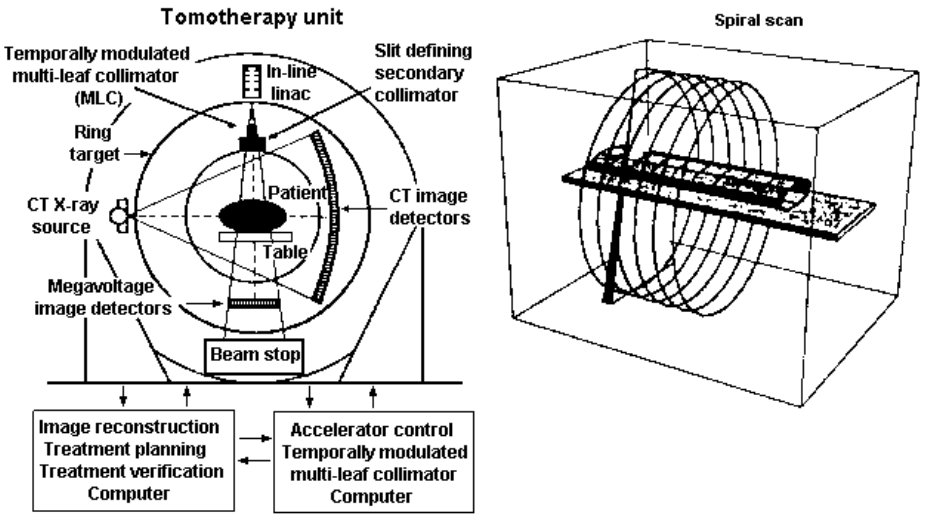

Figure 1.12: Schematic diagram of Helical Tomotherapy. [Mackie et al., 1993]

rotation, effectively *feathering* the dose delivered between arcs.

Several treatment site specific comparisons of the effectiveness of tomotherapy with (MLC-based) IMRT have been reported in the literature [Cheng et al., 2001; Lee et al., 2008; Mavroidis et al., 2007; McIntosh et al., 2008; Peñagarícano, 2006; Sheng et al., 2007; Van Vulpen et al., 2005]. A recent study by Bortfeld and Webb [Bortfeld and Webb, 2008] found tomotherapy to provide a greater flexibility over IMRT in shaping intensity maps and that tomotherapy allows the delivery of 3-D IMRT in a way that comes close to the ideal case in the transverse plane.

1.5.3 Intensity Modulated Arc Therapy™

First proposed by Yu in 1995 [Yu, 1995], intensity modulated arc therapy (IMAT) is a cone beam alternative to tomotherapy, avoiding the junction problems of serial tomotherapy and utilizing a standard IMRT capable linear accelerator [Williams, 2003]. Successful implementation of IMAT was intended to bring the benefits of rotational IMRT to a large number of radiotherapy clinics because of the wide availability of conventional linear accelerators. However, inverse treatment optimization of IMAT

was found to be difficult as the intensity solution space was found, in general, to be non-convex [Earl et al., 2003]. It has been suggested that this may be the reason why IMAT, though announced in the mid-1990's, did not gain popularity clinically for nearly a decade when planning algorithm developments improved the optimization process [Shepard et al., 2007]. IMAT is now offered as part of the Pinnacle treatment planning system (Philips Medical, Madison, WI) and can be delivered using Varian or Elekta accelerators.

During an IMAT treatment, the accelerator gantry rotates about the patient continuously while the MLC dynamically modulates the beam's intensity. Multiple arcs may be required to deliver the prescribed dose distribution. A typical treatment has been found to require 3 - 5 arcs [Yu, 1995]. A study by Cao *et al.* [Cao et al., 2007] has demonstrated that IMAT can deliver comparable plan quality to that of helical tomotherapy. However, with more complex planning criteria imposed, helical tomotherapy was able to deliver plans of slightly higher quality.

1.5.4 RapidArc™and Volumetric Modulated Arc Therapy™

Varian's RapidArc delivery system (Varian Medical Systems, Palo Alto, CA) is very similar to the IMAT delivery method described by Yu [Yu, 1995]. The major difference is that RapidArc is capable of delivering the entire treatment with only one rotation of the gantry and is therefore potentially faster. During the rotation, the orientation of the MLC leaf travel can be angled to the path of rotation. The ability to select the MLC orientation allows reduction of the artifacts in the dose distribution from inter-leaf leakage. Alternatively, by aligning the leaves with the rotation plane, the inter-leaf leakage can be incorporated in the dose delivery. The benefit of the single arc over IMRT is in reducing the required number of monitor units for a treatment and hence faster treatment times, reducing patient exposure to scattered radiation and reducing patient movement. An example illustration of a RapidArc treatment is shown in Figure 1.13 *(left)*. The ability to determine the MLC leaf sequencing for

RapidArc was made possible by the work of Otto [Otto, 2008]. Several early studies investigating the effectiveness of RapidArc and comparison with other arc treatment modalities have been published [Clivio et al., 2009; Cozzi et al., 2008; Fogliata et al., 2009, 2008; Gagne et al., 2008; Johansen et al., 2009; Kjaer-Kristoffersen et al., 2009; Korreman et al., 2009; Ling et al., 2008; Nicolini et al., 2008; Vanetti et al., 2009; Zimmerman et al., 2009].

Figure 1.13: The RapidArc ™ *(left)* and VMAT ™ *(right)* radiation delivery systems. [Varian Medical Systems, Palo Alto, CA] [Electa AB, Stockholm, Sweden]

The RapidArc delivery system is termed a volumetric modulated arc therapy (VMAT) technique. A nearly identical arc delivery system is now offered by Elekta (Elekta AB, Stockholm, Sweden) under the name VMAT. Elekta's VMAT is similarly designed to deliver the radiation in a single arc and is also capable of completing a treatment fraction in under 2 minutes. An example illustration of an Elekta VMAT treatment is shown in Figure 1.13 *(right)*.

1.6 Treatment Plan Optimization

The subject of treatment plan optimization is now briefly introduced in this section. It should be noted that it is inherently difficult to report the specific inner workings

of commercial treatment plan optimization algorithms as the material is, in general, proprietary. A basic description of a probabilistic metaheuristic type algorithm for the minimization of a cost function is now presented along with a discussion of the method of dose calculation in commercial treatment plan optimization systems.

1.6.1 Simulated Annealing

Dynamic MLC leaf sequences or static MLC apertures for delivery of an intensity modulation are commonly derived from an optimally derived radiation intensity map. The optimal radiation intensity map can be determined through a stochastic iterative optimization method such as simulated annealing. In this method, the radiation field is divided into beam elements (beamlets)[6] for which the weights of each can be optimized to minimize a cost function. Equation 1.2 serves as an example quadratic cost function quantifying difference in dose agreement between a prescribed dose distribution and a realized beamlet weighted dose distribution (based on the original radiotherapy treatment planning cost function presented by Webb [Webb, 1991])

$$C_n = \left[\left(\frac{1}{N} \right) \sum_r I_n(\overrightarrow{r}) \left(D_o(\overrightarrow{r}) - D_n(\overrightarrow{r}) \right)^2 \right]^{0.5}, \tag{1.2}$$

where C_n is the cost at the nth iteration, $D_0(\overrightarrow{r})$ is the desired dose at the point $\overrightarrow{r}$ in the patient, $D_n(\overrightarrow{r})$ is the computed dose at point $\overrightarrow{r}$ after the nth iteration and N is the number of dose points taken. $I_n(\overrightarrow{r})$ is an importance weighting factor that can be used to scale the cost function contribution from n regions/organs within the patient. In this function $D_n(\overrightarrow{r})$ is determined during each iteration by calculation of the weighted sum of beamlet dose distributions at point $\overrightarrow{r}$ by

$$D_n(\overrightarrow{r}) = \sum_m W^m D^m(\overrightarrow{r}), \tag{1.3}$$

for which W^m is the weight of beamlet m and $D^m(\overrightarrow{r})$ is the dose to point $\overrightarrow{r}$ from

[6] Beam elements can alternatively be referred to as fluence elements or fluence pixels.

beamlet m.

The search for a global minimum of C_n is often carried out through the use of a simulated annealing type regime to avoid becoming "trapped" within local minima during the search for the global minimum. A comprehensive description of conventional treatment plan optimization is provided by Webb [Webb, 1991]. In general, the cost function of Equation 1.2 is minimized by iteratively adjusting weights W_m for each n iteration, accepting those adjustments that reduce C_n, and accepting those adjustments that increase C_n with a probability function such as

$$P_{\text{accept}} = e^{-\frac{C_{i+1}-C_i}{kT}}, \tag{1.4}$$

where the temperature T is decreased according to a "cooling schedule", C_{i+1} and C_i are the calculated costs for the current and previous iterations and k is an arbitrary constant.

It should be noted that often the MLC leaves cannot be made to deliver the optimal intensity map derived by the above simulated annealing optimization algorithm due to mechanical restrictions, radiation leakage through the leaves and/or the physical leaf dimensions [LoSasso et al., 1998].

As observed by Llacer *et al.* [Llacer et al., 2003] and Jeraj *et al.* [Jeraj et al., 2003], in the presence of non-convex parameter spaces, few cases with local minima actually arise in practice. Those that were observed were found to produce dose distributions very close to the global minimum suggesting that alternatives to simulated annealing (such as stochastic gradient descent) could also be successfully used in radiotherapy optimization.

Bush [Bush and Popescu, 2006] has introduced a modification to the above cost function for use with MC dose calculation in which C_n is further weighted by $\sigma(\overrightarrow{r})^{-1}$, the simulation uncertainty at point $\overrightarrow{r}$. The cost function is then

$$C_n = \left[\left(\frac{1}{N} \right) \sum_r I(\overrightarrow{r}) \frac{\left(D_o(\overrightarrow{r}) - D_n(\overrightarrow{r})\right)^2}{\sigma(\overrightarrow{r})^2} \right]^{0.5} . \quad (1.5)$$

In this way, the cost function is isomorphic with the χ^2 statistic and the optimization becomes a χ^2 minimization.

1.6.2 Dose Calculation in Treatment Planning Optimization

The majority of implementations of treatment planning optimization algorithms for IMRT have performed calculations of the dose delivered from each beamlet or fluence element ($D_m(\overrightarrow{r})$ from the previous section) using a *pencil beam convolution/superposition* type algorithm [Boyer and Mok, 1985; Mohan et al., 1986; Mohan and Chui, 1987]. In this approach, the dose delivered is calculated at each calculation point within the patient using a convolution of the TERMA (see Section 1.3) from the finite sized beam element of radiation with a radial dose deposition kernel describing the dose component from scattered particles for a given material density, mean energy and intensity [Metcalfe et al., 2007]. Because separate kernels must be used for each material density, the convolution is technically a superposition operation, by which it is alternatively referred.

The accuracy of convolution/superposition pencil beam algorithms has been thoroughly investigated. In particular, their ability to correctly model dose in the presence of tissue inhomogeneities was examined. Ma *et al.* [Ma et al., 2000] have shown a commercial implementation to miscalculate dose by up to 20% within organs at risk where inhomogeneities exist. Significant differences with Monte Carlo dose calculation have also been reported by Wang *et al.* [Wang et al., 1998]. Cranmer-Sargison *et al.* [Cranmer-Sargison et al., 2004] have shown inaccuracies (overestimation of the dose to lung) in lateral profiles across a sharp lung-water interface by as much as 16%. Knoos and Weislander [Knoos et al., 1995; Wieslander and Knoos, 2000] have also observed differences in a mediastinum water-cork geometry by as much as 14%.

The above findings have recently prompted several improvements to commercial convolution pencil beam algorithm. For example, Varian's new anisotropic analytical algorithm (AAA) accounts for tissue heterogeneity anisotropically in the three-dimensional neighbourhood of an interaction site by using photon scatter kernels along multiple lateral directions [Ulmer et al., 2005]. Studies on the accuracy of the algorithm have found significant improvements. Confidence limits on the lung-water interface test was found to be within 4% [Gagné and Zavgorodni, 2007]. Sterpin *et al.* [Sterpin et al., 2007] has found the algorithm accurate to within 5% at interfaces and 1.7% differences in the mean planning target volume dose for a clinical case. The improvements to the algorithm come at a computational cost. The algorithm cannot be implemented in the iterative stages of the optimization at present due to the required computational time. The algorithm is used only after the optimization completes as a final dose calculation.

Modeling the photon fluence through the MLC for intensity modulation is inherently difficult with analytical methods and can contribute to the inaccuracy of commercial treatment planning systems. The accuracy of commercial MLC modeling in the Eclipse treatment planning system has been investigated by Gagne *et al.* [Gagne et al., 2008], where it was determined that modeling errors can be as high as 12% near isolated MLC leaf edges and up to 5% at the leaf end. Mihaylov and Siebers [Mihaylov and Siebers, 2008] have also observed significant dose calculation errors leading to optimization convergence errors resulting from use of a convolution/superposition algorithm in deliverable IMRT optimization for head-and-neck patients.

While improvements to convolution/superposition pencil beam algorithms have been made, further improvement can be achieved through the use of *Monte Carlo* based dose calculation techniques. A significant reduction in dose calculation errors and optimization convergence errors can also be achieved through the use of a more

accurate Monte Carlo algorithm [Mihaylov and Siebers, 2008]. The Monte Carlo approach applies a stochastic approach to modeling the individual particle interactions that occur from the passage of radiation through matter. The result is the potential for a highly accurate method of determining the dose delivered to the patient. The Monte Carlo dose calculation method will be introduced in detail in Chapter 2.

1.7 Dissertation Scope

The remarkable accuracy of Monte Carlo (MC) dose calculation algorithms has led to the widely accepted view that these methods should and will play a central role in the radiotherapy treatment planning of the future. The advantages of using MC clinically are particularly evident for radiation fields passing through inhomogeneities, such as lung and air cavities, and for small fields, including those used in intensity modulated radiation therapy (IMRT). Many research groups have reported significant differences between MC and conventional treatment planning systems in such complex situations, and have demonstrated experimentally the unmatched ability of MC to model charged particle disequilibrium [Boyer and Mok, 1985; Mackie et al., 1985; Knoos et al., 1995; Wieslander and Knoos, 2000; Cranmer-Sargison et al., 2004; Vanderstraeten et al., 2006].

Alongside the development of MC methods in radiotherapy, radiation delivery techniques have continued to evolve, with arc therapy and other advanced delivery techniques poised for widespread clinical use in the coming years. Few would argue that the combination of a fast, gold standard, MC dose calculation algorithm in the planning stages of advanced radiotherapy delivery would represent a powerful tool for radiotherapy treatment. At present no tool as such exists; there are many remaining issues impeding this goal. The scope of this dissertation is, therefore, to investigate several of these existing deficiencies in an effort to both further enable and improve the use of MC dose calculation in advanced radiotherapy. In the following paragraphs

the specific developments of four techniques are presented.

A pervasive limiting factor in the MC dose calculation process remains the ability to accurately represent the radiation field emerging from the accelerator head. This limitation is not confined to the modeling of advanced RT delivery techniques, but also appears in the modeling of more rudimentary open field techniques. The subject has been extensively researched with proposed solutions coming from a variety of modifications such as to the physical densities of components (target, flattening filter) in the accelerator head model [Hasenbalg et al., 2007; Keall et al., 2003], modifications to geometric components of the model (flattening filter, primary collimator, lead shielding, etc.) [Chibani and Ma, 2007; Keall et al., 2003], variations in incident electron beam spectrum [de Smedt et al., 2005; Faddegon and Blevis, 2000; Sheikh-Bagheri and Rogers, 2002b], modifications to the EGSnrc interaction models (pair/triplet production, radiative corrections in Compton interactions) [McEwen et al., 2008].

Fluctuations in radiation output from accelerators of the same model are very common. The manufacturer's tuning process often involves adjustment of the accelerating potential and/or insertion of attenuating shims to compensate for machining and density tolerances, waveguide resonance differences and/or other tolerances during the manufacturing of each linac. For this reason each MC accelerator unit must be commissioned to measurements.

The first component of this dissertation is to develop an efficient method for the determination of the optimal intensity distribution of the pre-target electron beam able to most accurately reproduce a set of measured photon field profiles for a given accelerator structure and incident electron beam energy. To achieve this, a novel method will be presented in which the pre-target electron beam intensity distribution can be *inferred* by employing a simulated annealing algorithm. The method allows

investigation of deviations from the pure Gaussian intensity distribution (commonly assumed) and has the potential to substantially speed up the parameter selection in the computational stages of the commissioning process.

A second component of this dissertation is to design, implement and evaluate the use of a technique for the reduction of *latent phase space variance*[7] in Monte Carlo simulation. The ability to model the accelerator head in a *two-step* approach with phase spaces offers the advantage of avoiding re-simulation of the unchanging accelerator components from patient to patient. During this process, a phase space from which the patient dependent simulation begins is often required to be reused/recycled (due to the finite number of particles it contains). The recycling of phase space particles inherently introduces an additional variance into the simulation, termed latent phase space variance [Sempau et al., 2001]. The latent phase space variance is reported by simulation codes in combination with the variance associated with the standard transport of particles. Upon inspection, the latent phase space variance component was found to be sufficiently significant to be a clearly visible feature of large field calculated dose distributions, even when using a relatively large phase space file of more than 65 million particles. By applying a random azimuthal rotation about the beam's central axis to each recycled particle, the latent variance originating from the reuse of particle positions is reduced.

As of yet there are no commercially available treatment planning systems using MC dose calculation for advanced radiotherapy deliveries, such as RapidArc or VMAT. The importance of treatment plan dose verification in arc radiotherapies has been discussed by Li *et al.* [Li et al., 2001] with respect to IMAT delivery. RapidArc and VMAT radiation fields are of increased complexity, in comparison with the character-

[7]The concept of a phase space will be discussed in Chapter 2 and 4. For the current discussion a phase space can be considered to be a set of particle records (energy, momentum, type) used to describe the radiation beam at a particular location in the accelerator treatment head.

istic IMAT dynamic gantry and MLC motions. Small field apertures are commonly found in RapidArc plans as well as a variable dose rate during delivery. In a third component of this dissertation, a novel method of modeling the dose delivered from volumetric modulated arc therapy plan using MC dose calculation will be presented. The work represents the first published method of calculating RapidArc treatment plans with MC dose calculation and provides a platform for verifying other arc therapy delivery methods such as VMAT and IMAT.

At present, the optimization of IMRT plans is carried out using dose calculations from analytical methods such the pencil beam (PB) model, collapsed cone (CC) model or analytic anisotropic algorithm (AAA). Analytic dose calculation methods are, in general, faster but less accurate than MC dose calculation methods. The optimization of VMAT and RapidArc therapy plans is performed based on dose calculations from a highly simplified pencil beam algorithm that does not take into account any inhomogeneities in the patient. This simplistic dose calculation method is implemented to minimize the computational effort during the plan optimization. A final calculation of the dose to be delivered is performed after the optimization using a more accurate calculation method. The feasibility of using MC beamlets in IMRT has been investigated by Bergman *et al.* [Bergman et al., 2006]. In a step toward introducing MC dose calculation into the planning of VMAT treatments, a technique will be presented to both generate and store a set of MC calculated beamlets and the respective dose distributions for use in treatment plan optimization. A requirement to store/buffer the large amount of dose data for a set of arc therapy beamlets is not achievable without implementing a data compression technique. A novel 3-D dyadic multi-resolution decomposition algorithm will be presented and the compressibility of the dose data using this algorithm will be investigated. The MC beamlet calculation method in conjunction with 3-D compression of the resulting data represents a viable

means to introduce MC dose calculation in the planning and optimization stages of advanced radiotherapy.

Chapter 2

Introduction to Monte Carlo Sampling Methods in Radiation Therapy

2.1 The Monte Carlo Method

The Monte Carlo (MC) method is a method of approximately solving mathematical and physical problems by the simulation of random variables [Sobol, 1974]. Given a specific probability density function (PDF), the ability to generate random numbers in proportion to the PDF provides a means to simulate physical systems. This is achieved in the MC method through the transformation of a set of uniformly distributed (pseudo) random numbers (easily generated on a modern computer) into the desired distribution of random numbers.

2.1.1 Transformation of Random Numbers by Integral Inversion

Consider the known probability density function $p(x)$, for which it is desired to generate random values X, distributed over the interval $[X_{min}, X_{max}]$ with density $p(x)$. It can be shown that the values of X are given by

$$\int_{X_{min}}^{X} p(x)dx = G, \tag{2.1}$$

where G is a set of uniformly distributed numbers, and X_{min} is the lower bound of the range of desired X values [Sobol, 1974].

The method of transforming a uniform random variable is demonstrated within the following example.

Example: Integral Inversion Sampling of Interaction Probability

Consider the exponentially distributed PDF for determining the probability of interaction for a photon penetrating an infinitely thick slab of material:

$$p(x) = \mu e^{-\mu x} \quad \text{for} \quad 0 \leq x \leq \infty, \tag{2.2}$$

where μ is the sum of *linear attenuation coefficients* (in cm^{-1}) for all photon interaction types (*e.g.* pair production, Compton scattering, photoelectric effect, coherent

scattering) for a given energy and material type. Using Equation 2.1, the uniform set of random numbers G is transformed into the set of numbers X distributed as $p(x)$ in the following way:

$$G = \int_0^X \mu e^{-\mu x} dx \tag{2.3}$$

$$G = 1 - e^{-\mu X}$$

$$X = -\frac{1}{\mu} \ln(1 - G) \quad \text{for} \quad 0 \leq G < 1.$$

By binning X for a set of random numbers G, the resulting histogram is isomorphic to the shape of $p(x)$.

It is often the case, however, that $p(x)$ is of a form that Equation 2.1 cannot be inverted to solve for X. An alternative to the *integral inversion* method described above is found in the following *acceptance-rejection* MC method.

2.1.2 Transformation of Random Numbers by Acceptance-Rejection

In the event that the inverse of $p(x)$ cannot be obtained the MC method can still be applied through use of the acceptance-rejection method. This method was first used by French scientist Georges-Louis Leclerc, Comte de Buffon as early as the 18th century in a technique known as Buffon's needle. The acceptance-rejection technique was later formalized by John von Neumann.

Given the PDF, $p(x)$, a rectangular *sampling envelope* is constructed which completely encloses the area under $p(x)$. Suppose N random points uniformly distributed over the sampling envelope are chosen by generating a pair of uniform random numbers G_1 and G_2 such that

$$x_{min} \leq G_1 \leq x_{max} \quad \text{and}$$

$$p_{min}(x) \leq G_2 \leq p_{max}(x)$$

form the coordinates of the point (G_1,G_2). For each $x = G_1$ generated, $p(G_1)$ is evaluated and compared to G_2. In the event that

$$G_2 \leq p(G_1), \tag{2.4}$$

the random value G_1 is accepted, otherwise it is rejected and another set of G_1 and G_2 are generated. In this way a random set of values G_1 distributed as p(x) can be generated from two uniform distributions of random numbers. The obvious disadvantage of this method is that a portion of the random numbers generated are wasted and each accepted value requires two random numbers be generated.

Example: Acceptance-Rejection Sampling of the Klein-Nishina Cross-Section

The sampling of Compton photon scattering angles θ is now presented as an example of the acceptance-rejection method. The PDF of photon scattering angles for free electrons is described by the Klein-Nishina cross-section

$$\sigma(\theta) = \frac{1}{\sigma_c} \frac{\pi \sin(\theta) r^2 \left(1 + \cos^2(\theta) + \alpha^2 \frac{(1-\cos(\theta))^2}{1+\alpha(1-\cos(\theta))}\right)}{(1+\alpha(1-\cos(\theta)))^2}, \tag{2.5}$$

where σ_c is the total cross-section, r is the classical electron radius, θ is the photon scattering angle, and α is the ratio of incident photon energy to electron rest mass. In this example the azimuthal dependence of the cross-section has been removed through integration.

In Figure 2.1 *(top)*, the Klein-Nishina cross-section is plotted for an incident photon energy of 6.0 MeV, 0.511 MeV and 0.0511 MeV. Considering the example of a photon with incident energy of 0.511 MeV (see Figure 2.1 *bottom*), random variables G_1 and G_2 are generated from a uniform distribution (easily done with a computer) such that

$$0 \leq G_1 \leq \pi \quad \text{and}$$

$$0 \leq G_2 \leq \sigma_{max}(\theta).$$

Evaluating $\sigma(\theta)$ for all $\theta = G_1$ it is determined if the acceptance criterion of Equation 2.4 is met. The accepted values of G_1 are thereby distributed as $\sigma(\theta)$.

It should be noted that the above example is simplified for clarity. The MC sampling of a Compton scattering event employed within the MC codes used in this research employs a more complex, but faster approach. Although based on the Klein-Nishina cross-section, binding effects and Doppler broadening are included and the sampling is done using the approach of Kahn [Kahn, 1954].

Efficiency Improvements and Variance Reduction Techniques in Monte Carlo Sampling

The *unconditional acceptance probability* is calculated to be the ratio of particles accepted to those generated. Sampling is therefore more efficient when the unconditional acceptance probability is high. In the case of integral inversion sampling, the unconditional acceptance probability equal to 1. Efficiency of acceptance-rejection sampling can be increased through careful selection of the sampling envelope. In some cases the sampling efficiency can be improved by constructing a complex non-rectangular envelope.

Other techniques have been developed in an effort to increase sampling efficiency such as the Ziggurat algorithm [Marsaglia and Tsang, 2000] and the Box-Muller transform [Box and Muller, 1958]. In these cases although the unconditional acceptance probability is less than 1, computational tricks have been implemented to reduce their computation times to below that of the integral inversion method.

The variance in estimating the properties of a particular random distribution may be reduced, in some cases, through the use of an *importance sampling* technique

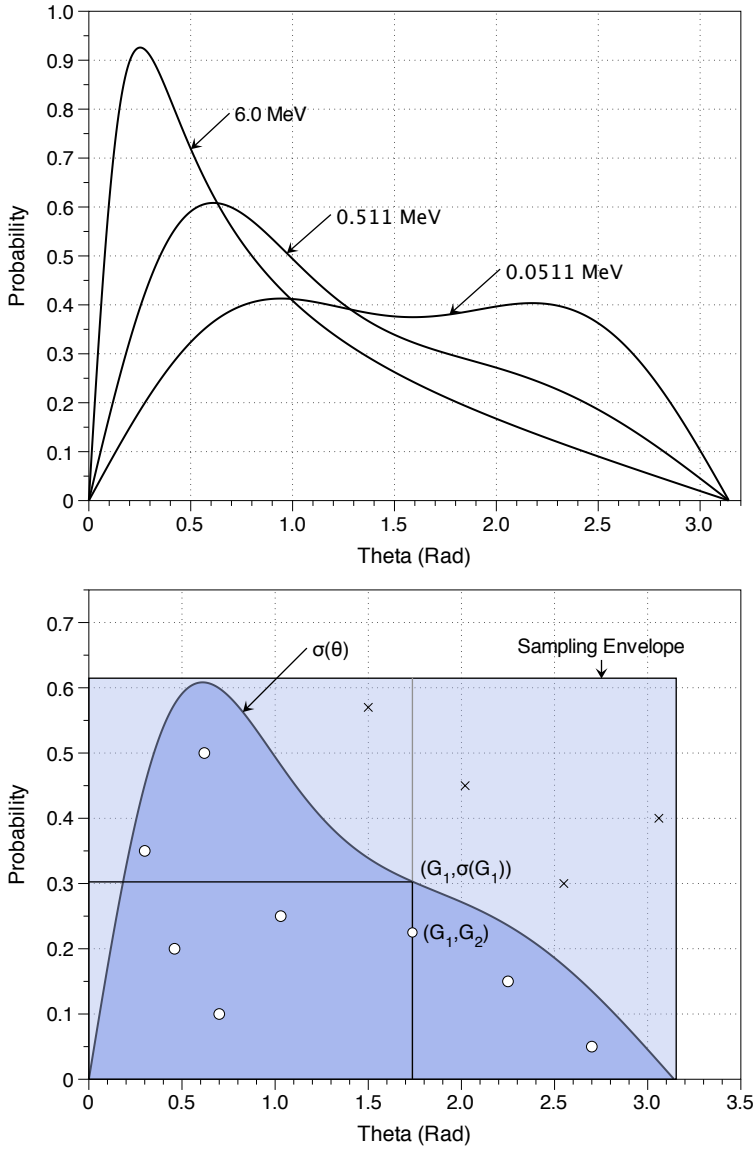

Figure 2.1: The acceptance-rejection method of transforming random variables. In this example a Compton scattering event is modeled by generating two random numbers G_1 and G_2 from a uniform distribution with a range corresponding to the sampling envelope. Accepted values of G_1 are indicated by circles while those rejected are indicated with $\times$'s.

[Robert and Casella, 2005] [Denny, 2001]. In this technique one samples from a distribution other than the uniform G of above. In importance sampling one attempts to avoid taking samples in regions where the PDF is less important to the problem at hand, and to concentrate on those regions contributing more to the problem at hand. To account for this bias the samples are weighted appropriately by the inverse of the applied importance function [Borcherds, 2000]. A careful choice of the biased distribution to encourage the important regions of the input variables is imperative as the reward can be significant run-time savings. Poor choice of distribution can result in longer run times than sampling without importance sampling [Robert and Casella, 2005].

It is somewhat natural to think of MC methods used in the above examples in simulating random, or stochastic, processes described by a PDF. It should be realized that this general description of MC methods may not seem relevant to some applications with which MC is used. For example, in the case of definite integration, random sampling would seem to have no apparent stochastic content. In such cases, shedding one's intuition and posing the solution in terms a PDF can allow the problem to be thought of as a stochastic process, and hence justify the use of the MC method to "simulate" the system.

2.2 Simulating Radiation Transport with EGSnrc

The MC methods briefly described in the previous section have been applied to many of the known interactions a particle may undergo with matter. Using these methods the ability to transform distributions of random numbers to model individual particle interactions is realized. However, in order to model the passage of a particle through, for example, a slab of lead, a particle detector, or even the human body, the ability to link the outcomes of successive interactions and particle trajectories forming the *particle shower* is required. The EGS (Electron-Gamma-Shower) code

[Nelson et al., 1985], developed at the Stanford Linear Accelerator Center, represents an amalgamation of particle interactions for the coupled simulation of electrons and photons in an arbitrary material geometry from a few keV up to several hundred GeV. Using EGS, quantities of interest can be calculated by averaging over a given set of MC particle cases or *histories*.

A detailed account of the MC modeling of particle interactions within EGS(4) is presented in the classic SLAC 265 report [Nelson et al., 1985]. Further refinements of the physics within EGS to improve its use in the modeling of radiotherapy were instituted by the Omega group in the mid 1990's within the National Research Council of Canada (NRC). The aptly named EGSnrc contained enhancements specifically to the electron transport algorithm, variance reduction techniques (bremsstrahlung splitting, Russian roulette, range rejection) and several of the physics models (bremsstrahlung angular sampling, photo-electric/Compton electron relaxations). A detailed account of the physics instituted in EGSnrc can be found in NRC Technical Report PIRS-701 [Kawrakow and Rogers, 2000].

2.2.1 Photon Interactions Modeled within EGSnrc

The interaction of photons with matter occurs via four basic processes [Kawrakow and Rogers, 2000]:

(i) Coherent (Rayleigh) scattering with atoms or molecules in the medium

(ii) Photo-electric absorption

(iii) Incoherent (Compton) scattering with atomic electrons

(iv) Materialization into an electron/positron pair in the presence of the electromagnetic field of an atomic nuclei and surrounding electrons (pair production)

With the exception of coherent scattering, each process transfers energy from the photon field to electrons within the medium. The interaction probabilities in water

below 100 MeV for the above processes are shown in Figure 2.2. From this figure it is evident that the pair production process dominates at higher energies, Compton scattering dominates at intermediate energies, and at lower energies photo-electric absorption dominates. The interaction probabilities are dependent on the medium in which the processes occur.

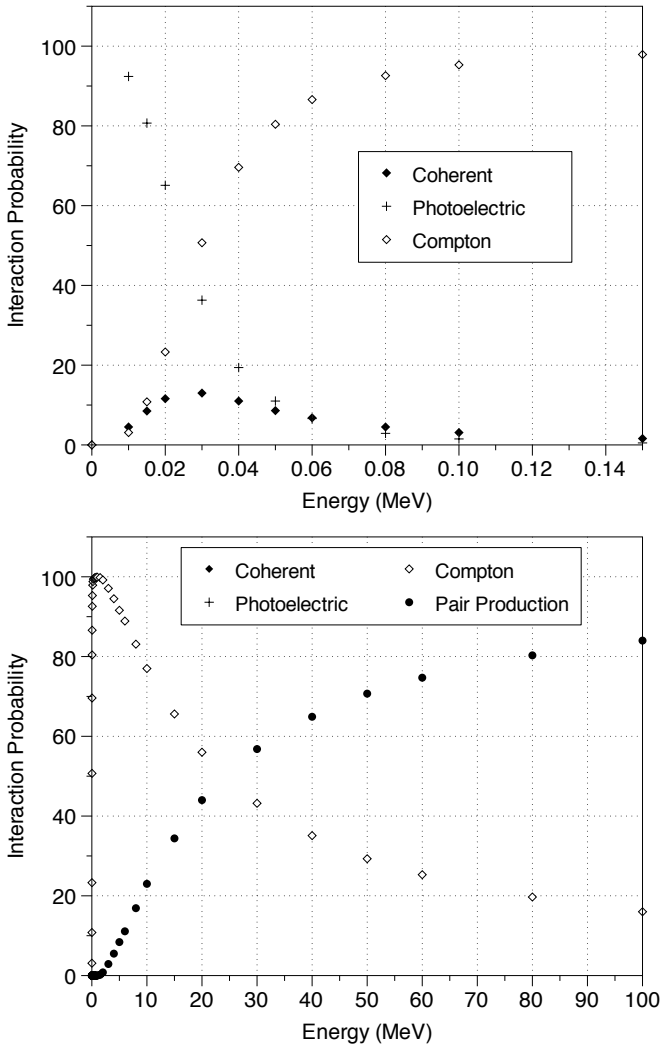

Figure 2.2: Photon interaction probabilities in water below 150 keV (top) and up to 100 MeV (bottom) of coherent scattering, photoelectric effect, Compton scattering, and pair production interactions (Data from Johns and Cunningham [Johns and Cunningham, 1983]).

Table 2.1: Summary of interaction cross-sections implemented in EGSnrc.

Interaction	Cross-Section
Coherent	Storm and Israel [Storm and Israel, 1970] ($\overline{\text{w}}$ atomic form factors [Hubbell and Øverbø, 1979]) or XCOM [Berger and Hubbell, 1987]
Photo-electric	Storm and Israel [Storm and Israel, 1970] ($\overline{\text{w}}$ Sauter distribution for photo-electron direction [Sauter, 1931]) or XCOM [Berger and Hubbell, 1987]
Incoherent	Klein-Nishina ($\overline{\text{w}}$ binding effects and Doppler broadening [Ribberfors, 1975])
Pair/Triplet	Relativistic first Born approximation [Motz et al., 1969] (Coulomb corrected > 50 MeV)

A thorough description of the cross-sections adopted within EGSnrc is available in NRC Technical Report PIRS-701 [Kawrakow and Rogers, 2000]. A summary is compiled in Table 2.1.

2.2.2 Electron Interactions Modeled within EGSnrc

An electron traveling through matter loses energy in two ways [Kawrakow and Rogers, 2000]:

(i) Inelastic collisions with atomic electrons

(ii) Radiative energy loss

Radiative energy losses occur in the form of bremsstrahlung and annihilation events with positrons. Inelastic collisions dominate at lower energies. Bremsstrahlung production dominates at high energies. In addition, electrons undergo a large number of elastic collisions with atomic nuclei leading to frequent changes in direction.

Electron Transport: PRESTA II

The modeling of charged particle transport is inherently difficult. Cross-sections for electron interaction become infinite as the kinetic energy approaches zero. The cross-sections are, in fact, finite but the exact values are not well known [Nelson et al., 1985]. However, low momentum transfer events do not significantly affect the shower results and so multiple steps can be lumped together in some cases without significant loss of simulation accuracy and approximated using a continuous slowing-down type approximation (CSDA). Lumping electron scattering events is known as a condensed history (CH) technique. A major difficulty with this technique arises in the region of material boundaries where the approach breaks down because one cannot account for the ensemble of paths occurring in the adjacent medium. Solving this problem required the development of new multiple scattering theories and more complex algorithms for transporting electrons, including reverting to modelling single scattering events near material boundaries (PRESTA II) [Rogers, 2002; Kawrakow and Bielajew, 1998].

2.3 Simulating Radiation Transport within the Accelerator Head: BEAMnrc

As described in the previous sections, EGSnrc provides a tool to accurately model a particle shower using MC methods within a defined geometry. The software package BEAMnrc [Rogers et al., 1995], represents a specialized user code of EGSnrc for the simulation of radiation beams from radiotherapy units including high-energy electron and photon beams, Cobalt-60 (Co^{60}) beams and orthovoltage machines. Geometries of the accelerator's components are defined through the use of component modules. In Figure 2.3, the component modules used in the modeling of the Clinac 21EX are displayed. From this figure, simulation A *(left)* is shown to model all of the patient independent component modules of the accelerator head: target, primary collimator, flattening filter, monitor chamber and mirror. The resulting phase space (PS_A) is then used as a source for simulation B *(right)*. During simulation B the chamber and mirror remain in place to score the backscattered dose to the chamber from the secondary collimator, a requirement for converting the resulting dose distributions to absolute dose using the method of Popescu *et al.* [Popescu et al., 2005]. By avoiding re-simulation of the unchanging components using a two-step approach, simulation times are reduced.

In Figure 2.4, the defined geometries for the Varian Clinac 21EX are displayed for energy configurations of 6 MeV *(left)* and 18 MeV *(right)*.

The ability to score particle characteristics in a phase space file (PSF) is an integral part of the BEAMnrc code, allowing the stopping/restarting of simulations, analysis of particle characteristics, modification of particle characteristics, etc. The characteristics recorded in the PSF include each particle's energy, position, direction cosines, weight, LATCH history, and optionally, the Z coordinate of the last interaction.

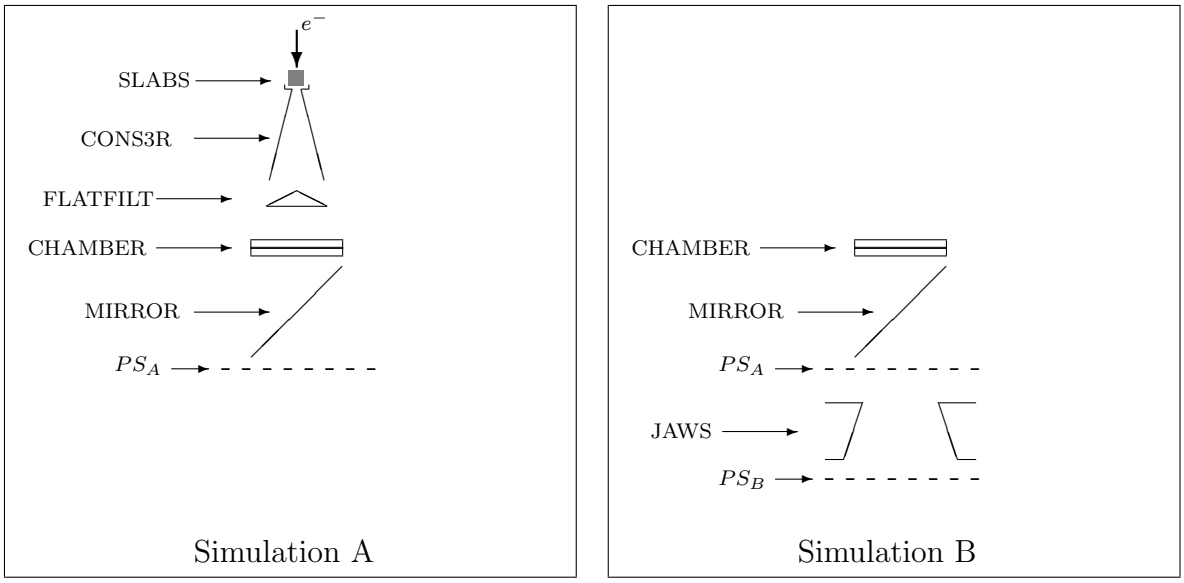

Figure 2.3: Schematics of the two-step simulation of the Varian 21EX. Simulation A *(left)* models all of the patient independent components. Simulation B *(right)* models the remaining patient dependent components. (with permission from Popescu *et al.* [Popescu et al., 2005])

2.4 Variance Reduction Techniques and Efficiency Improvements

BEAMnrc has introduced several techniques to allow variance reduction and improve simulation efficiency. An overview of the most common techniques will now be presented.

Range Rejection

Most of the computation time in MC simulation is devoted to tracking electrons. Range rejection can allow significant time savings during computations of electron transport. In this technique the residual range of each charged particle is calculated and the history is terminated if it cannot escape from its current region. The threshold for cutoff is defined using ECUT (defined in MeV, including rest mass) which can be set independently in each region of the accelerator model.

Because any potential photons (produced via bremsstrahlung) are assumed to

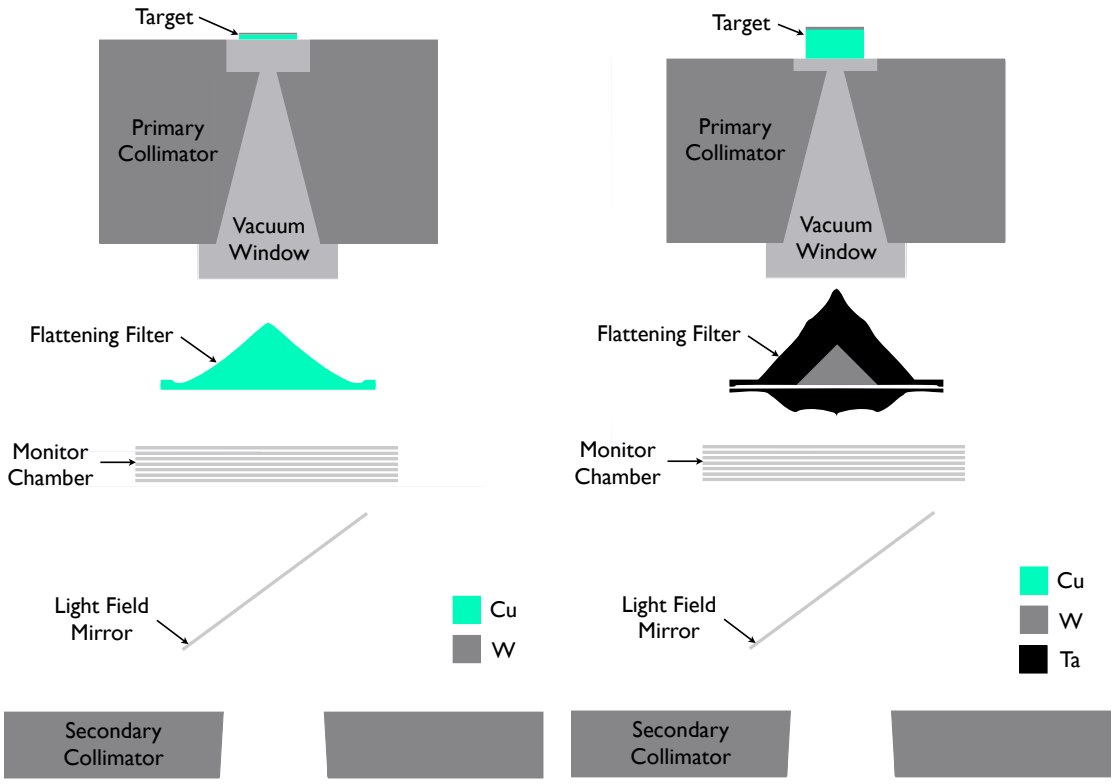

Figure 2.4: The 6 MV and 18 MV geometric accelerator models showing explicit differences in flattening filter design and target thickness for the Varian Clinac 21EX.

deposit their energy within the current region, range rejection introduces an approximation into the simulation. Care must therefore be taken to select an appropriate value for ECUT [Rogers et al., 1995]. As a general rule, ECUT is set such that an electron of energy ECUT has a range of less than $\sim 1/3$ of the smallest dimension of the geometric dose scoring region of interest.[1]

Bremsstrahlung Splitting and Russian Roulette

Photons are produced in a medical linac via bremsstrahlung within the electron target. A significant portion of the computations in a photon beam accelerator simulation involve tracking electrons within the target. The statistical uncertainty in the photon fluence, for a given number of incident electrons, can be significantly reduced by sampling multiple bremsstrahlung photons at each bremsstrahlung interaction site [Rogers et al., 1995]. To statistically account for the split, each photon is weighted by the inverse of the number of photons split into (splitting factor).

In conjunction with bremsstrahlung splitting, Russian Roulette can be used to restrict the number of electrons produced by the split photons. Since, in general, these electrons contribute little to the dose in the patient, it is not practical to simulate the many interactions required for each electron. Using Russian Roulette, the number of electrons can be reduced back down to that without splitting. This is carried out through comparison of a uniform random number, generated for each particle, to a survival threshold and terminating each particle above this threshold. To statistically account for the termination, each surviving electron is weighted by the applied splitting factor.

Further improvement to the bremsstrahlung splitting technique was achieved using a technique known as directional bremsstrahlung splitting (DBS) [Kawrakow et al., 2004]. Using DBS, multiple bremsstrahlung photons are sampled at each bremsstrahlung interaction site as before. Resulting photons that are aimed into the

[1] An ECUT of 0.700 MeV is, in general, considered conservative for most detailed simulations.

field of interest (defined by the user) are kept. All photons aimed outside of the field undergo Russian Roulette. To reduce the number of charged particles in the defined field, all photons about to undergo pair production, incoherent, or photo-electric events are forced to take part in Russian Roulette. DBS was found to increase efficiency by approximately 20 times over uniform bremsstrahlung splitting. However, DBS must be used appropriately as it will result in only a few charged particles exiting the accelerator model outside of the defined field.

Photon Forcing

Photon forcing is the process by which photons are forced to interact in specific regions of the accelerator model where relatively few interactions occur statistically. A copy of the photon is created and is forced to undergo an interaction. The weight of the scattered photon is scaled by the interaction cross section. The original photon continues on its path "unscattered" but scaled by a weight of 1 minus the interaction cross section. Photon forcing is commonly used to determine the electron contamination from particular regions of the accelerator model (such as in the air within the accelerator). Using this technique the variance of a simulation investigating particle scatter can be reduced when photon interactions are sparse.

2.5 Modeling the Multi-Leaf Collimator

For a given treatment, the MLC may be static, such as in conformal radiotherapies and aperture based IMRT, or dynamic, such as in dynamic IMRT and volumetric modulated arc therapies.

Transport through the MLC has been documented in the following ways [Chetty et al., 2007]:

(i) Explicit transport of each history through a detailed model of the MLC [Rogers et al., 2006; Heath and Seuntjens, 2003; de Walle et al., 2003]

(ii) Explicit-approximate transport in which the MLC is explicitly modeled but approximations are employed in the Monte Carlo photon/electron tracking scheme to improve simulation efficiency [Liu et al., 2001; Siebers et al., 2002; Tyagi et al., 2007]

(iii) Pseudo-explicit transport where an MLC characterization model or "toy-model" is used to describe the modulation effects [Chetty et al., 2000]

Examples of explicit transport (*i*) include the BEAMnrc component modules MLC, MLCQ, VARMLC [Rogers et al., 2006] and DYNVMLC [Heath and Seuntjens, 2003] for the Varian Millenium MLC, and MLCE [de Walle et al., 2003] for the Elekta MLC. Explicit transport is inherently the most accurate method of modeling the MLC since a particle shower is transported through a detailed MLC geometry. However, it is also the most computationally demanding. In the case of modeling a dynamic MLC, where only a small area of the field may be exposed throughout the leaf motion, the explicit transport method can result in a large number of particles terminating within the MLC [Siebers et al., 2002].

Examples of explicit-approximate transport (*ii*) methods include the work of Liu *et al.* [Liu et al., 2001], Siebers *et al.* [Siebers et al., 2002] and Tyagi *et al.* [Tyagi et al., 2007]. The approximations introduced include simplifications to the MLC geometry [Liu et al., 2001], modeling only a single Compton scattering event for each photon passing through the MLC [Siebers et al., 2002] or modeling only primary electrons created within the MLC [Tyagi et al., 2007].

An example of pseudo-explicit transport is presented by Chetty *et al.* [Chetty et al., 2000] in which a virtual source model is developed for simulating arbitrary, external beam, intensity distributions. The pseudo-explicit transport method is expected to be the least computer intensive method of modeling the MLC.

For the body of research presented in this dissertation, the explicit-approximate

method of Siebers *et al.* [Siebers et al., 2002] was chosen for modeling of the MLC. This method was selected to optimize the balance of accuracy and simulation efficiency.

2.6 Simulating Radiation Transport into the Patient

2.6.1 CTCreate

A *phantom* is constructed using a 3-D matrix of voxels (volume elements) for which each voxel contains a physical density and material assignment. There are two ways by which this matrix is most commonly created. The first way is by simply defining a set of x, y, and z boundaries and assigning densities and material types to these voxels using an (.egsinp) input file. The second way, used commonly for simulations on patient geometries, is to create the phantom from a set of CT images taken of the patient. From this set of images, the CT densities in Hounsfield units[2] (HU) are interpolated onto a 3-D matrix of voxels and converted into equivalent physical densities.

The conversion from CT densities to physical densities is achieved through interpolation of optical-to-physical density relations forming a CT ramp (see Figure 2.5). The matrix of physical densities is then written to a file (.egsphant). Also included in this file is a list of media present in the patient model, as well as a map of individual voxels to material type. It should be noted that, in general, not every material type is defined in this file. Instead, only the most common material types may be included. The assignment of material types is also achieved using the CT ramp (see Figure 2.5). The assignment of material type is based only on each voxel's average physical density. At the time of simulation the atomic properties (*eg.* electron densities) of each voxel are buffered into memory and pre-calculations of cross-section data are performed. The BEAMnrc software package includes CTCreate, a tool for creating

[2] $HU = \frac{\mu - \mu_w}{\mu_w} \times 1000.$

phantom models, as part of the distribution.

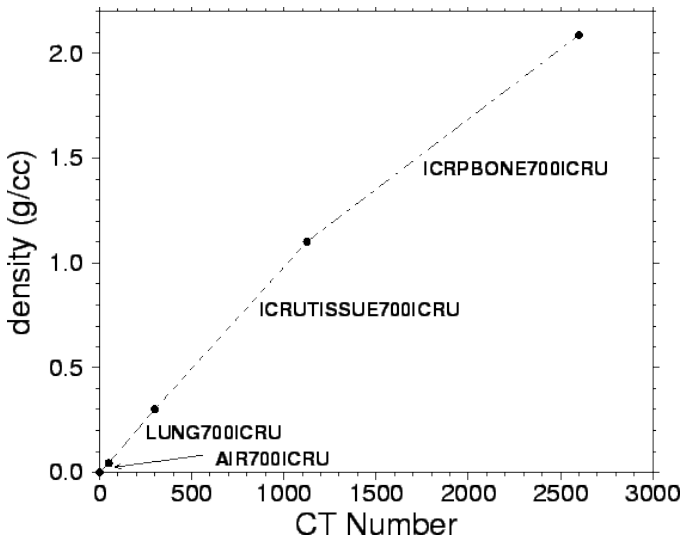

Figure 2.5: A sample CT ramp for conversion of CT values to material type and densities in CTCreate [Rogers et al., 2006]. (With permission from the National Research Council of Canada)

The DICOM (Digital Image and Communications in Medicine) image format provides a standard format by which the CT scanner data can be exported. The image resolution is not fixed, although 512 × 512 pixels is commonly used. The spacing of the pixels is determined by the size of the area that was imaged and is uniform along each axis. The number of CT images or *slices* is generally determined by the volume of the prescribed region to be imaged and the slice spacing specified by the oncologist.

Often, raw CT images contain structures (other than the patient) that, if left in the CT image, can lead to incorrect modeling of the phantom. Common sources of these structures include the CT couch, which is not made of the same material as the treatment couch (the treatment couch is carbon fiber whereas the CT couch is plastic) and CT head support. To eliminate such structures from the CT images, a program was written [Zavgorodni et al., 2007] to assign all pixels outside of a defined contour to a defined Hounsfield value (usually air or vacuum). A phantom can then

be created with the corrected CT images (see Figure 2.6).

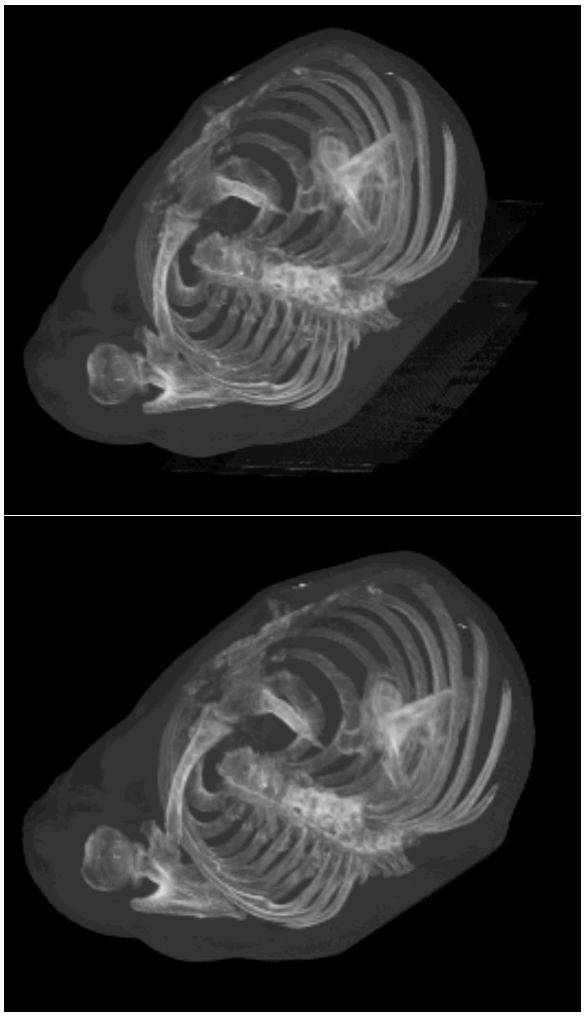

Figure 2.6: 3D reconstruction images of a DICOM CT data set before *(top)* and after *(bottom)* removal of the CT couch. Prior to removal the couch can be seen faintly in the lower right corner of the upper figure.

2.6.2 DOSXYZnrc

Once particle transport through the accelerator head has been simulated with BEAMnrc, the output can be transported into the constructed patient phantom using the DOSXYZnrc user code (included in the BEAMnrc distribution). There are several ways in which the particles emerging from the accelerator head may be passed on to DOSXYZnrc. First, through the use of a phase space file generated in BEAMnrc (and

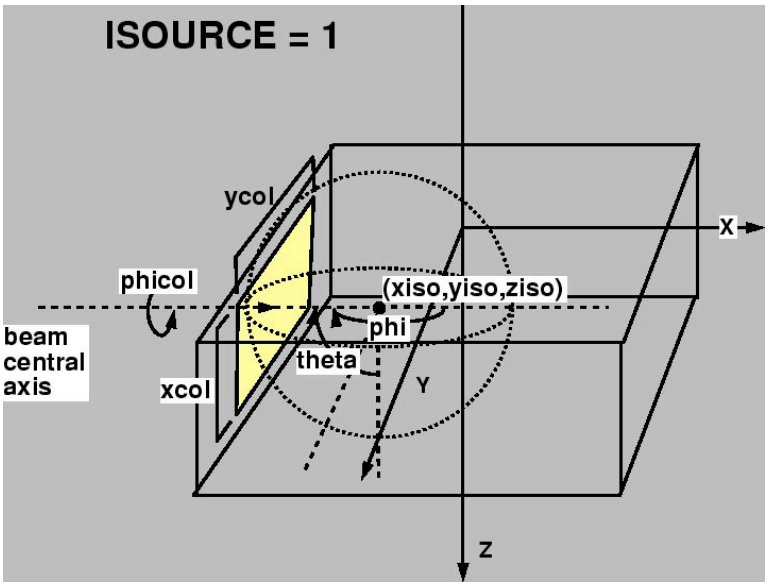

Figure 2.7: Orientation of the BEAMnrc phase space with respect to DOSXYZnrc. The isocenter, (xiso,yiso,ziso) defines the origin of the coordinate system. The phase space position is then defined using the angles, theta and phi. In this figure, with the beam incident on the centre of the negative Y face of the phantom, theta is set to 90^o and phi is set to 180^o. In this figure, xcol and ycol define the x and y dimensions of the secondary collimator (the jaws). Phicol defines the rotation of this collimator [Rogers et al., 2006]. (With permission from the National Research Council of Canada)

.

optionally modulated by a code such as vcuDMLC). Second, by characterizing the particles from BEAMnrc into a series of histograms and sampling from the derived *particle source model*. Lastly, by incorporating the BEAMnrc simulation as a shared library in DOSXYZ such that each particle requested by DOSXYZnrc is transported through the BEAMnrc simulation *on-the-fly*. DOSXYZnrc is specifically written for obtaining the dose (and accompanying uncertainty) in a Cartesian geometry.

In DOSXYZnrc, a spherical coordinate system is defined to describe the beam incidence on the phantom with an origin set to the isocenter, as defined by (xiso,yiso,ziso) the x, y, and z distances from the defined (0, 0, 0) origin of the phantom. The incident beam angle is specified by θ, ϕ, and ϕ_{col} (see Figure 2.7). In practical use of the accelerator, the incident beam angle is more commonly defined by specifying a gantry angle, couch rotation angle, and collimator rotation. A coordinate transforma-

tion is therefore required. Transformation between a right-handed Eclipse coordinate system and DOSXYZnrc coordinate systems is given by [Thebaut and Zavgorodni, 2006]

$$\theta = \cos^{-1}(\sin(\gamma)\sin(\rho)),$$

$$\phi = \tan^{-1}\left(\frac{-\cos(\gamma)}{\sin(\gamma)\cos(\rho)}\right), \quad \text{and}$$

$$\phi_{col} = \pm\cos^{-1}\left[\cos(\omega)\cos(\gamma)\cos(\rho)\sin(\phi) - \sin(\omega)\sin(\rho)\sin(\theta) - \cos(\omega)\sin(\gamma)\cos(\phi)\right],$$

where γ is the gantry angle, ρ is the couch rotation, and ω is the collimator rotation in Varian Eclipse coordinates. The sign of ϕ_{col} is determined by taking the sign of

$$\cos(\omega)\sin(\rho)\sin(\phi) + \sin(\omega)\left[\cos(\gamma)\cos(\rho)\sin(\phi) - \sin(\gamma)\cos(\phi)\right].$$

The absorbed dose is recorded or *scored* in a 3-D array of voxels with boundaries as defined in the CT phantom. The user can choose to omit specific voxels from the scoring array. By default, the dose, uncertainties, and voxel boundaries are all written in American Standard Code for Information Interchange (ASCII) format to a (.3ddose) file.

2.6.3 VMC++

A group of Voxel Monte Carlo (VMC) codes have been developed with the aim of improving the efficiency of MC particle transport with regards to radiotherapy treatment planning [Kawrakow et al., 1996; Fippel, 1999; Kawrakow and Fippel, 2000a,b]. For the purpose of this dissertation, a focus will be placed on the VMC++ code [Kawrakow and Fippel, 2000b]. A comprehensive overview of VMC codes can be found in AAPM Task Group Report 105 [Chetty et al., 2007].

VMC codes specialize in particle transport within a voxelized structure for radiotherapy use (*i.e.*, low-Z materials with densities in the $< 3\text{g/cm}^3$ and energies below 30 MeV). The increase in simulation efficiency over DOSXYZnrc is achieved in VMC++ from the use of additional variance reduction techniques and the use of a faster electron transport algorithm [Kawrakow and Fippel, 2000a].

Perhaps the most significant variance reduction technique introduced is the simultaneous transport of particle sets (STOPS) in which the set of electron tracks set in motion from a particular interaction type (pair production, Compton, photo-electric) are saved and reused at other points in the patient. Another feature of VMC++ is that an electron step can traverse several voxels, which results in significantly fewer electron steps over DOSXYZnrc [Gardner et al., 2007]. In addition, electrons can be transported down to zero energy avoiding the deposition of all electron energy below a cutoff (ECUT) in the current voxel.

A validation of VMC++ dose calculation for photon beams is presented by Gardner *et al.* [Gardner et al., 2007]. The study concluded that, for the observed patient plans, the most severe systematic difference introduced by VMC++ was 0.98% of the maximum dose for 2% of the voxels containing significant dose. The efficiency gain was found to be at least 10 times over DOSXYZnrc.

The use of VMC++ to model clinical treatment plans requires transformation of the gantry, couch and collimator angles (International Electrotechnical Commision or IEC coordinates) into the VMC++ coordinate system. A transformation was derived by the author from IEC coordinates into VMC++ coordinates (see Section 5.2.1), which utilize the Euler angles to specify the incident beam (*i.e.*, phase space) orientation.

2.7 Commercial Radiotherapy Systems Utilizing Monte Carlo Dose Calculation

Several challenges have historically impeded the clinical implementation of a MC dose calculation algorithm, most significantly, insufficient computation available for dose calculations to be performed within a reasonable time frame.[3] Along with consistent advancements in computer hardware, many variance reduction techniques have been implemented in today's MC simulation codes in an effort to improve efficiency [Kawrakow et al., 1996; Fippel et al., 1997; Kawrakow and Fippel, 2000a; Siantar et al., 2001; Fix et al., 2004; Rogers et al., 2006; Walters et al., 2005; Tyagi et al., 2006]. Although still requiring significantly more computation than conventional dose calculation techniques, MC dose calculation times can be reduced to the point of clinical acceptability. Peregrine (North American Scientic: Nomos Division) recently became the first FDA approved planning system with MC dose calculation for external beam radiotherapy. Peregrine, developed at the Lawrence Livermore National Laboratory, implements a modified version of the EGS4 library with a new condensed history electron transport algorithm. VMC codes are also making their way into many of the latest commercial treatment planning systems (CMS Monaco, Elekta PrecisePlan, Brainlab iPlan, Nucletron MasterPlan and Varian Eclipse). Initial implementations were focused on MC dose calculations for electron beam therapy planning as the performance of analytical electron beam dose deposition calculations have shown significant inaccuracies (as much as 5-10%) [Ma et al., 1999; Heath et al., 2004; Cygler et al., 2005; Pemler et al., 2006] and the modeling of a clinical electron beam can be inherently faster than a photon beam.

At present date, the clinical implementation of MC dose calculation for both electron beams and IMRT is still very much in the evaluation stages and is likely several

[3]It is understood that the term *reasonable* is perhaps different to many RT workers. It may be suggested here that reasonable be on the order of 20 - 30 minutes rather than hours.

years away from widespread clinical use. Although desirable, there are currently no commercial MC based treatment planning implementations for advanced radiotherapy techniques such as RapidArc, Volumetric Modulated Radiation Therapy, Helical Tomotherapy, or Intensity Modulated Arc Therapy.

It is important to add that in the development of a product, the commercial vendor is subject to the pressures of the competition and the demands of the consumer. Recently, the term *MC dose calculation* has become a highly desirable marketing platform for new commercial RT products. As a result of market pressure, the implementation of MC dose calculation may be forced to contain practical approximations into the MC method to speed calculations (e.g. simplifying the electron transport algorithm) or improve the agreement with measurement (e.g. unjustified energy/particle fluence correction functions), and may not necessarily reflect many of the research methods as used in the published literature. One must therefore exercise caution to determine exactly what is implied by the use of the term "Monte Carlo dose calculation" in a commercial product and perform a thorough benchmark of such products against heavily tested codes such as EGSnrc (see for example a comparison of Peregrine against EGSnrc [Heath et al., 2004]).

The following chapters address a series of challenges that exist in Monte Carlo dose calculation. The proposed solutions are presented in an aim to help lay the groundwork for an accurate and robust implementation of MC dose calculation in tomorrow's radiotherapy delivery. We begin by developing a novel method by which an accelerator model can be commissioned to accurately reproduce the output of the true accelerator by simply optimizing the energy and intensity distribution of the incident electron beam.

Chapter 3

Inference of the Optimal Pre-Target Electron Beam Parameters in a Monte Carlo Virtual Linac Model Through Simulated Annealing

Based on Bush *et al.*, Med. Phys. **36**, 6 (2009)

3.1 Introduction

The sensitivity of megavoltage Monte Carlo simulations to the pre-target electron beam parameters in medical linear accelerator Monte Carlo (MC) models has been thoroughly investigated. A comprehensive review of past research in this area is presented by Verhaegen and Seuntjens [Verhaegen and Seuntjens, 2003] and more recently by AAPM TG report No. 105 [Chetty et al., 2007]. The intensity distribution of the pre-target electron beam is among the most sensitive parameters of a medical linear accelerator model [Sheikh-Bagheri and Rogers, 2002b; Keall et al., 2003] . It is well known that off-axis dose profiles are particularly sensitive to the pre-target electron intensity distribution [Keall et al., 2003; Sheikh-Bagheri and Rogers, 2002b; Chibani and Ma, 2007; de Smedt et al., 2005; Tonkopi et al., 2005; Tzedakis et al., 2004]. The general restriction of a Gaussian pre-target electron beam intensity distribution has been consistently implemented in MC simulation of Varian accelerators with variations of energy and full-width half maximum (FWHM) of the beam intensity. The assumption of a Gaussian electron intensity distribution is, in part, based on an educated guess by the physicist (derived from beam line optics/accelerator physics), approximate recommendations by accelerator manufacturers, and in part implied from focal spot measurements sparsely published thus far in the literature [Huang et al., 2005; Jaffray et al., 1993; Loewenthal et al., 1992; Lutz et al., 1988; Munro et al., 1988].

Some of the first published focal spot measurements were produced by Lutz *et al.* [Lutz et al., 1988] who performed measurements of the emerging radiation field from the target using a beam spot camera technique. The measurements were limited to an 8 MV linear accelerator (linac) for which the particular model was not published. For the purpose of investigating modulation transfer functions (MTF's) of radiotherapy portal imaging devices, Loewenthal *et al.* [Loewenthal et al., 1992]

have recorded measurements of the 6 MV and 18 MV focal spot sizes on a Clinac 1800 accelerator. The measurements were made using a slit camera technique. The resolution of the detectors used by both Lutz *et al.* [Lutz et al., 1988] and Loewenthal *et al.* [Loewenthal et al., 1992] was limited and insufficient for precisely determining a pre-target electron intensity distribution for MC simulation.

Using a technique similar to that of Loewenthal *et al.* [Loewenthal et al., 1992], Jaffray *et al.* [Jaffray et al., 1993] used a CT reconstruction technique to make quantitative measurements of the size and shape of the focal spot from a total of nine accelerators. Jaffray *et al.* determined a range for the Clinac 2100c focal spot intensity FWHM of $1.2 - 1.4$ mm for the 6 MV beam and $0.9 - 1.6$ mm for the 18 MV beam. In addition, Jaffray *et al.* measured the shifts in the mean position of the focal spots of dual energy accelerators on the order of 0.8 mm between energy selections of the same linac.

Huang *et al.* [Huang et al., 2005] have published measurements of the focal spots of electron beam's for the Clinac 21EX using the beam spot camera technique of Lutz *et al.* [Lutz et al., 1988]. The work is also useful in the determination of pre-target electron intensities for photon beam models. The measurements of Huang *et al.* [Huang et al., 2005] were the first and only measurements made to date for the purpose of MC simulation. They concluded varying elliptical eccentricities of the focal spot (up to 21%) for electron energies from 6 to 16 MeV with FWHM's in the range of 1.69 mm to 2.24 mm. Lateral shifts in the focal spot were also observed with reported displacements of as much as 7.79 mm.

Based on the above measurements performed thus far in the literature it is clear that the electron focal spot intensities deviate from the ideal Gaussian shape assumed in MC simulation. To the author's knowledge, at the time of this publication, no measurements of pre-target electron beam intensity distributions specifically for use in megavoltage MC photon therapy simulations have been published.

A common method for the determination of the pre-target electron beam parameters for a particular MC simulation (as outlined by Sheikh-Bagheri and Rogers [Sheikh-Bagheri and Rogers, 2002b]) is to begin with a best guess of the electron beam energy and full width half maximum (FWHM) and subsequently perform iterative trial and error adjustments of these parameters until acceptable agreement with measured the dose distribution is achieved. Typically the energy is determined first by varying the electron energy until optimal agreement with measured depth dose profiles is obtained. Adjustments of the FWHM of the Gaussian intensity distribution are then applied until acceptable agreement with lateral (off-axis) profiles is met. It has been shown that the correlation between FWHM and central axis depth dose profile shape is minimal beyond the depth of maximum dose deposition [de Smedt et al., 2005; Keall et al., 2003; Sheikh-Bagheri and Rogers, 2002b]. However, further fine-tuning of the electron beam parameters may be required if the initial guess of FWHM was sufficiently inaccurate during the energy tuning stages. For the remainder of this chapter the above method will be referred to as educated trial-and-error (ETE) commissioning method.

Using an ETE method, the commissioning of a MC model can be laborious, as the time required for the high-statistics simulation of each parameter adjustment is generally large and achieving the optimal combination of electron parameters using a so-called blind search of the solution space is not guaranteed. The process/results from using the conventional method to commission MC linacs are presented by several groups [Keall et al., 2003; Sheikh-Bagheri and Rogers, 2002b; Tzedakis et al., 2004].

Another ETE type method for determining both the pre-target electron energy and FWHM for commissioning a MC model is through comparison of MC calculated lateral profiles in air with measurement. Tonkopi *et al.* [Tonkopi et al., 2005] have investigated the influence of ion chamber response on the MC-based measurement of in-air off-axis ratio (OAR) profiles for megavoltage photon beams. Their work

confirmed the conclusions of Sheikh-Bagheri and Rogers that in-air OAR profiles can be useful in the MC beam commissioning process. The use of OAR profiles could potentially reduce the time required to commission a MC beam by reducing the number of in-water simulations.

Often, after carefully modeling the accelerator to the best-known specifications the accelerator model's output cannot be made to acceptably match measured profiles, especially for the case of higher energy large fields. Resulting dose profiles based on the ETE commissioning methods have been shown at times to deviate substantially from measurement [Chibani and Ma, 2007; de Smedt et al., 2005]. Chibani and Ma [Chibani and Ma, 2007] recently investigated the effects of modifying the dimensions and of the accelerator components to improve dose profile agreement for their Clinac 21EX 18 MV MC model. The discrepancies, first shown by Ding [Ding, 2002], were found to be present in the build-up region of the depth dose profiles of the 18 MV beam. Chibani and Ma concluded that improved depth-dose curve agreement was achieved in the build-up region when using a larger primary collimator bore than specified by the manufacturer, as well as including the lead shield and mirror frame accelerator head components in their simulation. Explicit modeling of the ion chamber geometry has also been found to improve agreement [McEwen et al., 2008]. Alternatively/additionally, recent improvements to BEAMnrc/EGSnrc transport parameters have also been implemented for the purpose of correcting the 18 MV surface dose discrepancy [Rogers et al., 2006].

The sensitivity of the MC model to the incident energy has also been thoroughly investigated [de Smedt et al., 2005; Keall et al., 2003; Sheikh-Bagheri and Rogers, 2002b; Tzedakis et al., 2004; Faddegon and Blevis, 2000; Mohan et al., 1985; Sheikh-Bagheri and Rogers, 2002a]. It has been shown that while the simulation is highly sensitive to the mean electron energy, the energy distribution has little effect on the resulting beam [de Smedt et al., 2005; Sheikh-Bagheri and Rogers, 2002b].

After performing a thorough search of pre-target electron energies and intensity distributions in 18 MV 40×40 cm^2 MC simulations, in-water profile agreement with measurements was achievable to within $\sim$2%. However, a closer analysis of the profiles revealed a systematic disagreement between MC and measured lateral dose profiles outside of the 1σ uncertainty level. The depth dose profiles were found to be in good agreement with measurement with the exception of the build up region in accordance with results previously shown by Ding [Ding, 2002].

The purpose of this chapter is to develop an efficient method for the determination of the optimal intensity distribution of the pre-target electron beam able to most accurately reproduce a set of measured photon field profiles for a given accelerator structure and incident electron beam energy. To achieve this, a novel method has been developed by which the pre-target electron beam intensity distribution can be *inferred* by employing a simulated annealing optimization algorithm. The method has the potential to substantially speed up the parameter selection in the computational stages of the commissioning process and also allows investigation of the effect of deviating from a pure Gaussian intensity distribution.

3.2 Materials and Methods

3.2.1 Monte Carlo Simulation Parameters

MC simulations were made using the BEAMnrc [Rogers et al., 1995] and DOSXYZnrc [Walters et al., 2005] MC code system, based on the underlying EGSnrc [Kawrakow and Rogers, 2000] particle transport code. The following MC transport parameters were used in all simulations: AP=PCUT=0.010 MeV and AE=ECUT=0.700 MeV (including rest mass), where AP and AE are the low-energy thresholds for the production of secondary bremsstrahlung photons and knock-on electrons, respectively, while PCUT and ECUT define the global cutoff energy for photon and electron transport, respectively. Directional bremsstrahlung splitting (DBS) was used with a splitting

factor NBRSPL=1000. Koch and Motz (KM) bremsstrahlung sampling was used for 18 MV simulations. The accelerator model, a Varian Clinac 21EX (Varian Medical Systems, Palo Alto, California), was defined exactly by specifications provided by the 1996 Varian Oncology Systems Monte Carlo Project package. The model does not contain recent modifications to the target location or the lead shielding located in the treatment head determined by Chibani and Ma [Chibani and Ma, 2007].

3.2.2 Measured data

Measured data for depth dose and lateral profile comparisons were obtained from departmental quality assurance archives. The measurements were taken using an IC-15 ionization chamber (volume = 0.13 cc, cavity length = 5.8 mm) within a Scanditronix Wellhofer Blue Phantom water tank with a scanning volume of 48.0 × 48.0 × 48.0 cm. For measured profile and depth dose data displayed in this chapter, an average of 4 independent measurements, taken at different times, was calculated. From this data an objective profile fit was produced for use in the optimization of the electron intensity.

3.2.3 Determination of the pre-target electron energy range

The method begins with the determination of a pre-target electron energy range to be optimized by observing the agreement of MC calculated depth-dose curves with measurement. Because of the relatively weak dependence of depth-dose curves with modification of the incident electron intensity distribution [Keall et al., 2003; Sheikh-Bagheri and Rogers, 2002b], those energies producing unacceptable depth-dose curve agreement (>1%) beyond the build-up region were not used in the optimization. The range of incident electron energies examined was chosen in accordance with energies examined by Keall *et al.* [Keall et al., 2003] for the Clinac 21EX and based on experience from previous commissioning efforts by the authors. Specifically 17.0, 18.0, 18.5 and 19.0 MeV were used. In each simulation, the FWHM was set to 1.3

mm. This FWHM was chosen based on the measurements of Jaffray *et al.* [Jaffray et al., 1993]. While Jaffray *et al.* measured photon spot sizes, Keall *et al.* [Keall et al., 2003] found that the initial electron distribution is approximately equal to the bremsstrahlung radiation distribution on the target, and therefore the FWHM value given by Jaffray *et al.* can be used as an estimate of electron FWHM.

Dose was calculated in a $50 \times 50 \times 50$ cm^3 water tank phantom with a voxel dimension of $0.5 \times 0.5 \times 0.5$ cm^3. Energies found to produce depth dose curves in acceptable agreement with measured depth dose curves were used in the simulated annealing optimization.

3.2.4 Determination of the optimal intensity pre-target electron intensity distribution for the selected energy set

Subsections *(i)* - *(vi)* were repeated for each incident electron energy.

(i) Simulation of annular fluence regions

The simulation of annular fluence regions begins from a cylindrically symmetric mono-energetic pre-target electron beam (radius 0.5 cm) of uniform intensity. This beam is subdivided into annular regions of particle fluence. Particles from each region are transported through the accelerator head (Figure 3.1 *top*) and into a $50 \times 50 \times 50$ cm^3 water tank phantom (SSD = 100.0 cm) with a voxel dimension of $2.0 \times 2.0 \times 1.0$ cm^3 (the smallest voxel dimension was oriented with depth). The cross-plane voxel dimensions were chosen in a balance of reducing the dose variance in the lateral profile direction while maintaining dose resolution. Each dose distribution was scored as a separate 3-D dose matrix. In all cases 34 annuli with equal widths of 0.015 cm were used as defined in Figure 3.1 *(bottom)*. From each annular fluence, 360 million histories were simulated for a statistical uncertainty of $\sim$0.4% within the region of uniform dose.

The use of phase spaces, and hence the introduction of latent variance [Sempau

et al., 2001], was avoided by incorporating BEAMnrc into the DOSXYZnrc simulations as a shared library (isource 9). Division of the electron beam into annular sub-regions was accomplished using a BEAMnrc component module (ANNULI) (written specifically for this purpose). The placement of the ANNULI module with respect to the other accelerator components is shown in Figure 3.1 *(top)*. The module operates by translating each incident particle's position to a new position within the annuli to be simulated, sampled proportionally with increasing R. In all cases a mono-directional, circular pre-target electron beam was used.

The new random radius R and azimuthal angle ϕ are calculated as

$$R = \sqrt{R_1^2 + G_1(R_2^2 - R_1^2)} \quad \text{and} \tag{3.1}$$

$$\phi = 2\pi \times G_2, \tag{3.2}$$

where R1, R2 are the inner and outer radii of the annuli and G1, G2 are uniform random numbers where $0 \leq G_1 \leq 1$ and $0 \leq G_2 \leq 1$.

It then follows that the particle's new Cartesian position (X,Y) is given by

$$X = R\cos(\phi) \quad \text{and} \tag{3.3}$$

$$Y = R\sin(\phi). \tag{3.4}$$

Alternatively, the subdivision of the pre-target electron beam into annular fluence regions could have been accomplished by writing a BEAMnrc source routine in place of the ANNULI component module. The component module approach was implemented to avoid introducing modifications into the BEAMnrc source code and facilitate "plug and play" with other BEAMnrc distributions.

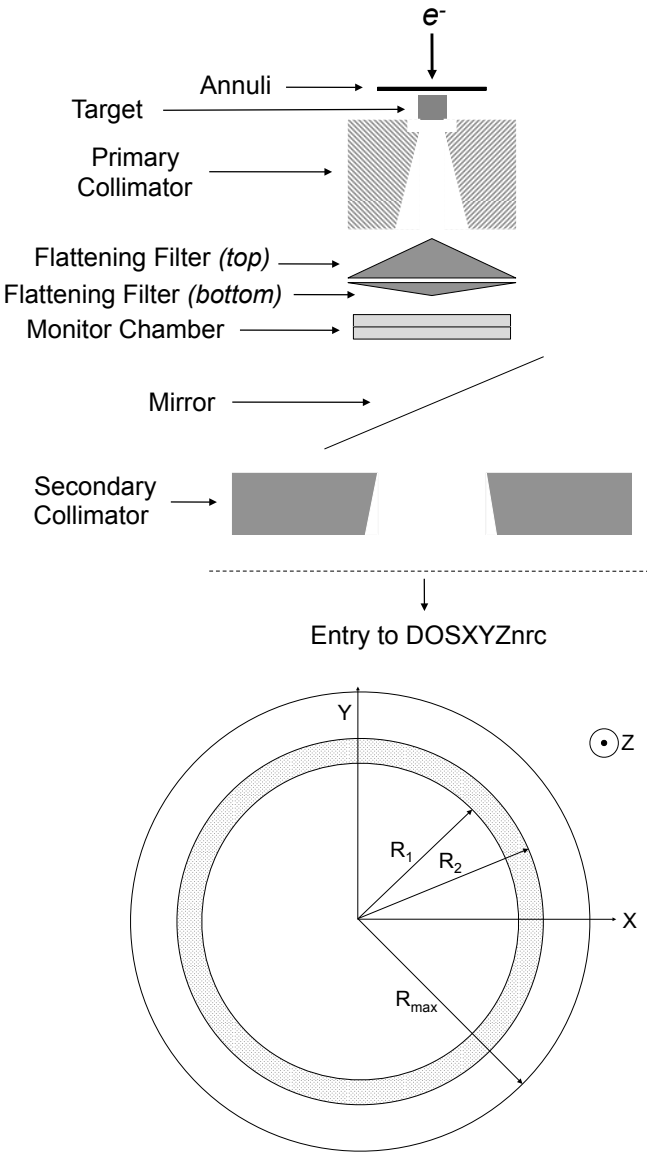

Figure 3.1: Position of the ANNULI component module with respect to the other components of the Clinac 21EX MC model *(top)*. Annular fluence assignment within the ANNULI module *(bottom)*.

(ii) Simulated annealing optimization

Once the dose distributions of all annular fluence regions were collected a search of scaling factors for each dose distribution was performed. A simulated annealing based search algorithm with a least squares cost function was implemented for this task. The cost function to evaluate the goodness-of-fit was defined as

$$C = \sum_n (D_n^{measured} - D_n^{MC})^2, \tag{3.5}$$

where $D_n^{measured}$ and D_n^{MC} are the measured and MC calculated doses to voxel n. The MC calculated dose, $D_n^{MC}(N)$, is calculated as a weighted sum of the annular doses by

$$D_n^{MC} = \sum_N W(N) \cdot D_n^{MC}(N), \tag{3.6}$$

where *W(N)* are the scaling factors for annular region N and $D_n^{MC}(N)$ is the MC calculated dose to voxel n from annular region *N*.

The search for the optimal set of scaling weights, *W(N)*, is carried out such that in every iteration of the search a small weight change to a random *W(N)* is made. Changes bringing the *scaled sum of annular doses* closer to measurement are immediately accepted while changes worsening the agreement are rejected with a given probability as governed by a Boltzman-based "cooling schedule"

$$P = e^{-\frac{C_{i+1}-C_i}{kT}}, \tag{3.7}$$

where the temperature T is decreased linearly each iteration of the search, C_{i+1} and C_i are the calculated costs for the current and previous iterations and k is an arbitrary constant.

It is important to note that a change in scaling factor $W(N)$ is isomorphic with a

change in the electron intensity originating from annular region N. The determination of optimal scaling factors $W(N)$ therefore yields a solution for the optimal pre-target electron intensity distribution.

(iii) Optimization of Gaussian electron intensity distributions

The first application of the simulated annealing algorithm described above was a minimization of Equation 3.5 with the aim of finding the best Gaussian distributed scaling weight set $W(N)$. By achieving a global minimum of the cost function a best possible agreement for the given electron energy was found.

The measured dose $D_n^{measured}$ was limited to a diagonal profile from an 18 MV 40×40 cm^2 field at a depth of 3.5 cm in water. It should be noted that the algorithm is not limited to 1-D profiles and is capable of performing the optimization on 3-D dose distributions as well as multiple 1-D profiles. The MC calculated annular dose D_n^{MC} was similarly chosen from each annular fluence region from voxels subtending depths of 3.0 - 4.0 cm in the water tank model previously described. To reduce statistical variance, the mean dose of the diagonal profiles was calculated. Voxels in the penumbral region were omitted to avoid introducing bias from the MC voxel size in regions of steep dose gradients.

During each iteration of the Gaussian optimization the complete set of scaling factors $W(N)$ is resampled by making a random change to the Gaussian FWHM. The iterations are terminated when a global minimum of the cost function (i.e. a best fit of the weighted sum of annular dose distributions with the measured dose distribution) is achieved. The FWHM of the Gaussian scaling factors is then recorded, to be later integrated in the pre-target electron beam Gaussian source model. The range of FWHM's permitted in the search was limited to 0.0 - 0.5 cm as any solution outside of this range would be grossly unphysical.

(iv) Optimization of unrestricted electron intensity distributions

In a second application of the optimization method the restriction of scaling weights being normally distributed is lifted from the optimization. By doing so, the algorithm was free to seek out the best possible agreement between measured dose distributions and the weighted sum of annular dose distributions, with no implied Gaussian correlation between scaling weights. For the optimization all scaling factors $W(N)$ were arbitrarily initialized to 1.0, and scaling factor changes (randomly) up to 100% were permitted. Figure 3.2 displays a sample search for the optimal scaling factors and the associated scaled diagonal dose difference profiles.

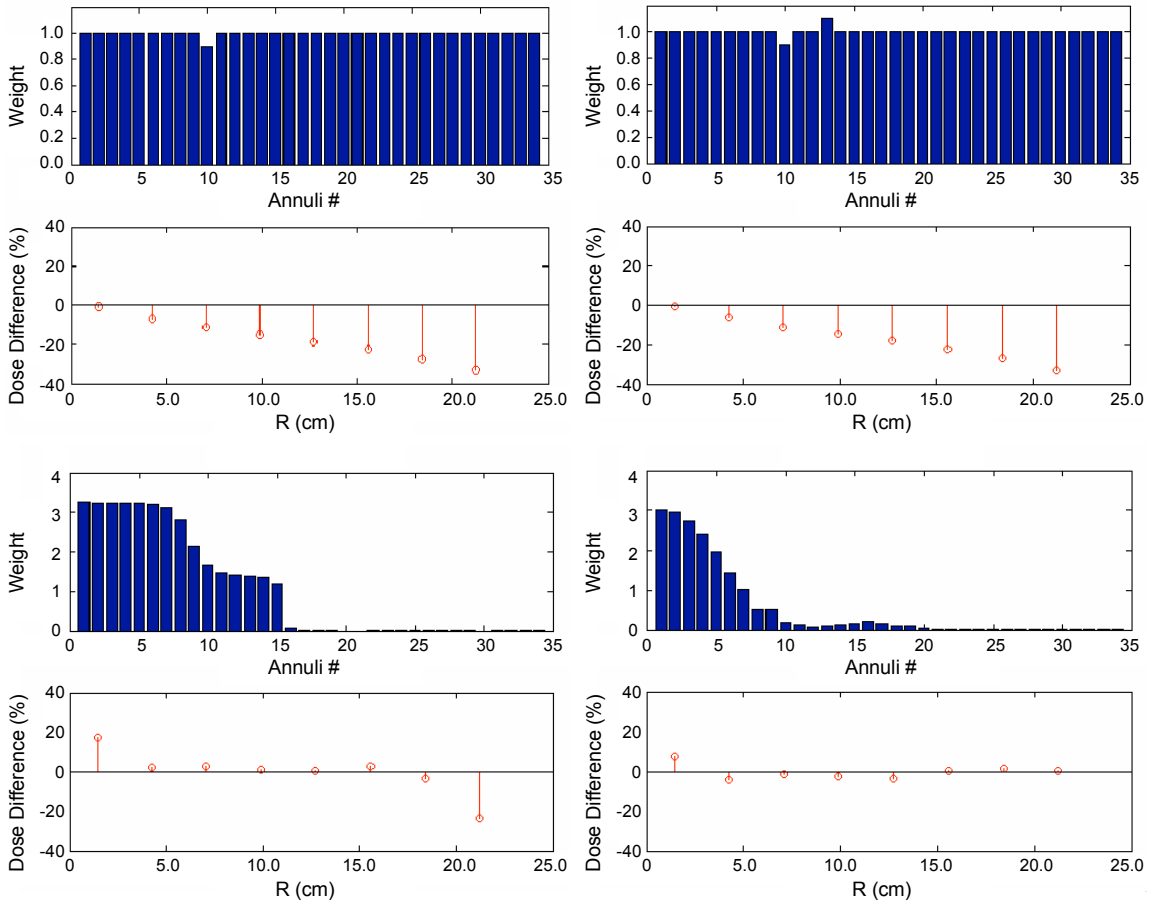

Figure 3.2: Sample search for the optimal set of annular scaling factors (weights) achieving the best agreement with measurement. For each subfigure the upper bar plot displays the set of scaling factors $W(N)$ at a given stage of the optimization, while the lower figure displays a percent dose difference plot of the measured and MC weighted sum dose distributions for a 40×40 cm^2 field at a depth of 3.5 cm. In this example the optimization began with a weight change for annuli #10 *(top left)* followed by annuli #13 *(top right)*. The set of annular weights is also shown at two later iterations (bottom left and right).

***(v)* Incorporating the derived intensity distribution in future simulations**

Once a minimum (global or approximately global) of the cost function has been achieved, the resulting set of annular intensities must be permanently included in the accelerator head simulation. The annular intensities were incorporated into future simulations by the use of a component module. For each particle that enters the component module the radial position is evaluated and the EGSnrc weight variable is replaced by the respective scaling factor. By replacing the particles weight with the optimally determined annular weight the absorbed dose resulting from this particle is effectively scaled by the optimally determined weight. Alternatively, the weights derived from the optimization could be used to construct a characterized source for input into BEAMnrc.

***(vi)* Verification of incident electron intensities with alternate field sizes**

The electron beam intensity distribution is optimized based on the diagonal dose profiles from a 40×40 cm^2 field. The assumption was therefore made that the optimized electron intensity would produce good profile agreement for other field sizes. Verification of the optimized electron intensity was performed by comparing MC calculated and measured 10×10 cm^2 and 4×4 cm^2 lateral and depth dose profiles. MC simulations were performed with a voxel size of $0.5 \times 0.5 \times 0.5$ cm^3 at an SSD of 100.0 cm.

***(vii)* MC modeling of the focal spot image and the effect of the flattening filter on the focal spot image**

To allow comparison of the inferred pre-target electron intensity distribution with slit-type measurements performed in the literature [Jaffray et al., 1993; Sham et al., 2008], an analysis of photon fluences collected within the accelerator head was performed using a directional cosine rejection filter and radially binning the fluence into 30 equal area bins covering the entire aperture of the primary collimator. The directional

cosine rejection filter was designed to reject photons with a Z-directional cosine that deviated from the central axis more than 0.0246 degrees. This angle was chosen to correspond to that described by Sham *et al.* in their slit-type measurement of the electron beam using a 0.3 mm slit opening positioned 70.0 cm from the target. The radial bin size used was 0.15 mm.

The above analysis was performed for fluences resulting from the unrestricted optimization of the pre-target electron beam. The fluences were collected at the downstream face of the primary collimator, as well as at the downstream face of the flattening filter. For comparison, the photon fluence resulting from an optimized Gaussian pre-target electron intensity was also analyzed at the downstream face of the flattening filter. In each case 125 million particles were modeled.

In addition, to observe the differences in photon fluences between Gaussian and unrestricted optimized pre-target electron beams, photon fluences at the base of the primary collimator were radially binned using 30 equal area bins covering the entire aperture of the primary collimator.

3.3 Results

3.3.1 Determination of the pre-target electron energy range

The depth dose curve agreement test applied to the set of incident electron energies (17.0, 18.0, 18.5, and 19.0 MeV) resulted in all energies passing an acceptance criterion ($< 1\%$) beyond a depth of 3.5 cm. A similar finding was reported by Keall *et al*[Keall et al., 2003]. The simulated annealing search was therefore performed for an optimal pre-target electron intensity distribution for 17.0, 18.0, 18.5, and 19.0 MeV. The overall best match between measured and MC calculated depth dose profiles for the authors' 18 MV model was determined to be 18.0 MeV when using a mono-energetic, mono-directional electron source with an estimated FWHM of 1.3 mm.

3.3.2 Simulation of annular fluence regions

Figure 3.3 *(top)* displays a sample particle position plot of the 18 MeV pre-target electron beam and the assignment of annular sub-regions (only every second annuli displayed for clarity). MC calculated diagonal dose profiles scored in water at a depth of 3.5 cm (in units of dose per incident particle) from the 34 annular pre-target fluence regions are shown in Figure 3.3 *(bottom)* for a secondary collimator setting of 40×40 cm^2.

3.3.3 Optimization of Gaussian electron intensity distributions

Table 3.1 summarizes the optimal agreement with measured lateral profiles for the set of pre-target electron energies used in Gaussian restricted optimizations. The resulting optimized radial intensity profiles for the selected electron energies are displayed in Figure 3.4 *(top)*.

Table 3.1: A comparison of optimization results for electron energies examined for the 18MV Clinac 21EX model. Estimated uncertainty on the least significant digit is displayed in brackets.

e- Energy (MeV)	Optimal Gauss. FWHM (mm)	Rel. RMSE (Gauss.)	Rel. RMSE (Unrestricted)
17.0	1.67(1)	6.17	1.07
18.0	1.34(1)	3.25	1.00
18.5	1.19(1)	2.69	1.84
19.0	1.06(1)	2.24	2.23

Diagonal dose profiles resulting from the optimized intensity distributions are shown in Figure 3.5 *(top)* along with diagonal dose profile measurements for a 40×40 cm^2 field at 3.5 cm depth.

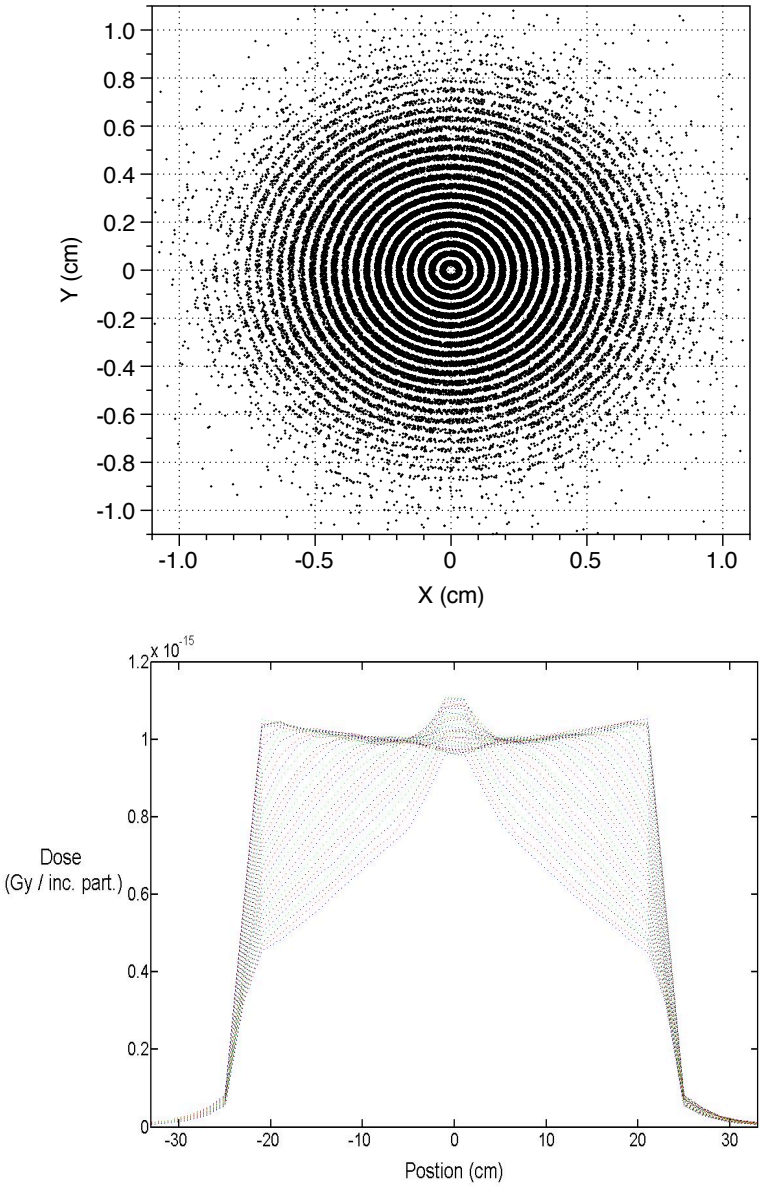

Figure 3.3: Sample particle position plot of the 18 MV pre-target electron beam after assignment of annular sub regions *(top)*. Every second annuli is displayed for demonstration purposes only. MC calculated diagonal water dose profiles of 34 annular fluence regions from a uniform intensity source are shown at a depth of 3.5 cm *(bottom)*. In this plot the lower curves are produced by the outermost annuli.

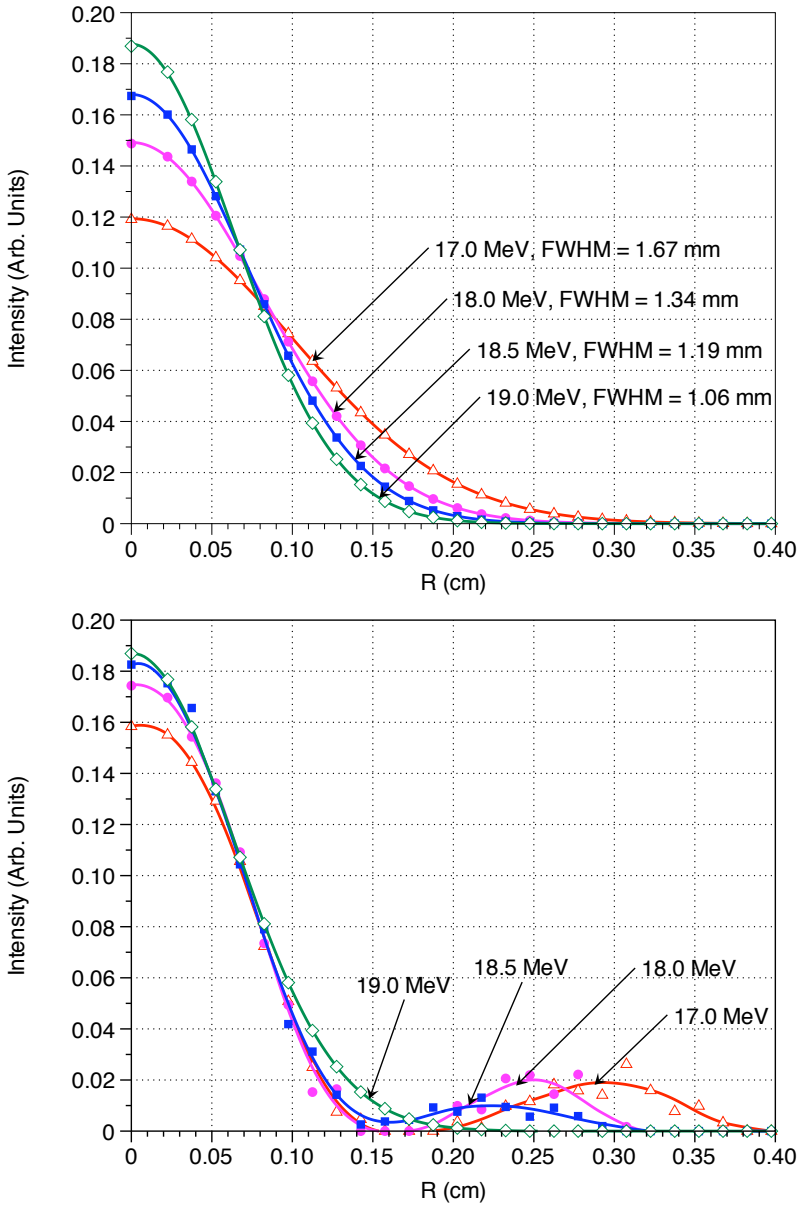

Figure 3.4: Optimized radial intensity profiles for the selected set of pre-target electron energies. Each intensity profile is the result from a simulated annealing optimization using Gaussian *(top)* and unrestricted *(bottom)* annular scaling factors.

3.3.4 Optimization of unrestricted electron intensity distributions

The resulting optimized radial intensity profiles for the selected electron energies are displayed in Figure 3.4 *(bottom)*. The agreement with measured lateral profiles for the set of pre-target electron energies in all unrestricted optimizations is shown in Table 3.1. It is important to note that during the optimization the scaling factors were com-

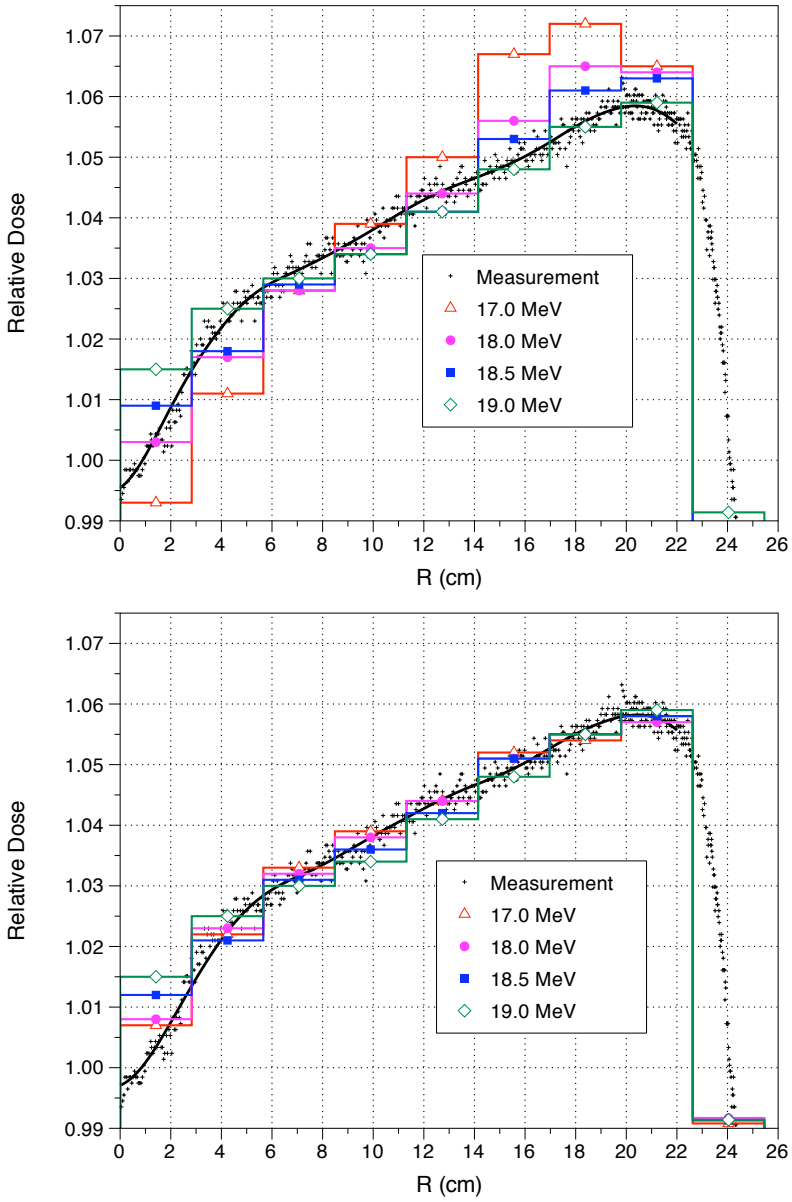

Figure 3.5: Optimized 18 MV MC calculated 40×40 cm^2 diagonal dose profiles in water compared with measurement (fit and raw data) for the selected set of pre-target electron energies and optimized intensity distributions as displayed in Figure 3.4. For each energy a simulated annealing optimization using Gaussian *(top)* and unrestricted *(bottom)* annular scaling factors was performed.

pletely unrestricted (with the exception of negative values) and no prior knowledge of the intensity distribution was implied. The overall optimal intensity distribution was determined to be a solution that is Gaussian-like with a FWHM=1.10(1) mm at an energy of 18.0 MeV. In addition, the solution contains an extra focal halo component

on the order of 10% of the central peak intensity.

Diagonal dose profile comparisons resulting from the unrestricted optimization of electron intensities (displayed in Figure 3.4 *bottom*) are shown in Figure 3.5 *(bottom)* along with diagonal dose profile measurements for a 40×40 cm^2 field at 3.5 cm depth. From this plot the improved agreement with measured profiles is demonstrated.

In Figure 3.6 the observed differences of in-water lateral dose profiles compared with measurement are displayed along with difference plots for the optimized 18.0 MeV electron beam for both the Gaussian intensity *(top)* and unrestricted intensity *(bottom)*. A systematic discrepancy between MC and measured profiles is visible when restricting the intensity to Gaussian distributions. By lifting the Gaussian restriction, the root-mean-square-error (RMSE) was reduced by a factor of 3.9.

3.3.5 Verification of incident electron intensities with alternate field sizes

Verification simulations of the derived electron intensity distributions (originally derived for the 40×40 cm^2 field) were performed for secondary collimator settings of 10×10 cm^2 and 4×4 cm^2. The resulting lateral and depth dose profiles with dose differences displayed within a fiducial region are shown in Figure 3.7 along with the respective measured profiles.

3.3.6 MC measurement of the focal spot image and the effect of the flattening filter on the focal spot image

In Figure 3.8 the photon intensity distributions after application of the directional cosine rejection filter are displayed for a Gaussian pre-target electron beam at the base of the flattening filter, and free optimized pre-target electron beam at the base of the primary collimator and at the base of the flattening filter. The result displays the blurring effect that the flattening filter has on the focal spot images.

In Figure 3.9 the relative photon intensity profiles at the base of the primary

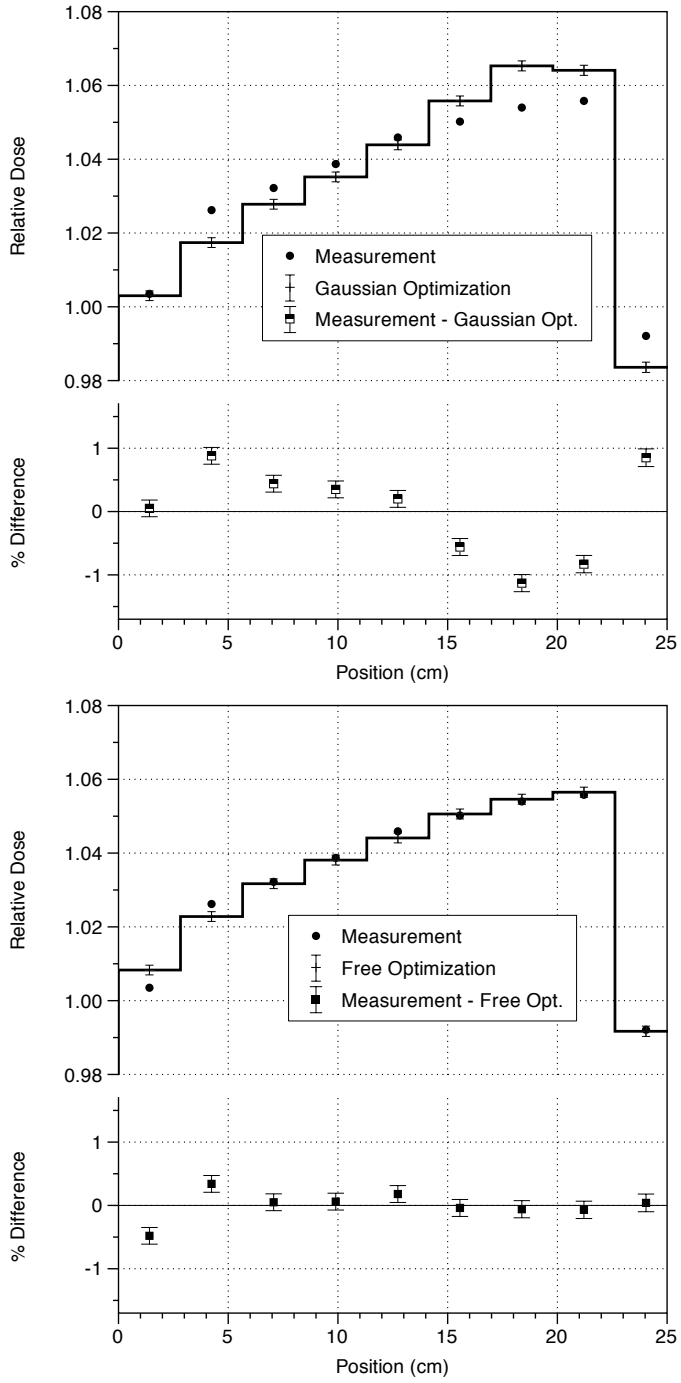

Figure 3.6: Measured and MC calculated diagonal dose profiles from a 40×40 cm^2 field in water at a depth of 3.5 cm for 18.0 MeV Gaussian (top, RMSE = 0.59%) and unrestricted (free) optimized (bottom, RMSE = 0.15%) pre-target intensity distributions. When using a Gaussian pre-target electron intensity distribution, a systematic discrepancy is present even after optimization. The statistical uncertainty was calculated for MC data only.

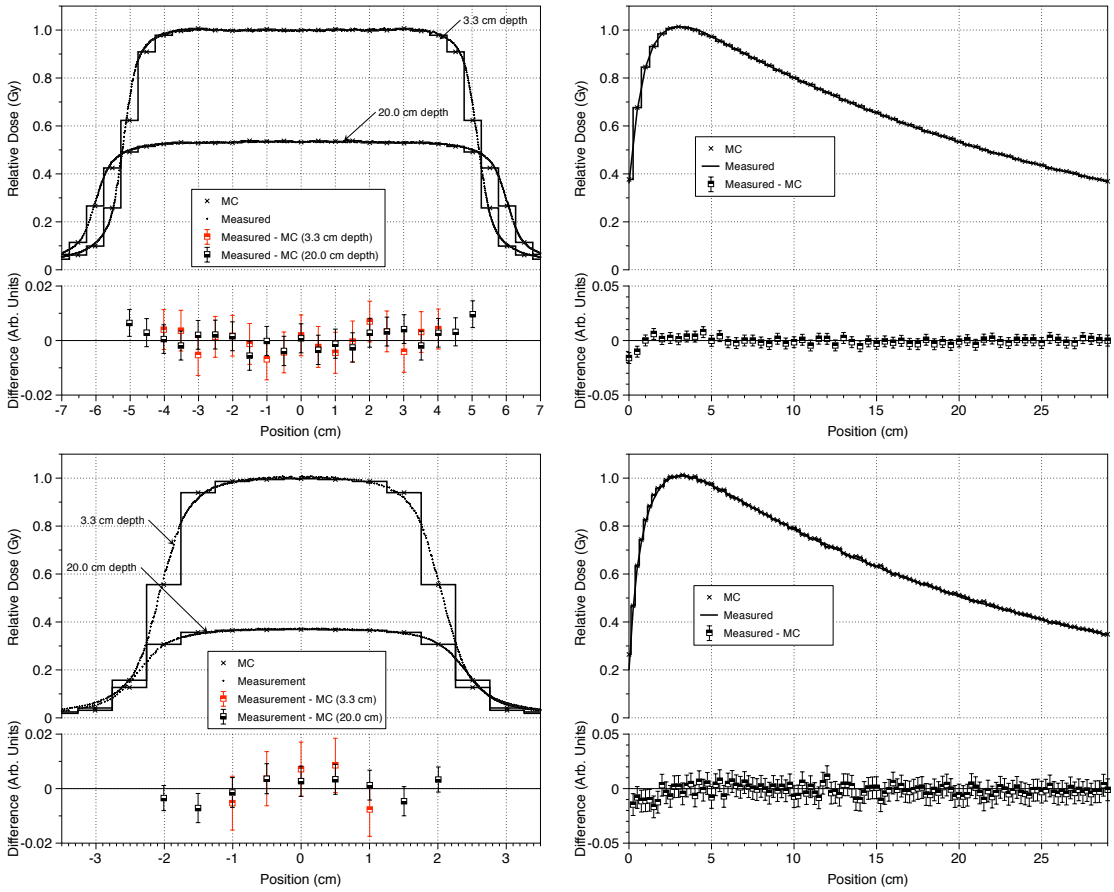

Figure 3.7: MC calculated lateral (*top left*, RMSE = 0.32%) and depth dose (*top right*, RMSE = 0.20%) profiles from a 10×10 cm^2 field at depths of 3.5 cm and 20.0 cm calculated using the optimized intensity distribution are shown versus measured dose. MC calculated lateral profiles at depths of 3.5 cm and 20.0 cm (*bottom left*, RMSE = 0.49%) and depth dose curves (*bottom right*, RMSE = 0.38%) from a 4×4 cm^2 field are also shown versus measurement.

collimator for best Gaussian and free optimized electron intensity distributions are displayed. A relative intensity profile from particles originating from the extra focal halo region is also plotted for comparison. The subtle differences in relative intensity between the best Gaussian and unrestricted (free) optimized electron intensity distributions are shown in the difference plot.

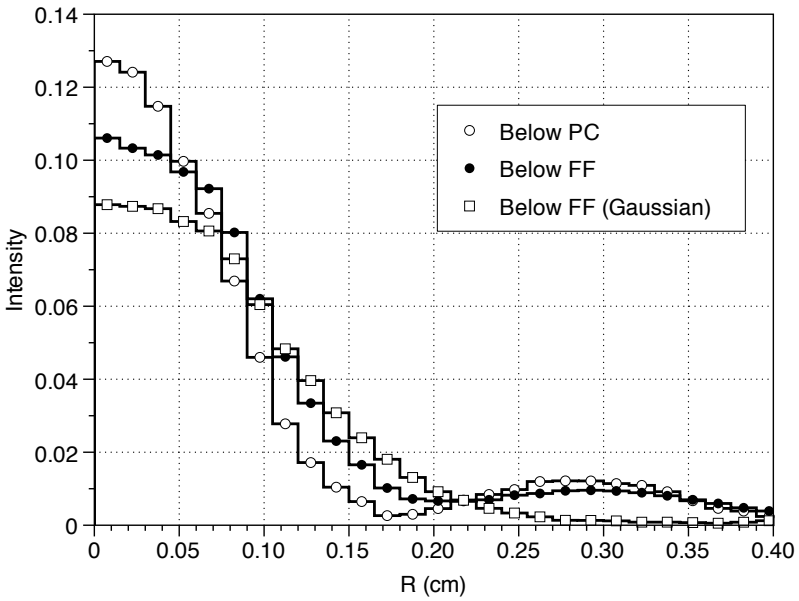

Figure 3.8: Focal spot intensity profiles at the base of the primary collimator (PC) and at the base of the flattening filter (FF) calculated using the directional cosine rejection filter, demonstrating the potential signal observed from a slit-type focal spot measurement.

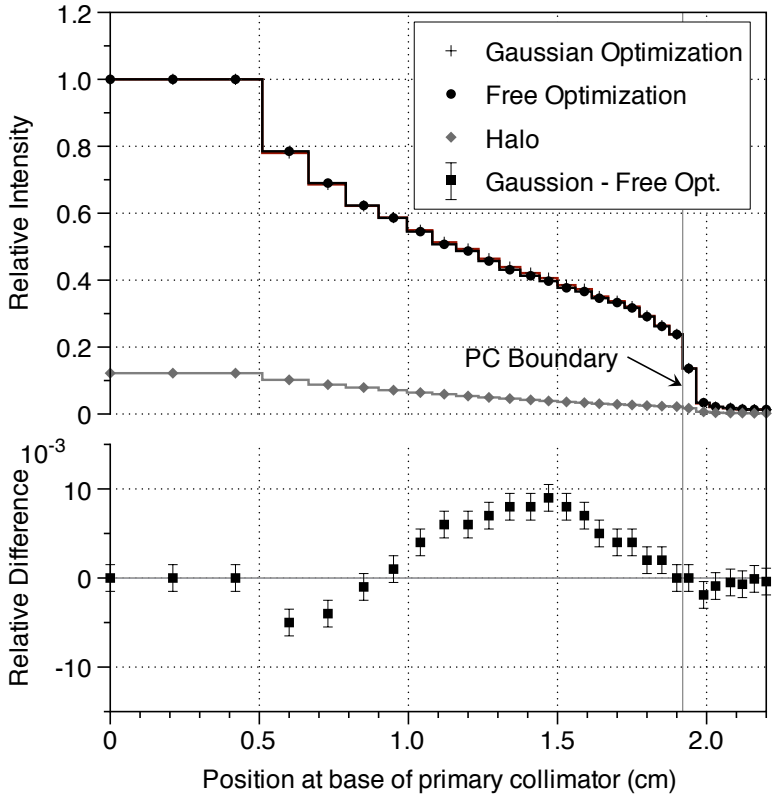

Figure 3.9: Relative photon intensity profiles and relative differences at the base of the primary collimator from best Gaussian and unrestricted (free) optimized electron intensity distributions. Subtle differences between "Gaussian Optimization" and "Free Optimization" data are only visible in the relative difference plot *(below)*. The contribution from particles originating in the extra focal halo region is also plotted.

3.4 Discussion and Conclusions

A technique has been developed to improve the commissioning of a MC accelerator capable of producing dose distributions in better agreement with measurement than previously possible with conventional commissioning methods. By implementing a simulated annealing search of the electron beam intensity distribution, a best-fit solution can be obtained at a given pre-target electron energy.

The optimization technique was applied to the Varian 18 MV Clinac 21EX MC model as the 18 MV configuration presented more modeling difficulties than the 6 MV configuration. The method could equally be applied to MC models of other accelerators and beams including those for electron therapy. Given the current method, the pre-target electron beam is required to possess cylindrical symmetry. Future research may include investigating the use of alternative shaped fluences other than cylindrical annuli to allow the technique to be applied to other accelerator models with non-cylindrical pre-target electron intensity distributions.

Tuning of the simulated annealing optimization parameters was required to avoid trapping in local minima solutions along the path to the optimal solution. However, in the author's experience, the solution space for the optimal electron intensity distribution contained many convex surfaces in the region of the global minimum which did not vary significantly in cost. The small differences between local minima solutions in this region also had minimal effect on the resulting dose distribution. The optimization did not require a significant amount of time for completion ($\sim$10 minutes on a single 2.2 GHz processor) and so the efficiency improvement from implementing a faster optimization was not explored. The collection of the low variance dose distributions from annular electron fluences was the most computationally demanding component of the method. However, these data only need to be collected once for each beam energy and accelerator model.

When restricted to Gaussian pre-target electron intensities the optimally determined solution for the 18 MV Clinac 21EX model was found to be Energy = 19.0 MeV, FWHM = 1.06(1) mm, yielding in-water 40×40 cm^2 lateral dose profiles at a depth of 3.5 cm that were in agreement with measurement with a RMSE = 0.34%. However, analysis of the entire set of optimized data lead to the conclusion that, when considering smaller field and depth dose agreement with measurement, the Energy = 18.0 MeV, FWHM = 1.34(1) or Energy = 18.5 MeV, FWHM = 1.19(1) are preferred without considerable increase in the RMSE. All values of Gaussian electron beam FWHM are within the measurements made by Jaffray *et al.* of 0.9 - 1.6 mm [Jaffray et al., 1993].

Lifting the restriction of a Gaussian pre-target electron intensity resulted in a solution for the 18 MV Clinac 21EX model with a Gaussian-like intensity (Energy = 18.0 MeV) with the presence of an extra-focal halo contribution peaked at 2.4 mm off axis (Figure 3.4 bottom). The FWHM of the central peak of this distribution was found to be 1.10(1) mm. The extra focal component of the intensity has proven to be essential in achieving the best possible agreement with measurement (RMSE = 0.15%).

In the case that the geometry and composition of all essential linac head components were known to a high degree of precision and the modeling of bremsstrahlung production was also known with great precision, one could infer that the optimized pre-target electron intensity distributions reflect reality. In practice, neither geometry of linac nor modeling of bremsstrahlung production can be claimed to be established to the required precision. A comprehensive benchmark of the Monte Carlo modeling of bremsstrahlung by Faddegon *et al.* [Faddegon et al., 2008] has determined the photon yields in EGSnrc (up to 15 MV, for Al and Pb targets) to be within agreement with the measurement which had an accuracy of ±5%. It can be argued that even a much smaller (∼1.5%) error in the modeling of bremsstrahlung angu-

lar yield alone is sufficient to compensate for the difference between the "Gaussian" and "free-optimization" profiles shown in Figure 3.6. In conclusion, a considerably higher accuracy of at least 1% would be required to state that the inferred pre-target intensity distributions reflect reality, rather than a calculation artifact.

For the MC model used in this paper (1996 Varian Oncology Systems - Monte Carlo Project package) the simulated annealing optimization required the presence of an extra focal electron intensity contribution to achieve the best overall agreement with measured profiles. While it would certainly be interesting if the extra focal electron intensity were a measurable effect, it may be an indication of a deficiency in the MC model used. It would be worthwhile to repeat the optimizations using an accelerator model that includes recently modified specifications from Varian. These specifications confirmed the findings of Chibani and Ma [Chibani and Ma, 2007] which imply additional electron scatter contributions and result in significantly better modeling of the dose in buildup region. To the author's knowledge the only display of lateral profiles obtained using the recent modifications has been published by Chibani and Ma [Chibani and Ma, 2007], Figure 7. In their figure systematic discrepancies with measurements on the order of those reported in Section 3.3 (Figures 3.5 - 3.6 *top*) are somewhat visible and would likely be reduced through optimization of the pre-target electron intensity distribution using the technique described in this chapter. It would be interesting to determine if any deviations from a Gaussian intensity distribution would still be required to achieve a best overall agreement.

A recent experimental investigation by Sham *et al.* [Sham et al., 2008] has measured the focal spot size for a 6 MV accelerator. Their results have implied a radial intensity containing a narrow central peak (with a Pearson VII fit) as well as a broad intensity contribution (with a double Lorentzian fit). The author's calculations for a pseudo slit-type model of the focal spot image (Figure 3.8) have inferred what would be approximately observed from measurement if the extra-focal component of

pre-target electron beam was present. It is worthwhile to note that our model did not include the additional blurring of the intensity profile resulting from radiation passing through the slit, the effect of detector size or imperfections of the experimental setup. Accounting for these extra measurement uncertainties would inevitably blur the profile further than that shown in Figure 3.8, but the extent of this blurring has not yet been determined. The pseudo slit-type model illustrates that with the flattening filter in place, the extra focal electron component would be observed as a broad intensity tail in agreement to the observations of Sham *et al.* for 6 MV. The focal spot image modeled using a Gaussian pre-target intensity distribution did not display a broad intensity tail. Modeling of the experiment with the flattening filter removed suggests that the extra-focal halo, if observable, could be detected with a slit type measurement, provided the resolution of the measurement was sufficient.

The presented method has not been tested and may require modification to achieve optimal agreement with small fields (< 1.0 cm). Scott *et al.* [Scott et al., 2009] have shown that output factors of small fields (0.5 cm - 1.0 cm) are particularly sensitive to the incident electron beam intensity distribution. Their results indicate that the output factors of square fields larger than 1 cm show decreasing dependence on the electron intensity. Therefore, to achieve MC model agreement with measurement for field sizes below 1 cm, the inclusion of output factors in the optimization cost function may be required.

Few comparable published results from the commissioning efforts of other groups are available at this time either due to differences in accelerator models or lack of large lateral field profile comparisons with measurement. Perhaps the most appropriate comparison for 18 MV commissioning of the 21EX showing large fields comes from the work of Keall *et al.* [Keall et al., 2003] in which their 18 MV 21EX model was commissioned to within 1% with a largest reported field size of 25×25 cm^2 and a voxel size of 2.0 cm along the profile direction. Achieving these results required

selection of three parameters: target density, FWHM of the electron intensity, and the electron energy. Hasenbalg *et al.* [Hasenbalg et al., 2007] reported achieving 2% agreement between modeled and measured profiles for the radiation fields of up to 40×40 cm^2 size for a 15 MV beam. Importantly, although these groups were able to achieve acceptable results, ETE approaches to determining the optimal parameters in a multi-dimensional solution space require a considerable amount of time and effort. Using a simulated annealing approach can allow a significant time and effort savings in the computational stages of the commissioning process as well as the ability to achieve better agreement with measured profiles (for larger 40×40 cm^2 fields). In addition, the results can be achieved by varying only the electron intensity profile and energy, arguably the least known parameters in the accelerator model.

It is anticipated the method could also be used in the case where lateral profiles in air are used to determine the optimal energy of incident electrons, optimizing the intensity distribution using measured lateral in-air profiles in place of measured in-water profiles for each energy.

Chapter 4

Latent Phase Space Variance Reduction with Azimuthal Particle Redistribution

Based on Bush *et al.*, Phys. Med. Biol. **52**, 14 (2007)

4.1 Introduction

The ability to record particle characteristics in a phase space file (PSF) is an integral part of the BEAMnrc code [Rogers et al., 1995], allowing the stopping/restarting of simulations, analysis of particle characteristics, modification of particle characteristics, etc. The characteristics recorded in the PSF include particle energy, position, direction cosines, weight, LATCH history, and optionally, the Z coordinate of the last interaction. When modeling an accelerator head for Monte Carlo (MC) simulation, a "two-step" phase space approach is commonly used. In this approach a phase space (PS_A) is often scored in a plane just "downstream" from the accelerator components that remain constant for each simulation. For the Clinac 21EX[1], this plane lies just above the secondary collimating jaws (see Figure 4.1). All future simulations can be started from this plane using PS_A as a particle source, effectively eliminating the need to remodel many of the unchanging linac components for each simulation. A second phase space, PS_B, is commonly used to record the final output of the BEAMnrc simulation and acts as the source for particle transport into a patient model or phantom. The scoring of PS_B can optionally be eliminated in BEAMnrc by incorporating the PS_B simulation as a shared library in DOSXYZnrc.

As addressed by Sempau *et al.* [Sempau et al., 2001], the use of phase space techniques in MC simulation introduces a baseline level of statistical variance that cannot be suppressed through the use of particle recycling techniques. This variance, termed *latent phase space variance*, is due to the finite number of particles stored in a PSF. MC dose uncertainty calculation is comprised of uncertainty components from latent PS variance as well as the variance associated with transporting the particles into a phantom. It is difficult to individually quantify these two components of uncertainty. An approach to quantifying each component is presented by Sempau *et al.*. The latent PS variance component can be a significant limiting factor in achieving

[1]Varian Medical Systems, Palo Alto, California.

accurate, low-uncertainty, dose distributions Gagné and Zavgorodni [2007].

In general, to obtain acceptably low uncertainty results from two-step MC simulations, the size of PS_A must be kept rather large. For larger clinical field sizes, PS_A file sizes are often required to be larger than 1 gigabyte (GB) in order to achieve a statistical uncertainty in the phantom of less than 1-2% with a voxel size of ($0.5 \times 0.5 \times 0.5$ cm^3). To further reduce statistical uncertainty in the MC simulation, one can either increase the size of the intermediate PSF (increase particle density) or recycle the particles that have already been recorded. When a particle is recycled, the PSF record for the particle is reused. The recycled history differs from the original history only by the random number chosen to restart the particle's transport through the remainder of the accelerator model. This method of recycling particles will be referred to as the standard particle recycling (SPR) method. For the remainder of the simulation up to the surface of the phantom, a lack of significant scattering in air creates a situation in which each recycled use of a particular particle is very likely to reach the surface of the phantom at the same location. By simply recycling particles using SPR, the latent variance of PS_A is transported directly to the surface of the phantom.

To reduce latent PS variance Fix *et al.* (2004) have used a PS rotation technique in which BEAMnrc source code has been modified to rotate phase space particles between recycled uses. The degree of variance reduction was not determined in this study.

Tyagi *et al.* [Tyagi et al., 2006] have reported "a proof of principle" for an Adaptive Kernel Density Estimation (AKDE) technique that "has the potential to reduce latent PS variance". This technique as well as the technique used by Fix *et al.* [Fix et al., 2004] utilize cylindrical symmetry in the PS plane. In AKDE new photons are sampled at the level of PS_A based on the estimated trends of the existing photons located at a similar radial distance from the beam's central axis. Electrons

are excluded from AKDE re-sampling. By sampling new photons, the PS plane is "filled out" and the effective PS particle density is increased. AKDE, in theory, may provide a means to reduce latent PS variance for a given number of particles in a PSF. The published results, however, do not demonstrate or conclude any reduction in latent PS variance and offered only similar results to a standard PS recycling technique.

Developers of the BEAMnrc code have also implemented a particle re-distribution technique into the DOSXYZnrc user code initiated through the ISMOOTH [Walters et al., 2005] input parameter. Using this technique, recycled PS particles are re-distributed by mirroring particle positions and directions about the X and Y axis, reducing systematic (latent) uncertainty by exploiting rectangular phase space symmetry. Although simple to use, the technique is limited to radiation fields that are symmetric about the central axis of the accelerator and is only effective up to a maximum of four redistributed positions for each particle (one per field quadrant).

In this chapter, a BEAMnrc component module (MCTWIST) is designed to implement a simple azimuthal particle redistribution (APR) technique that reduces latent variance in PSF based MC simulations. The APR technique differs from SPR techniques in that a random rotation about the beam's central axis is introduced for each recycled use of a particle. For the first time a quantitative approach will be taken to determine the latent variance reduction that can be gained as a result of utilizing cylindrical PS symmetry. It is anticipated that by incorporating the MCTWIST module in MC simulations, considerably more accurate, lower-uncertainty in-phantom dose distributions can be produced by reducing the latent PS contribution to the total dose variance.

The module is unique in a sense that no physical component is added to the accelerator model. Transformations are made directly to each particle's characteristics, independent of BEAMnrc/EGSnrc particle transport. MCTWIST has therefore been

termed a pseudo-component module. This chapter demonstrates both the development and application of MCTWIST in MC simulation.

4.2 Materials and Methods

4.2.1 Azimuthal Particle Redistribution

A powerful feature inherent in the BEAMnrc software architecture is the ability to build accelerator head models with user written component modules (CM's). The MCTWIST CM allows seamless integration into the BEAMnrc system (see Figure 4.1) by replacing a thin slab of air, already existing in the BEAM model, with an air slab that changes particle characteristics according to required transformations.

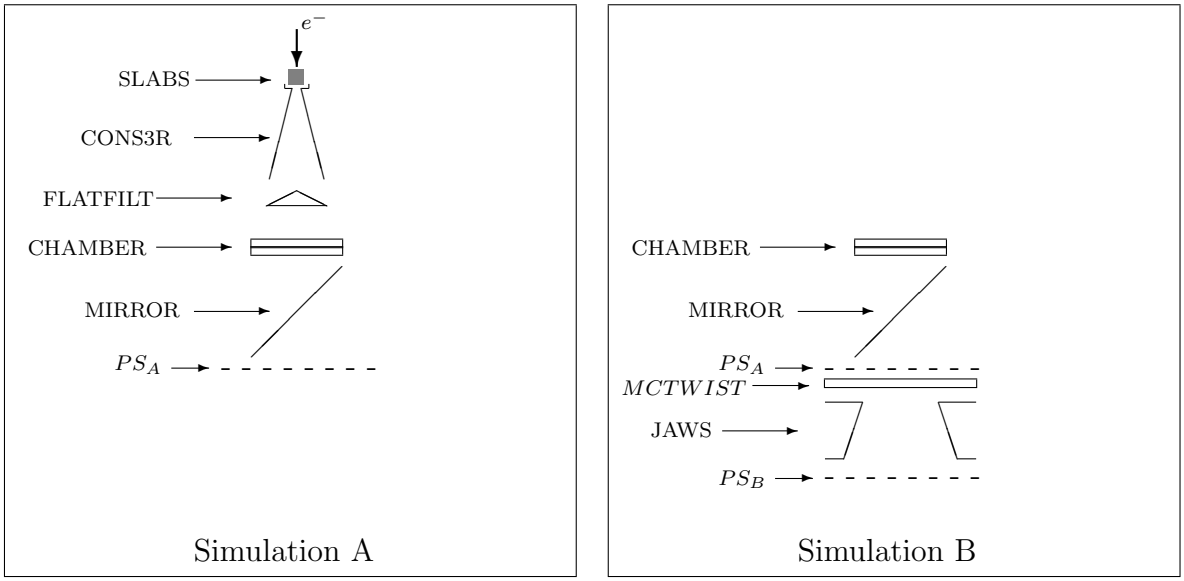

Figure 4.1: Schematics of the Varian 21EX setup and the placement of the MCTWIST module. Simulation A *(left)* models all of the patient independent component modules of the accelerator head: target, primary collimator, flattening filter, monitor chamber and mirror. The resulting phase space (PS_A) is then used as a source for Simulation B *(right)*. The MCTWIST module is inserted immediately following PS_A and above the Secondary collimator (JAWS). For this simulation, the chamber and mirror remain in place to score the backscattered dose to the chamber from the secondary collimator, a requirement for converting the resulting dose distributions to absolute dose using the absolute dose conversion method by Popescu *et al.* [Popescu et al., 2005].

For each instance that a particle enters the MCTWIST module, the particle's radial distance R from the central axis and azimuthal angle ϕ are calculated (see

Figure 4.2) as

$$R = \sqrt{X^2 + Y^2} \quad \text{and} \quad \tan\phi = \left(\frac{X}{Y}\right). \tag{4.1}$$

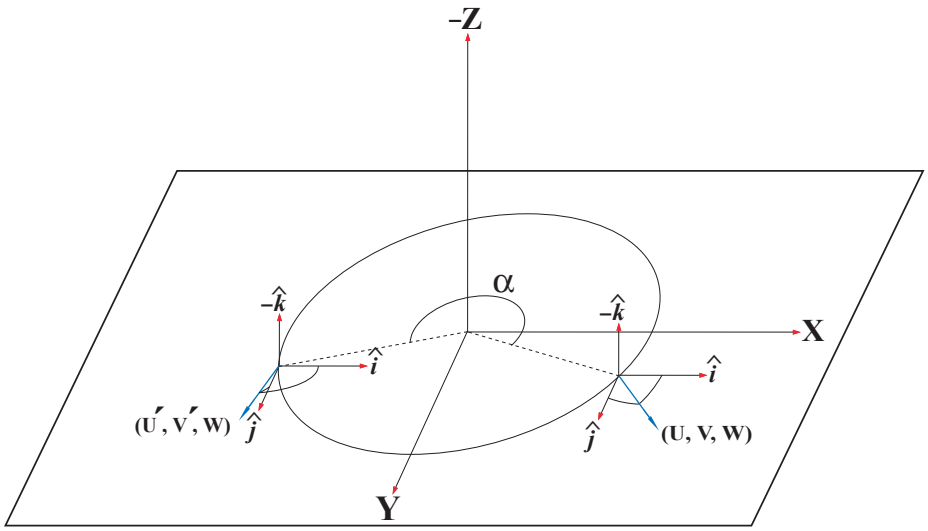

Figure 4.2: The MCTWIST rotation. A particle has entered the MCTWIST component module from the top (-Z) at radius R and undergoes a random azimuthal rotation α. Directional cosines are correspondingly transformed from (U, V) to (U', V'). The polar direction cosine (W) remains unchanged. Particle transport through the remainder of the simulation continues following the rotation.

The particle is then forced to undergo a random rotation about the central axis by generating a new random azimuthal angle ϕ' $(0 \leq \phi' < 2\pi)$. Therefore APR, as implemented in MCTWIST, is making use of cylindrical symmetry of the particle transport and effectively improves the accuracy of the particle fluence representation in the BEAM model that, as will be shown, results in reduced latent variance of the source. Particle direction cosines, U and V, are transformed to preserve the original directions relative to the central axis using the rotation matrix

$$\begin{pmatrix} U' \\ V' \end{pmatrix} = \begin{pmatrix} \cos(\alpha) & -\sin(\alpha) \\ \sin(\alpha) & \cos(\alpha) \end{pmatrix} \begin{pmatrix} U \\ V \end{pmatrix}, \tag{4.2}$$

where $\alpha = \phi' - \phi$.

Because of this random azimuthal rotation, it is required that the MCTWIST module be inserted into the accelerator model at a point downstream from the cylindrically symmetric accelerator head components. For the Clinac 21EX, the MCTWIST module was placed just below the patient independent PS_A located above the secondary collimating jaws (see Figure 4.1) where geometry is both cylindrically symmetric and patient independent. The monitor unit calculation method by Popescu *et al.* [Popescu et al., 2005] requires modeling transport of particles backscattered from the collimators back through the MCTWIST and MIRROR modules. Particles traveling backwards through the module will not be cylindrically symmetric and so these particles are not rotated. In the rare event that a backscattered particle traverses MCTWIST multiple times, multiple rotations will occur, however our estimates show that the contribution of these particles to the calculated dose is less than 0.1%.

There are several methods of implementing APR in MC simulations with the MCTWIST module while maintaining compatibility with the history-by-history method of uncertainty calculation. First, all particles of a given recycle iteration (NRCYCL) can be rotated the same random $\Delta\phi$. This is analogous to rotating the entire PS plane a random amount for each recycled use. Second (implemented as an option in MCTWIST), all sister particles associated with a particular primary (independent) history can be rotated the same random $\Delta\phi$. By rotating all sister particles by the same $\Delta\phi$ all correlations present between a primary history and all associated secondary histories are preserved. The final method of implementing APR with MCTWIST is to rotate every particle used from the PS a random ϕ whether they originated from the same primary or not. In this method the correlation of x-y directional cosines with other characteristics of all particles from a given primary history is reduced, but the correlation of remaining particle characteristics is maintained [Tyagi et al., 2006]. The correlated particle groupings are maintained by leaving the

assignment of negative energy to the first particle of each group. In this way no modifications are required to the history-by-history uncertainty calculation method. All results presented have used the last implementation of MCTWIST.

4.2.2 The Radial Dependence of Azimuthal Particle Redistribution

It is expected that the reduction in latent PS variance with MCTWIST is proportional to $1/R$, the radial distance from the beam's central axis. An explanation of this can be seen by first considering a small area element of PS_A, dA. Under the assumption of no electron scatter and perfect beam divergence, the latent variance σ_L^2 in the absorbed dose produced by this area element is proportional to $1/N$ where N is the number of particles in dA. From the definition of *latent variance* it is clear that SPR in dA will not effect σ_L^2. Relating N to $\rho(R)$, the density of particles in dA, one can write for the latent variance

$$\sigma^2_{L_{SPR}} \propto \frac{1}{\rho(R)dA}. \tag{4.3}$$

Using APR, the effective number of particles in dA is increased. This increase is proportional to the effective area of the PS contributing to the absorbed dose in the phantom and to the number of times each particle is to be recycled. The latent variance using MCTWIST, $\sigma^2_{L_{APR}}$, of dA is then

$$\sigma^2_{L_{APR}} \propto \frac{1}{\rho(R)2\pi RdR} \cdot F(NRCYCL), \tag{4.4}$$

where $F(NRCYCL)$ is a function of the number of times a particle is recycled. In Cartesian coordinates, used in DOSXYZnrc, the area dA is $(dR)^2$. Therefore reduction in latent variance, $\sigma^2_{L_{APR}}/\sigma^2_L$, is found to be inversely proportional to the radial distance from the beam's central axis and dependent on the number of particle recyclings:

$$\frac{\sigma^2_{L_{APR}}}{\sigma^2_L} \propto \frac{F(NRCYCL)}{R}. \tag{4.5}$$

Note that this inverse radial dependence of the *latent variance* reduction is the result of coordinate transformation between cylindrical (MCTWIST) and Cartesian (DOSXYZnrc) coordinate systems. Scoring the dose in a cylindrical coordinate system (such as in DOSRZ [Kawrakow and Rogers, 2000]) would yield radial-independent *latent variance* reduction that would only depend on NRCYCL. One can also see from Equations 4.3 to 4.5 that the radial fluence non-uniformity cancels in evaluation of $\sigma^2_{L_{APR}}/\sigma^2_L$.

To determine the additional simulation time required by the MCTWIST module, the percent time increase was calculated from the average time difference of 3 separate PS_A to PS_B BEAMnrc simulations, both with and without the MCTWIST module. Simulations were run on a single 2.8 GHz Pentium 4 processor using the BEAMnrcMP release with the g77 compiler with default BEAMnrc compiler options.

4.2.3 Evaluation of Latent Phase Space Variance Reduction with Azimuthal Particle Redistribution

The following MC transport parameters were used for all simulations: AP = PCUT = 0.010 MeV and AE = ECUT = 0.700 MeV, where AP and AE are the low-energy thresholds for the production of secondary Bremsstrahlung photons and knock-on electrons, while PCUT and ECUT define the global cutoff energy for photon and electron transport, respectively. Bremsstrahlung splitting was not applied.

The first goal in evaluating the effects of the APR was to determine the latent PS_A variance with and without the use of the MCTWIST module. This was accomplished using the method proposed by Sempau *et al.* [Sempau et al., 2001]. In this method the mean dose variance reported by DOSXYZnrc was determined using a deliberately limited fraction of PS_A containing 2×10^5 particles for a 10×10 cm^2, 6 MV beam

in a $30 \times 30 \times 30$ cm^2 water phantom. The dose was scored at a depth of 1.5 cm. By repeating the simulation for an increasing number of recyclings (NRCYCL = 1, 2, 10, 50, 100, 500, 1000) and extrapolating the variance to an infinite number of recyclings ($\frac{1}{NRCYCL} = 0$), the latent variance present in this fraction of PS_A is quantified. The latent variance of the full PS_A is smaller by a factor F_{size}, which is a ratio of the number of particles in the full PS_A to that from its limited fraction used in this evaluation process. Using this method the latent variance reduction in PS_A can be quantified, and its reduction due to APR can be determined. In addition, to allow confirmation of the radial dependence of the latent variance reduction, the mean dose variance was calculated in multiple annuli of 0.5 cm width, placed at radii R between the central axis and the field edge.

4.2.4 Dose Profile Calculations with Azimuthal Particle Redistribution

The effect that APR has on in-water dose profiles was determined by first establishing a set of benchmark MC profiles by which all other profiles obtained could be compared. This simulation was made using a large PS_A containing 2×10^8 particles (6.5 GB) recycled 100 times (for a total of 2×10^{10} particles simulated). This benchmark replicates the 10×10 cm^2 benchmark MC result obtained by Tyagi *et al.* for evaluation of their AKDE particle recycling alternative. For these and all other profiles shown, an (X,Y,Z) voxel size of 0.3 cm × 0.5 cm × 1.0 cm was used with the beam incident along the Z-axis. Profiles were taken along the X-axis at surface (first voxel), d_{max}, and at the depth of 10 cm. The latter profile is produced to provide a direct comparison with the results obtained using the AKDE method. Dose distributions with and without the MCTWIST module were obtained from simulations in which PS_A was recycled 100 and 1000 times. The total number of histories requested was kept at a constant 1×10^{10} particles. This was done to keep the particle transport component of the total dose variance (*i.e.* the non-latent PS variance contribution to the total dose variance) fixed for each simulation. In each of the simulations, the

dose was scored at d_{max} and at the surface of a $30 \times 30 \times 30$ cm^2 water phantom for a 10×10 cm^2 field with a 90 cm SSD.

To probe the range of possible PS_A file sizes used with MCTWIST while still obtaining acceptable agreement with the benchmark ($< 1.0\%$), the above method of obtaining profiles was repeated with increasing number of recyclings until an acceptance criteria of 1.0% was no longer met. An energy spectrum, cosine and radial position distributions for each of the PS_A was simultaneously calculated and examined within annuli of widths corresponding to the dose scoring voxel widths. It was expected that a positive correlation between the increasing uncertainty in our profiles and the increasing uncertainty in the distributions representing PS_A particle fluence would be seen. For each distribution, particles were selected in an annulus between $R = 2.7$ cm and $R = 3.0$ cm, for PSF containing 1×10^7, 1×10^6, and our benchmark 2×10^8 particles.

4.3 Results

4.3.1 Azimuthal Particle Redistribution

Figure 4.3 presents PS_B particle position scatter plots generated by BEAMDP using SPR (*top*) and APR (*bottom*) for 1.5×10^5 particles. In this simulation, particles from PS_A were recycled 100 times, transported through the collimating jaws, and recorded in PS_B. The upper scatter plot appears to have fewer particles simply because many of the particles are overlapping due to the lack of significant scattering. This figure demonstrates the origin of latent variance in the PSF and improvement in the particle source representation using MCTWIST.

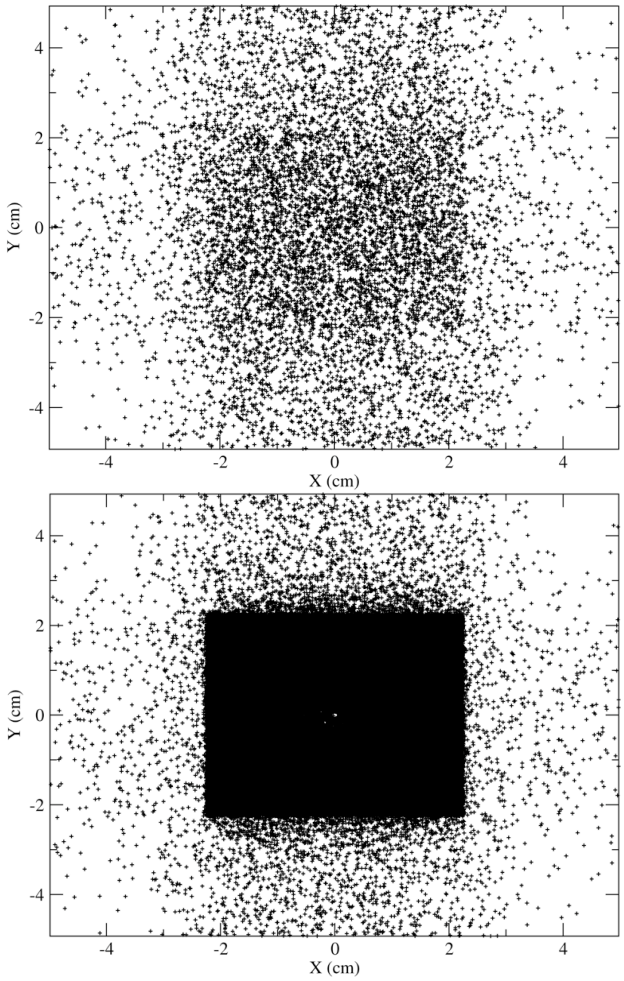

Figure 4.3: PS_B particle position plot generated by BEAMDP at Z=45.0 cm from the electron target using standard particle recycling (*top*) and using advanced particle recycling with the MCTWIST component module (*bottom*). Both plots contain the same number of particles (1.5×10^5). Both PS_B's were obtained by simulating particles from the same PS_A, recycled 100 times, through the secondary collimating jaws. The plot on the top only appears to have fewer particles because of overlapping particle positions.

The increase in simulation time using the MCTWIST module was determined to be an additional 15% for transporting particles between PS_A and PS_B. Given that the simulation through the secondary collimator is a small component of the entire patient dose calculation, the MCTWIST computational overhead can be considered insignificant.

4.3.2 Evaluation of Latent Phase Space Variance with Azimuthal Particle Redistribution

Figure 4.4 presents the determination of latent variance reduction in PS_A for both SPR and APR. From this figure, it can be seen that the latent PS variance is reduced by a factor of 2 near the central axis and by more than a factor of 35 off axis, when using the MCTWIST module. Marked improvement appears at 10 recyclings with a total variance reduction of 18%. The latent relative standard deviation for the 200 000 particle PSF is determined to be 3.2%. Note that the above variance is reported for dose scored in a plane between 1 cm and 2 cm depth. The latent variance for a single voxel was estimated using the method by Sempau *et al.* [Sempau et al., 2001] and found to be significantly larger. The latent variance for the 0.3 cm $\times$ 0.3 cm $\times$ 1.0 cm voxel used in this simulation was determined to be 6.34% $\pm$ 0.55%. The magnitude of the latent variance for 200 000 particles can be scaled to estimate that of the full phase space by applying the factor F_{size} described in Section 4.2.3. Table 4.1 presents the latent variance for this voxel size after scaling to larger PS_A file sizes.

# Particles	Est. σ^2_{Latent}	Uncertainty
2×10^8	0.32 %	$\pm$ 0.02 %
1×10^8	0.45 %	$\pm$ 0.03 %
1×10^7	1.43 %	$\pm$ 0.09 %
1×10^6	4.52 %	$\pm$ 0.29 %

Table 4.1: Estimated latent PS variance for a 0.3 cm $\times$ 0.3 cm $\times$ 1.0 cm voxel for various PS_A file sizes.

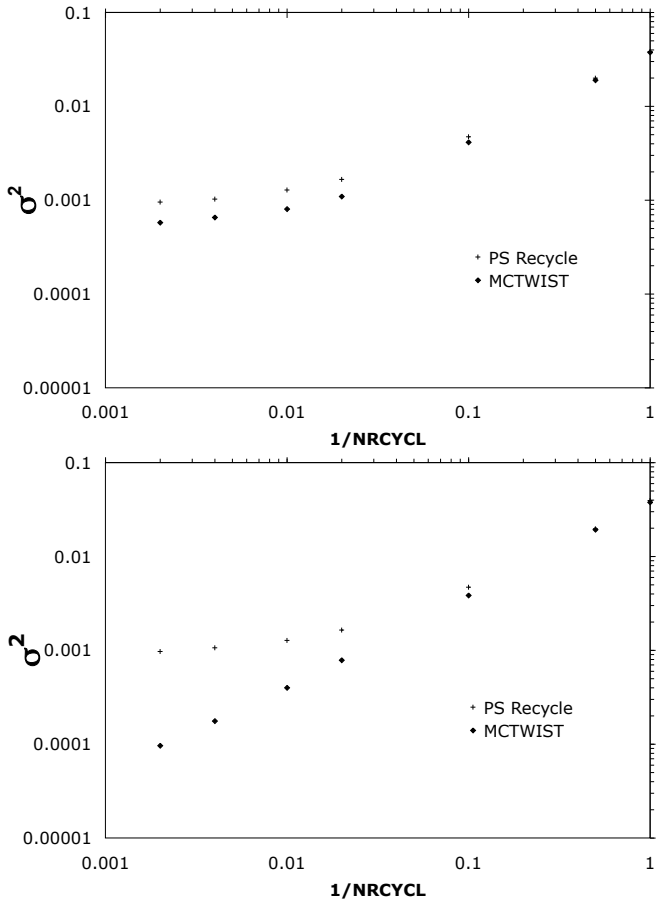

Figure 4.4: Plot showing the reduction in variance (relative) of the dose produced by a 10×10 cm^2, 6 MV beam in a $30 \times 30 \times 30$ cm^2 water phantom at 1.5 cm depth both on the beam's central axis (*top*) and 4.0 cm off-axis (*bottom*). MC variances for PS recycling factors (NRCYCL) of 1, 2, 10, 50, 100, and 500 have been displayed for both SPR and APR (MCTWIST). For each data point 200 000 particles were drawn from PS_A and recycled by the respective amounts.

Shown in Figure 4.5 is a plot of the fractional reduction in variance (σ^2) reported by DOSXYZnrc for the 10×10 cm^2 field vs 1/R, the radius from the central axis, for 200 000 particles modeled with various number of recyclings (NRCYCL). This plot confirms that, for a given number of recyclings, the fractional improvement in variance is proportional to 1/R.

4.3.3 Dose Profile Calculations with Azimuthal Particle Redistribution

Figure 4.6 presents benchmark 6MV, 10×10 cm^2 profiles generated as described in Section 4.2.4. Even though a large number of particles were used, a significant

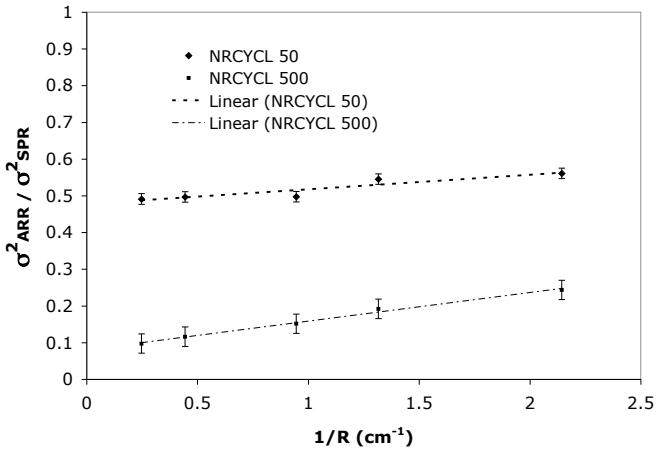

Figure 4.5: Plot showing the inverse radial dependence of the fractional reduction in standard deviation using MCTWIST for NRCYCL = 50, 500, for a 6 MV beam in a $30 \times 30 \times 30$ cm^2 water phantom at a depth of 1.5 cm.

amount of dose uncertainty is still observed in the SPR benchmark profile. The dose profiles produced using MCTWIST CM (labeled as MCTWIST benchmark) while being considerably smoother closely follow the shape of the SPR benchmark profiles. The MCTWIST benchmark dose profile uncertainty (also shown in Figure 4.6) is reduced as compared to the SPR benchmark.

To this point it has been shown (Figures 4-6) that APR reduces latent variance, reproduces the shape of the SPR dose profile and provides less dose uncertainty. The MCTWIST profiles are therefore used as a benchmark to compare all following profiles in this chapter.

Figure 4.7 shows the resulting dose profiles scored at d_{max} for simulations using 1×10^8 histories recycled 100 times. For the profile on the right, APR has been used. In this Figure, the use of APR has produced a much smoother profile, closer to the benchmark of 2×10^{10} total histories, with lower overall uncertainty as reported by DOSXYZnrc (see difference plots below each profile).

In Figure 4.8, dose profiles at surface from simulating 10^8 particles recycled 100 times are presented. Once again, for the profile on the right, APR has been used. Because relatively few particle scattering events occur prior to entering the phantom,

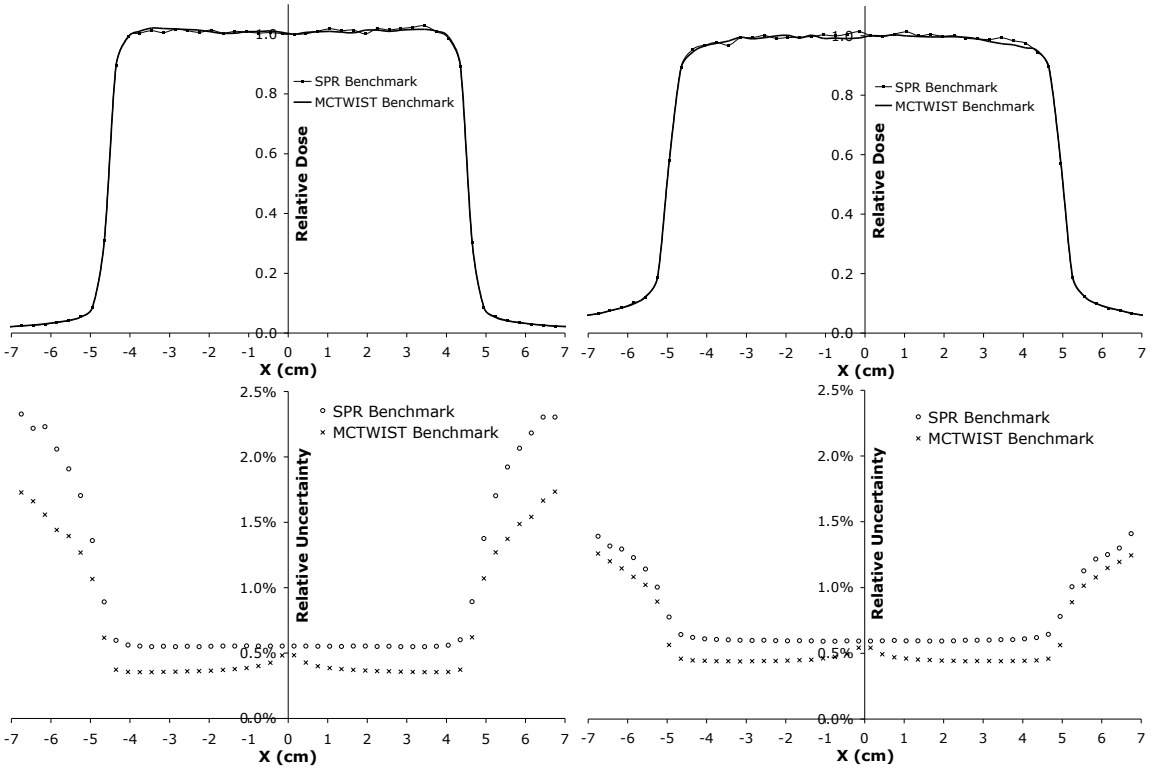

Figure 4.6: 6 MV, 10×10 cm^2 field benchmark dose profiles and corresponding uncertainties scored in a $30 \times 30 \times 30$ cm^2 water phantom at a depth of 1.5 cm (*left*) and 10.0 cm (*right*) with an SSD of 90.0 cm. Both SPR and APR benchmark simulations were made with 2×10^8 histories recycled 100 times.

it was expected that the contribution of latent variance to the overall variance would be greatest at the surface. This is confirmed by comparing profiles at the surface (Figure 4.8) with those at d_{max} (Figure 4.7).

Figures 4.9 and 4.10 show profiles at d_{max} and at surface respectively from the simulations in which each particle was recycled 1000 times.

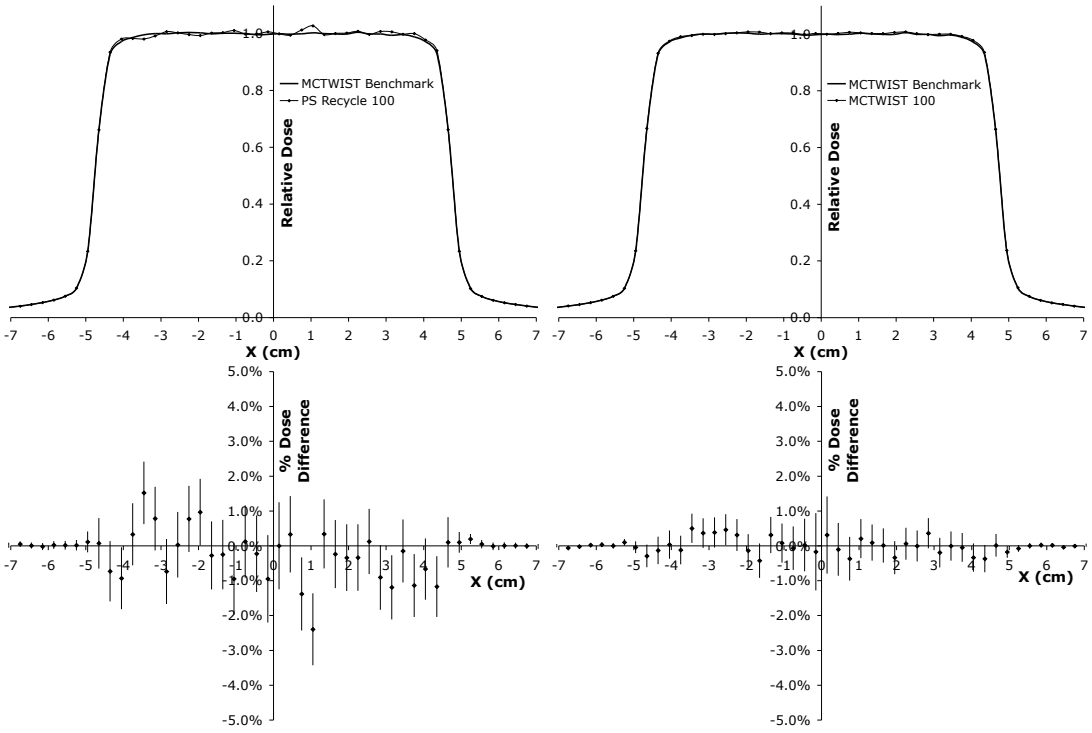

Figure 4.7: 6 MV, $10\times10\text{cm}^2$ field profiles (and accompanying dose difference plots) scored in a $30 \times 30 \times 30$ cm^2 water phantom at a depth of 1.5 cm (d_{max}) from the simulation of 1×10^8 histories from PS_A, recycled 100 times (1×10^{10} total).

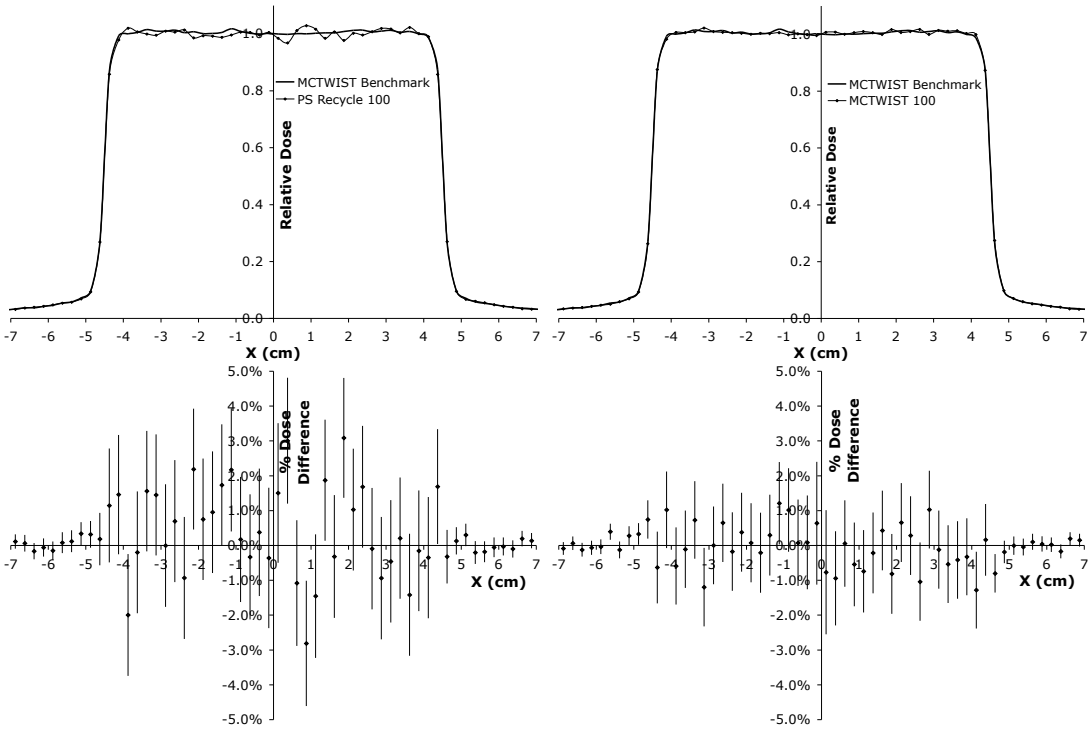

Figure 4.8: 6 MV, $10 \times 10\text{cm}^2$ field profiles scored in a $30 \times 30 \times 30$ cm^2 water phantom at the surface. Both figures show the agreement with the benchmark after simulating 1×10^8 histories from PS_A, recycled 100 times (1×10^{10} total).

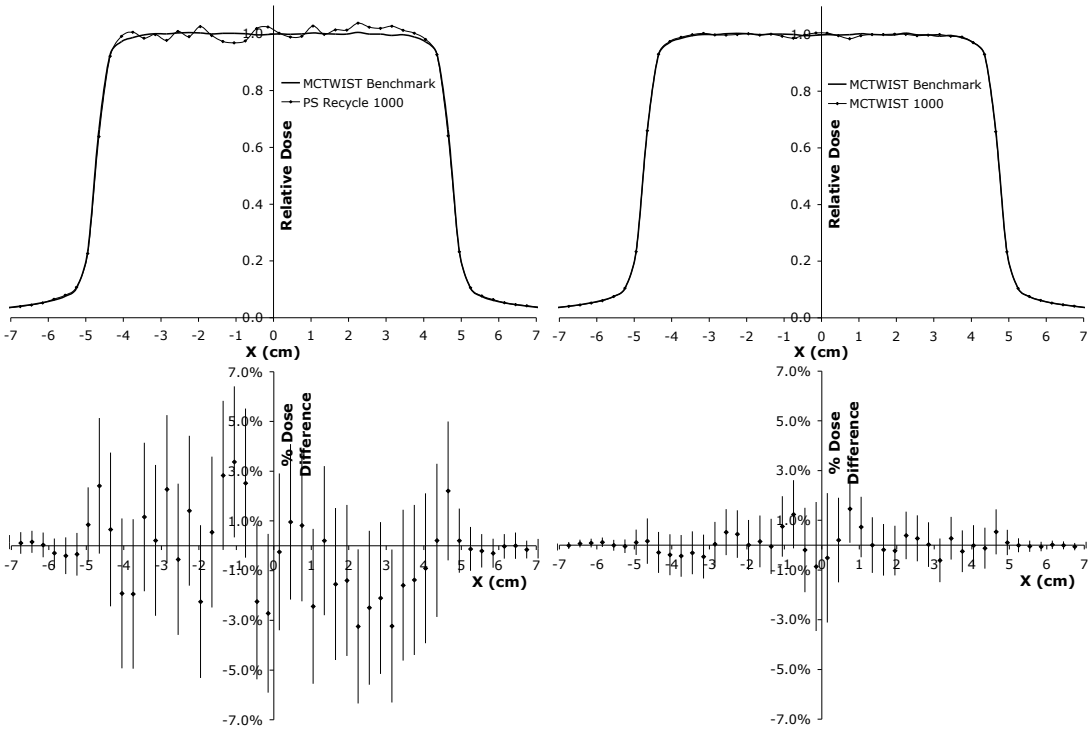

Figure 4.9: 6 MV, $10 \times 10\text{cm}^2$ field profiles scored in a $30 \times 30 \times 30$ cm^2 water phantom at a depth of 1.5 cm with an SSD of 90.0 cm, resulting from the simulation of 1×10^7 histories from PS_A, recycled 1000 times (1×10^{10} total).

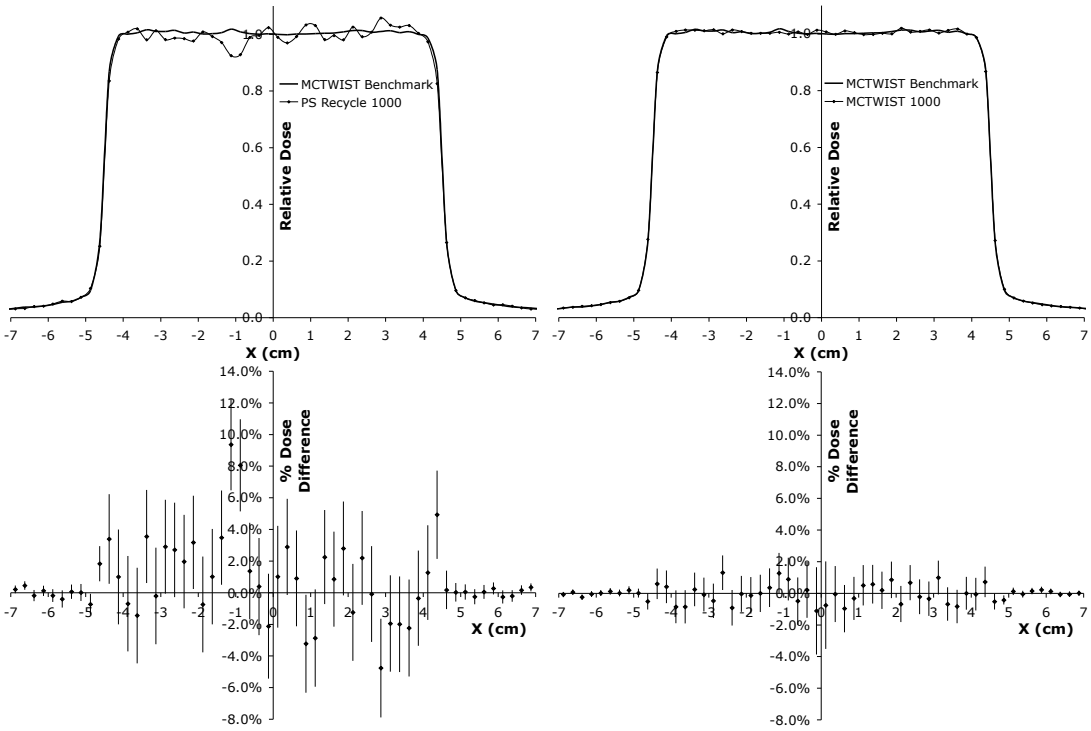

Figure 4.10: 6 MV, $10 \times 10\text{cm}^2$ field profiles scored in a $30 \times 30 \times 30$ cm^2 water phantom at the surface with an SSD of 90.0 cm, resulting from the simulation of 1×10^7 histories from PS_A recycled 1000 times (1×10^{10} total).

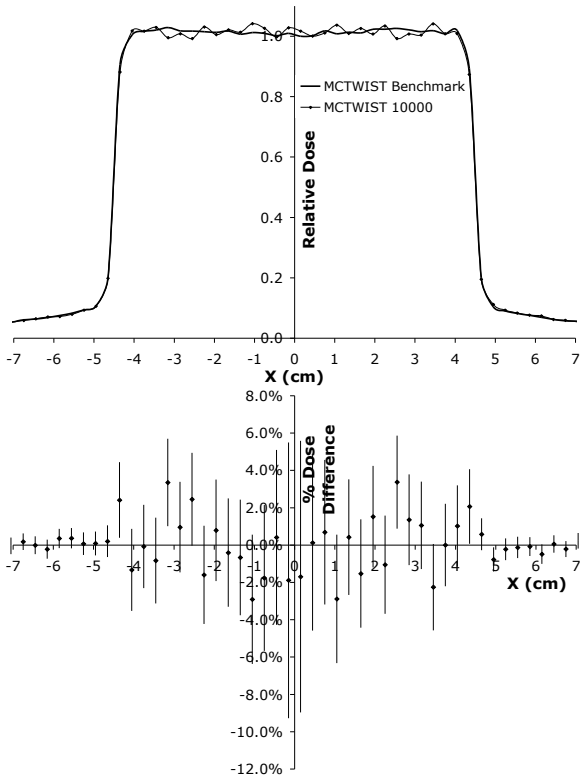

Figure 4.11: 6 MV, $10 \times 10\text{cm}^2$ field profiles and accompanying uncertainties scored in a $30 \times 30 \times 30$ cm^2 water phantom at surface with an SSD of 90.0 cm from the simulation of 1×10^6 histories from PS_A recycled 10 000 times (1×10^{10} total), with the MCTWIST module.

In all cases considered up to 1000 recyclings, the MCTWIST profiles remain in good agreement with benchmark while the SPR technique breaks down as expected at surface with a high number of recyclings, producing inaccurate profiles. The radial dependence on APR variance reduction is observed in the percent dose difference plots of these figures.

Figure 4.11 shows the MCTWIST profile at surface from a simulation in which each particle was recycled 10 000 times (1×10^6 particles in the phase space). With this few original phase space histories used the MCTWIST profile shows significant uncertainty due to a large latent variance component in the overall variance.

In Figure 4.12, the mean percent absolute dose difference of APR profiles with the benchmark profile has been calculated and plotted against the number of original

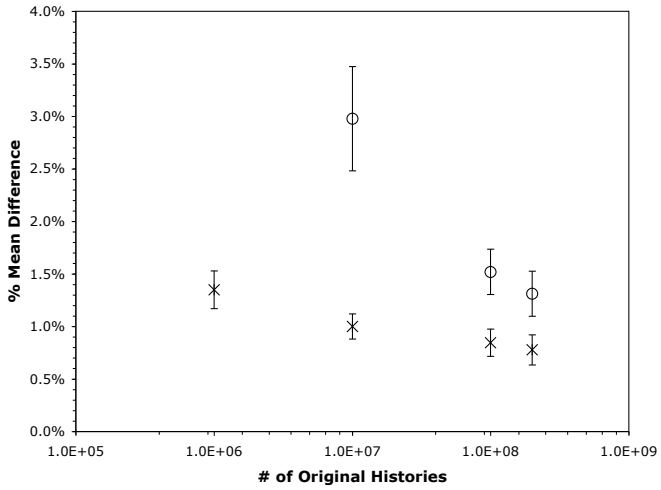

Figure 4.12: Plot showing the percent mean difference vs. number of original histories used from PS_A for the surface profiles presented above. For each data point the total number of histories simulated (after recycling) was a constant 1×10^{10} histories. The circular data points correspond to the SPR percent mean differences while the X data points correspond to the APR percent mean differences.

histories used from PS_A for recycling factors of 50, 100, 1000, and 10 000. Also plotted are the mean absolute percent dose differences between the benchmark profile and SPR simulations for 50, 100 and 1000 recyclings. From this figure, it can be seen that the mean absolute percent dose difference from a MC simulation using 10^7 PS_A particles with a recycling factor of 1000 provided better agreement with the benchmark (1.0%) than an SPR simulation using 20 times more particles (1.3%). This is also close to the value of mean percent absolute dose difference calculated from a very small (10^6 particles, which is 200 times less than the phase space used in SPR) phase space recycled with MCTWIST 10000 times.

Figure 4.13 shows MCTWIST and SPR dose profiles for 3×3 cm^2 (*top*) and 30×30 cm^2 (*bottom*) fields. The 3×3 cm^2 field is the result of 1×10^8 histories from PS_A recycled 100 times (1×10^{10} total) while the 30×30 cm^2 field was limited to only 1×10^7 histories from PS_A recycled 100 times due to phase space size restraints. Voxel sizes of 0.3 and 0.6 cm were used along the 3×3 cm^2 and 30×30 cm^2 profile directions. The results confirm the effectiveness of APR with varying field size.

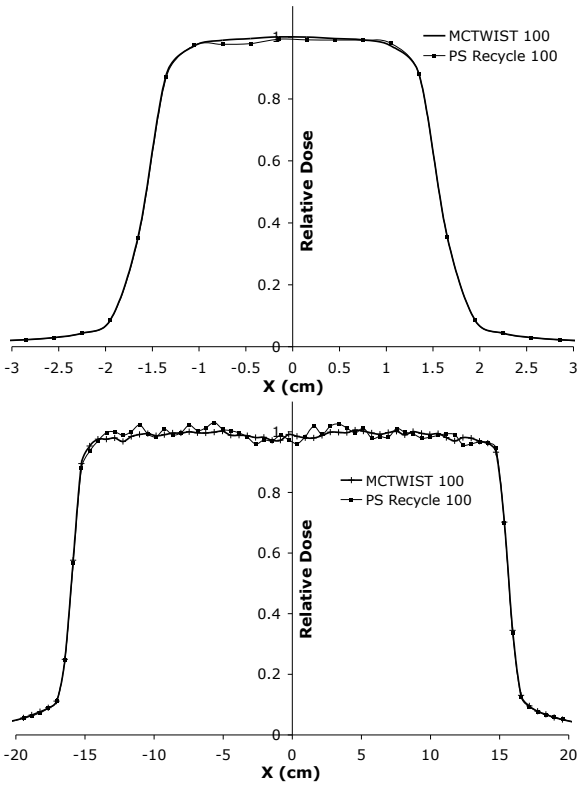

Figure 4.13: 6 MV, $3 \times 3\text{cm}^2$ (*top*) and $30 \times 30\text{cm}^2$ (*bottom*) field profiles scored in a $30 \times 30 \times 30$ cm^2 water phantom at 1.5 cm depth with an SSD of 90.0 cm from the simulation of 1×10^8 histories from PS_A recycled 100 times (1×10^{10} total) and 1×10^7 histories from PS_A recycled 100 times respectively, with SPR and with the MCTWIST module.

In Figure 4.14 the 10×10 cm^2 MCTWIST and benchmark profiles at 10 cm depth are presented for direct comparison with AKDE results.

To investigate the degradation in profile dose uncertainty with increasing particle recyclings, the spectral distribution of the particle fluence and radial position distribution have been plotted for each PS_A used in the above 10×10 cm^2 profiles. (See Figures 4.15 and 4.16.) For each figure, the 1×10^6 particle histogram corresponds to the 10 000 recycle simulation.

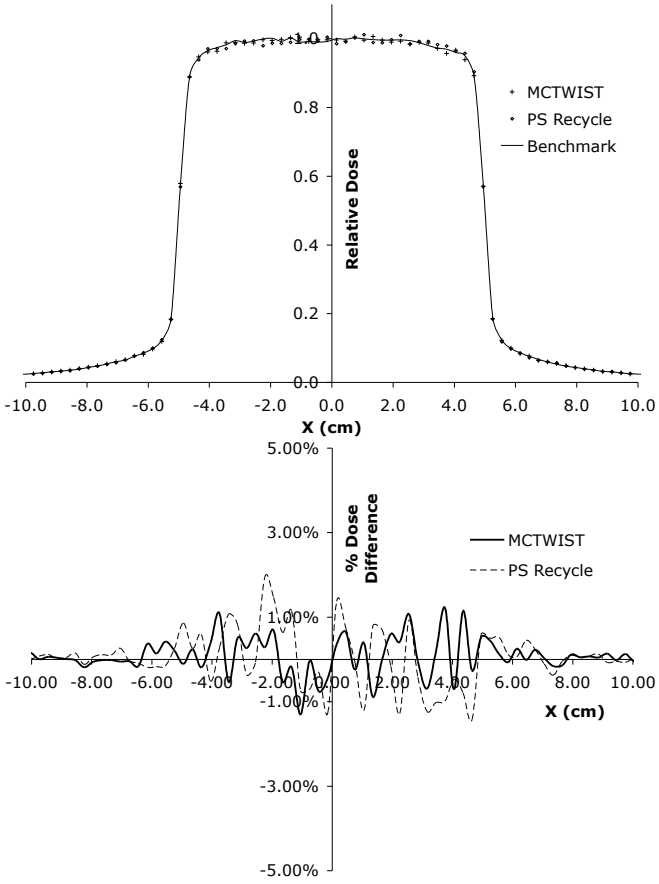

Figure 4.14: 6 MV, $10 \times 10\text{cm}^2$ field profiles scored in a $30 \times 30 \times 30$ cm^2 water phantom at 10 cm depth with an SSD of 90.0 cm from the simulation of 1×10^8 histories from PS_A recycled 100 times (1×10^{10} total), with SPR and with the MCTWIST module.

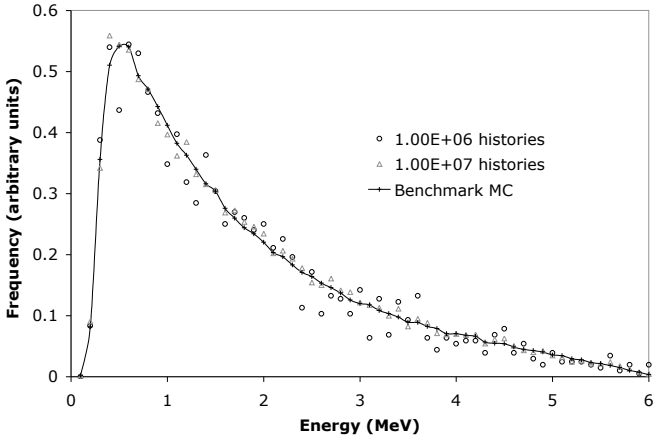

Figure 4.15: Plot showing the spectral distribution of the particle fluence within an annulus between radii 2.7 cm and 3.0 cm for three PS_A's containing: 1×10^6, 1×10^7, 2×10^8 (benchmark) histories.

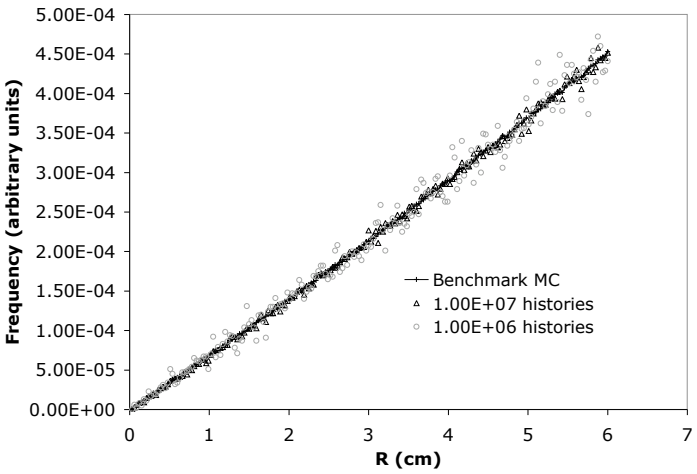

Figure 4.16: Plot showing the radial position distribution for three PS_A's containing: 1×10^6, 1×10^7, 2×10^8 (benchmark) histories.

4.4 Discussion and Conclusions

By making use of cylindrical phase space (PS) symmetry and sampling new azimuthal particle positions between recyclings, the MCTWIST module provides a simple mechanism by which latent phase space variance and consequently the variance of scored dose can be reduced, especially near the surface of a phantom. Unlike post-simulation smoothing techniques, which operate on calculated dose distributions, APR improves accuracy of the particle source prior to radiation transport into the phantom. The potential for inadvertently smoothing out naturally occurring high dose gradient regions within the phantom does not exist as it does with post-process smoothing techniques.

Ultimately, to avoid latent PS variance completely, MC PSF's would be of sizes great enough to not require the recycling of particles or would not be used at all. However, even with modern computers, a two-step PS approach using particle recycling is the best feasible alternative.

To improve results in the clinical realm when using a two-step PS based MC simulation with particle recycling, significant reductions in latent PS variance have been achieved using MCTWIST with as little as 10 particle recyclings. A mean surface profile agreement of 1.0% has been achieved with a PS_A containing as little as 10 million histories, recycled 1000 times.

Comparing the results of implementing MCTWIST (Figure 4.14) with the results obtained by AKDE, one can see that APR has yielded a profile of similar quality to the AKDE method within the high dose region (within 1.2% uncertainty for both) and performs substantially better in the penumbral region (1.2% for APR versus 4.50% for AKDE)(for a comparison refer to Tyagi *et al.* [Tyagi et al., 2006] Figure 5(b)). As no latent variance reduction was reported or concluded by Tyagi *et al.*, no comparison can be made in this respect. Tyagi *et al.* have also found that their SPR profiles show a systematic bias with high recyclings. No systematic bias has appeared

in the author's SPR profiles, as seen in Figure 4.14. From the author's profiles, the greatest latent variance appears closer to the surface of the phantom and is nearly washed out by 10 cm depth.

As expected, the variance reduction capabilities of APR are increased radially from the beam's central axis. The reduction in the absorbed dose variance for a given number of particle recyclings was found to be proportional to $1/R$ when the absorbed dose is scored in a DOSXYZnrc cartesian voxel set.

It is important to note that the use of bremssrahlung splitting is not a replacement for particle redistribution in any way and the two techniques are entirely compatible. Latent variance reduction by particle redistribution is a technique to reduce PSF latent variance for a phase space of a fixed size. Bremsstrahlung splitting will simply reduce the latent variance of the PSF per incident electron, not per PSF size.

Uncertainty in the spectra for all particle characteristics will contribute to the dose profile uncertainty. By considering the phase space in cylindrical coordinates (R, ϕ, w, E), the characteristics that do not undergo variance reduction with azimuthal recycling include R, w (*i.e.* $\cos(\theta_Z)$), and E. Therefore, if these characteristics become inaccurate due to statistical fluctuations, it will be reflected in the inaccurate dose profiles. From the plotted energy spectra and radial position distribution (Figures 4.15 and 4.16), an increasing level of degradation was observed as the size of PS_A decreases. The $\cos(\theta_Z)$ distribution (not shown) was found to be less sensitive to PS_A size. One can see from these figures, that as PS_A gets smaller, it becomes a poor representation of the particle fluence that results in inaccurate dose profiles. Therefore evaluation of energy spectra and radial distribution of particles in the phase space allows establishing a lower limit on the size of the phase space that can be used with APR for accurate MC calculations.

In some respects, APR is similar to the particle re-distribution technique offered in DOZXYZnrc code through utilizing the ISMOOTH input parameter. However, as

demonstrated, APR as implemented in MCTWIST, is a considerably more powerful and flexible technique. MCTWIST provides a significant improvement in latent variance reduction over re-distribution with ISMOOTH. The number of effective recycles is only four with ISMOOTH, whereas it can be thousands with MCTWIST, and is only limited by the size of the phase space. Clearly, the dose fluctuations that appeared in the profiles, produced by 10 000 recyclings with MCTWIST, are attributed to a small size of the phase space (only 1 000 000 particles) rather than to a large number of recyclings. Larger phase spaces, that maintain integrity of the particle spectra, can potentially be re-cycled as many times as needed. Another important difference, is that re-distribution with ISMOOTH is limited to radiation fields that are symmetric relative to central axis of the beam. This is a rather severe limitation making re-distribution with ISMOOTH unusable in clinical MC treatment planning calculations. In contrast, MCTWIST, being a component module positioned above any moving parts of the linac treatment head, can be used for any field, including intensity modulated fields.

MCTWIST has been written in the format of a BEAMnrc component module to allow for easy implementation in any accelerator model that has cylindrical symmetry for particles traveling *downstream*.

Chapter 5

Monte Carlo Modeling of Arc Radiotherapy Delivery

Based on Bush *et al.*, Phys. Med. Biol. **53**, 19 (2008)

In the preceding chapters, the Monte Carlo method was introduced and two techniques addressing fundamental issues faced by Monte Carlo users were investigated. In this chapter a framework will be developed to carry out Monte Carlo dose calculations with BEAMnrc for the dosimetric verification of Varian's RapidArc delivery system. Verification of the framework will be made through comparison of the calculation results with the Eclipse treatment planning system (Varian Medical Systems, Palo Alta, CA). The approach represents the first published account of Monte Carlo dose modeling of RapidArc treatments.

5.1 Introduction

The RapidArc delivery system is among the most complex radiotherapy treatment modalities available today, able to deliver an entire treatment fraction in a single volumetric modulated arc [Otto, 2008]. The clinical impact and effectiveness of volumetric modulated arc therapies (VMAT) has been investigated [Clivio et al., 2009; Cozzi et al., 2008; Fogliata et al., 2008, 2009; Johansen et al., 2009; Kjaer-Kristoffersen et al., 2009; Palma et al., 2008]. Verification of RapidArc dose calculation will certainly be an active part of upcoming research in the medical physics community.

The unmatched ability of Monte Carlo (MC) methods to model intensity-modulated radiation therapy (IMRT) delivery is well recognized, as is the ability of MC methods to accurately model small radiation field apertures present in RapidArc radiation delivery. MC based verification methods have been implemented in previous radiotherapy arc delivery techniques. Solberg *et al.* [Solberg et al., 1998] used Monte Carlo dose calculations to investigate effects of tissue inhomogeneities in radiosurgery plans produced with fixed circular collimators. Li *et al.* [Li et al., 2001] demonstrated the feasibility of Monte Carlo modeling an intensity-modulated arc therapy (IMAT) technique [Yu, 1995]. The technique approximated the modulated arc as a series of static multi-leaf collimator (MLC) apertures with a gantry angle spacing of 10 de-

grees. Chow *et al.* [Chow et al., 2003] explored the use of MC particle source model techniques in open field photon arcs. The technique uniformly sampled gantry positions for the open field (non-MLC) arc during the MC simulation. Gladwish *et al.* [Gladwish et al., 2007] developed efficiency improvements to the IMAT optimization process resulting in fewer required MLC leaf pair position permutations. MC dose calculation was used on 51 static field MLC segments from the final derived IMAT optimization using a fast commercial MC dose calculation code (NXEGS). MC verifications of Tomotherapy delivery [Mackie et al., 1993] have also recently been recently published [Muzik et al., 2008; Sterpin et al., 2008].

The importance of treatment plan dose verification in arc radiotherapy has been discussed by Li *et al.* [Li et al., 2001] with respect to IMAT delivery. RapidArc radiation fields are of increased complexity, in comparison with the characteristic IMAT dynamic gantry and MLC motions, in that small field apertures are commonly found in RapidArc plans as well as a variable dose rate during delivery. In this situation Monte Carlo verification of RapidArc dose calculation, calculated using the anisotropic analytical algorithm (AAA), becomes indispensable.

In this chapter, an efficient framework (VIMC-Arc) for MC verification of RapidArc treatment plans is developed and presented. The implementation is unique in that dynamic MLC motion is explicitly modeled throughout the arc rotation. VIMC-Arc requires only a standard RapidArc Digital Imaging and Communications in Medicine (DICOM) dataset to construct the MC beam and patient models, simulate radiation transport and collect the resulting dose, which is returned in DICOM format for import back into the treatment planning system (TPS). A comparative dosimetric investigation of RapidArc's AAA dose calculations against Monte Carlo calculations with VIMC-Arc was conducted and published in a study by Gagne *et al.* [Gagne et al., 2008] using the system developed in this chapter.

5.2 Materials and Methods

5.2.1 The Vancouver Island Monte Carlo (VIMC) system

VIMC-Arc is based on the VIMC process [Zavgorodni et al., 2007, 2008] developed as a collaborative project within the BC Cancer Agency - Vancouver Island Center. The author has made considerable contributions to the project including developing the primary infrastructure of the software, coding many of the C++ library routines, TCL and shell scripting, interfacing with the parallel computing batching system [Thain et al., 2005], and co-supervision of cooperative education students working on code for the system. This section briefly describes the VIMC system components that are relevant to the implementation of VIMC-Arc. Specific attention will be placed on the author's contributions.

VIMC was built for verification of existing treatment plans that can be exported from the planning system in DICOM standard format. The MC plan verification process is illustrated in Figure 5.2. The DICOM exported data set is required to include the patient's computed tomography (CT) files, a plan file containing all planning parameters (including linac/couch angles, monitor unit details, MLC leaf sequences, etc.), and dose files containing the dose distribution within the patient, calculated by the TPS. Plan parameters needed for the MC simulation of the linac head, as well as patient CT data, are extracted from the DICOM dataset using an in-house developed DICOM Library [Locke and Zavgorodni, 2008]. The linac head is modeled using the BEAMnrc system [Rogers et al., 1995]. Azimuthal particle redistribution [Bush et al., 2007] (see Chapter 4) is incorporated in the BEAMnrc model, considerably reducing the latent variance [Sempau et al., 2001] in the calculated MC dose distributions. Photon transport through the MLC for conformal and IMRT fields is modeled using the particle DMLC code [Keall et al., 2001; Siebers et al., 2002].

A patient phantom is created from the (CT) dataset, using the CTCreate code

contained in the DOSXYZnrc package [Walters et al., 2005]. Once the patient phantom is generated, the dose distributions can be calculated with either the DOSXYZnrc [Walters et al., 2005] or VMC++ code [Kawrakow et al., 1996]. The patient phantom can be converted into binary format for compatibility with VMC++.

Co-ordinate transformations [Thebaut and Zavgorodni, 2006] were implemented into VIMC to provide the relationship between the linac's coordinates (the isocentre position within a patient, along with the gantry, collimator, and couch angles) and the DOSXYZnrc coordinate system. This is essential as multiple coordinate systems are used by different codes. The patient phantom is generated by CTCreate from the DICOM CT dataset, and the phantom therefore remains in the DICOM co-ordinate system (c.s.). BEAMnrc models the treatment beams in a Cartesian c.s. with a different orientation to that of the patient c.s. The incident beam direction and orientation in DOSXYZnrc are required to be specified in spherical coordinates that, in turn, must be calculated from gantry, couch, and collimator angles provided by the planning system. The equivalent transformations for use with VMC++ have also been derived by the author and are presented in the following section for reference.

The total number of particle histories required for modeling each treatment field is calculated based on the user's requested dose uncertainty [Spezi et al., 2002]. This calculation is based on the secondary collimator size, the voxel dimensions in the patient phantom and effective attenuation coefficient of the photon beam. When a plan consists of multiple beams, the uncertainty for each beam is added in quadrature. The calculation of the required number of particles (N) to be run per field (from a phase space located above the jaws) is calculated as

$$N = \frac{1}{n}\frac{1}{\xi\delta^2\mu_{\text{en}}^{\text{eff}}}\frac{A_{\text{beam}}}{V_{\text{voxel}}}, \tag{5.1}$$

where n is the number of fields, δ is the total requested uncertainty, $\mu_{\text{en}}^{\text{eff}}$ is the effective energy absorption coefficient in water for the given field's photon energy, A_{beam} is the

open area of the beam, V_{voxel} is the volume of the voxels used to create the patient phantom, and ξ is a correction factor to account for the scattered dose contributions and other deviations from the ideal case assumed in Equation 5.1. The correction factor ξ was derived from a 10×10 cm^2 calibration run.

For a plan with multiple fields, BEAMnrc and DOSXYZnrc (or optionally VMC++) input files as well as script files that run the simulation are created by VIMC for each field. These job scripts are submitted to the Vancouver Island Monte Carlo (VIMC) computing cluster (24-node cluster) via the Condor High-Throughput Computing software[1] to allow parallel execution of fields. Upon execution, each field simulation produces a separate 3D dose distribution.

The 3D dose output files produced from VMC++ are produced in a binary format and so are converted to conform to the 3D dose format of DOSXYZnrc using the .3ddose C++ library written by the author. This enables VIMC to seamlessly use the same process to handle the 3D dose output from either DOSXYZnrc or VMC++.

Conversion to absorbed dose from the normalized units of Gy/incident electron (as produced by DOSXYZnrc and VMC++) to the absolute dose in Gy for each treatment field is achieved using the strategy of Popescu *et al.* [Popescu et al., 2005]. In this method, backscattered radiation from the secondary collimator is collected in the monitor chamber for use in the calculation. This method has been shown to be very versatile, allowing simple yet very accurate absolute dose calculations in a variety of situations encountered in treatment planning, from symmetric and asymmetric open fields to static and sliding window IMRT. Following the conversion into absolute dose (Gy) of the entire set of field dose distributions, all fields are summed to provide a total plan dose.

Since the Eclipse TPS (and most other TPS's) calculate the absorbed dose as *dose-to-water*, VIMC has an option of converting the *dose-to-media* (D_{med}) resulting from

[1]Condor Project, Madison, Wisconsin.

DOSXYZnrc calculated distributions to dose-to-water (D_w) for accurate comparison. This is done using the method of stopping power ratios proposed by Siebers *et al.* [Siebers et al., 2000]. Using this method each voxel's dose is converted from *dose-to-media* to *dose-to-water* by first determining the media of the voxel from the patient phantom. Using a look-up table of mass collisional stopping power ratios the dose is converted as

$$D_w = D_{\text{med}} s_{w,\text{med}}, \tag{5.2}$$

where $s_{w,\text{med}}$ is defined as *the ratio of unrestricted mass collisional stopping power in water to mass collisional stopping power in the medium averaged over the energy spectra of primary electrons in the phantom.* The converted dose distribution and individual field dose distributions are then written in DICOM format, to be available for import into a TPS such as Varian's Eclipse along with the *dose-to-media* dose distributions.

Although VIMC uses a BEAMnrc model for the Varian Clinac 21EX, the VIMC process is designed for use with many other clinical accelerators, and is not limited to the Varian 21EX.

IEC coordinate transformations for clinical phase-space based VMC++ simulation

The use of VMC++ dose calculation into the VIMC system required the derivation of a coordinate transformation to allow the particles of a BEAMnrc type phase-space file (PSF) to be correctly oriented relative to the VMC++ patient model using Euler angles (α, β, γ), translation vector x_o and isocenter position x_{iso} from International Electrotechnical Commission (IEC) linac coordinates of gantry, collimator and couch angles.

The position x and direction u of each particle in the PSF are translated and rotated within the VMC++ to new position x' and direction u' by way of the following

operations:

$$x' = R(x + x_o - x_{iso}) + x_{iso} \tag{5.3}$$

and

$$u' = R(u), \tag{5.4}$$

where rotation operator R is defined to be

$$R = R_x(\alpha)R_y(\beta)R_z(\gamma) \tag{5.5}$$

with rotation matrices

$$R_x(\alpha) = \begin{bmatrix} 1 & 0 & 0 \\ 0 & \cos(\alpha) & -\sin(\alpha) \\ 0 & \sin(\alpha) & \cos(\alpha) \end{bmatrix}, \tag{5.6}$$

$$R_y(\beta) = \begin{bmatrix} \cos(\beta) & 0 & \sin(\beta) \\ 0 & 1 & 0 \\ -\sin(\beta) & 0 & \cos(\beta) \end{bmatrix}, \quad \text{and} \tag{5.7}$$

$$R_z(\gamma) = \begin{bmatrix} \cos(\gamma) & -\sin(\gamma) & 0 \\ \sin(\gamma) & \cos(\gamma) & 0 \\ 0 & 0 & 1 \end{bmatrix}. \tag{5.8}$$

The motion of the Clinac 21EX can be expressed in terms of the rotation matrices R_x, R_y, R_z about the right handed patient coordinate system (c.s.) of the Eclipse TPS. In the patient c.s. the positive X-axis is directed laterally left, the positive Y-axis is directed posterior, and the positive Z-axis is directed superior. The radiation field of an accelerator with gantry, couch and collimator (*col*) angles all equal to zero *(top-dead-zero)* is incident on the front of the patient with head pointing toward the

gantry.

Using rotation matrices in the patient c.s., a collimator rotation is simply described by a rotation about the −Y-axis or $R_{-y}(col)$. A gantry rotation is then simply described by a rotation about the +Z-axis or $R_z(gantry)$ and a couch rotation is then described by a rotation again about the −Y-axis or $R_{-y}(couch)$. The non-commutative nature of the operations requires the rotations be applied in the order: collimator, gantry, couch. The rotation of the linear accelerator (R_{accel}) is then described in terms of rotation matrices as

$$R_{accel} = R_{-y}(couch)R_{-z}(gantry)R_{-y}(col). \tag{5.9}$$

To determine the position of the linear accelerator beam in terms of the VMC++ rotations about the x, y and z axes as shown in Equation 5.5 the following relation can be solved for rotation angles α, β, γ

$$R_x(\alpha)R_y(\beta)R_z(\gamma) = R_{-y}(couch)R_{-z}(gantry)R_{-y}(col). \tag{5.10}$$

However, it is necessary to describe the motion of a BEAMnrc PSF with collimator, gantry and couch angles of that of the Clinac 21EX model. One must therefore account for an additional rotation required to initially align the BEAMnrc PSF with the top-dead-zero position of the collimator, gantry and couch angles. This extra rotation is required since the normal vector of the phase-space plane is initially aligned along the positive Z-axis of the patient c.s. (incident on the soles of the patient's feet). The initial alignment of the BEAMnrc phase-space plane with the top-dead-zero accelerator position is achieved through a rotation of $\frac{\pi}{2}$ about the X-axis or $R_x\left(\frac{\pi}{2}\right)$. The amended relation we need to solve is

$$R_x(\alpha)R_y(\beta)R_z(\gamma) = R_{-y}(couch)R_{-z}(gantry)R_{-y}(col)R_x\left(\frac{\pi}{2}\right) \tag{5.11}$$

or

$$\begin{bmatrix} \cos(\beta)\cos(\gamma) & -\cos(\beta)\sin(\gamma) & \sin(\beta) \\ \sin(\alpha)\sin(\beta)\cos(\gamma)+\cos(\alpha)\sin(\gamma) & -\sin(\alpha)\sin(\beta)\sin(\gamma)+\cos(\alpha)\cos(\gamma) & -\sin(\alpha)\cos(\beta) \\ -\cos(\alpha)\sin(\beta)\cos(\gamma)+\sin(\alpha)\sin(\gamma) & \cos(\alpha)\sin(\beta)\sin(\gamma)+\sin(\alpha)\cos(\gamma) & \cos(\alpha)\cos(\beta) \end{bmatrix} \tag{5.12}$$

$$= \begin{bmatrix} \cos(b)\cos(a)\cos(c)-\sin(b)\sin(c) & -\cos(b)\cos(a)\sin(c)-\sin(b)\cos(c) & -\cos(b)\sin(a) \\ -\sin(a)\cos(c) & \sin(a)\sin(c) & -\cos(a) \\ \sin(b)\cos(a)\cos(c)+\cos(b)\sin(c) & -\sin(b)\cos(a)\sin(c)+\cos(b)\cos(c) & -\sin(b)\sin(a) \end{bmatrix}$$

for rotation angles α, β, γ and gantry (a), couch (b) and collimator (c) angles. The solution of the three variables α, β, γ is overdetermined by the nine equations of the 3×3 matrix. It can be shown that a sufficient solution of this system for VMC++ rotation angles α, β, γ in terms of *gantry*, *couch* and *collimator* angles as follows

$$\alpha = \tan^{-1}\left[\frac{\cos(gantry)}{-\sin(couch)\sin(gantry)}\right], \tag{5.13}$$

$$\beta = -\tan^{-1}\left[\frac{\cos(couch)\sin(gantry)}{\sqrt{1-\sin^2(gantry)\cos^2(couch)}}\right], \quad \text{and} \tag{5.14}$$

$$\gamma = \tan^{-1}\left[\frac{\cos(couch)\cos(gantry)\sin(col)+\sin(couch)\cos(col)}{\cos(couch)\cos(gantry)\cos(col)-\sin(couch)\sin(col)}\right]. \tag{5.15}$$

Table 5.1: Beam parameters used to test the transformations for fields shown in Figure 5.3.

	Gantry Angle (deg.)	Couch Angle (deg.)	Collimator Angle (deg.)
Field 1	26.0	8.0	17.0
Field 2	107.0	49.0	99.0
Field 3	243.0	66.0	197.0

The transformations of Equations 5.13 - 5.15 were verified through comparison of VMC++ simulated dose distributions with those calculated by Eclipse for two different external beam plans, each of which contained three asymmetric photon

Table 5.2: Beam parameters used to test the transformations for fields shown in Figure 5.4.

	Gantry Angle (deg.)	Couch Angle (deg.)	Collimator Angle (deg.)
Field 1	10.0	59.0	266.0
Field 2	163.0	30.0	306.7
Field 3	318.0	92.0	88.0

fields. The field orientations are shown in Table 5.1 for the first plan and 5.2 for the second plan. The orientations were chosen to be the same as those previously used for testing the DOSXYZ transformations derived by Thebaut and Zavgorodni [Thebaut and Zavgorodni, 2006]. This combination of beam angles allows testing of the transformations in all clinically relevant quadrants and collimator angles. In each simulation 250 million particles were transported into a CT scanned cylindrical water phantom (radius = 10.0 cm, length = 20.0 cm) for each field.

For comparison with Eclipse field orientations the VMC++ calculated dose distributions were converted to DICOM format and imported into the Eclipse TPS.

5.2.2 VIMC-Arc

By its nature RapidArc treatment delivery is a dynamic process in which the dose is delivered with simultaneous gantry rotations and MLC motions. The delivered dose rate can also be variable. Motion of any linac component is described in DICOM files through the use of control points specifying where each linac component (such as gantry, MLC leaves and other) are required to be positioned at a specific point of the dose delivery. The required fraction of the total photon fluence will also be delivered at the specified control point. Other parameters, such as the collimator angle, couch angle, and jaw positions are specified outside of the control points (thus are currently kept constant throughout the arc). Similar to the VIMC system described above, the VIMC-Arc process uses DICOM files exported from the Eclipse TPS and extracts all data required for the MC calculation.

DICOM files produced by Eclipse represent each RapidArc treatment as a series of fields with 177 gantry positions, each associated with an MLC field aperture. Using this information, VIMC-Arc models the gantry arc rotation as a series of static gantry positions, with MLC motion modeled dynamically. Between each adjacent pair of gantry control points, a mean gantry angle is computed, representing a static VIMC-Arc gantry position 5.1. The MLC leaf positions for adjacent gantry angles are then used as the basis to create an IMRT MLC motion for this mean gantry angle. This implies that during a gantry rotation between two control points each leaf moves with a constant speed, though this speed varies from one leaf to another. VIMC-Arc therefore generates 176 sliding window IMRT radiation segments to model RapidArc dose delivery. The process of generating IMRT fields within an arc segment is depicted in Figure 5.1.

For each of the these 176 segments, MC input files are created along with the respective input files for the code modeling dynamic MLC motion [Keall et al., 2001; Siebers et al., 2002]. Each segment is treated as a separate radiation field and is

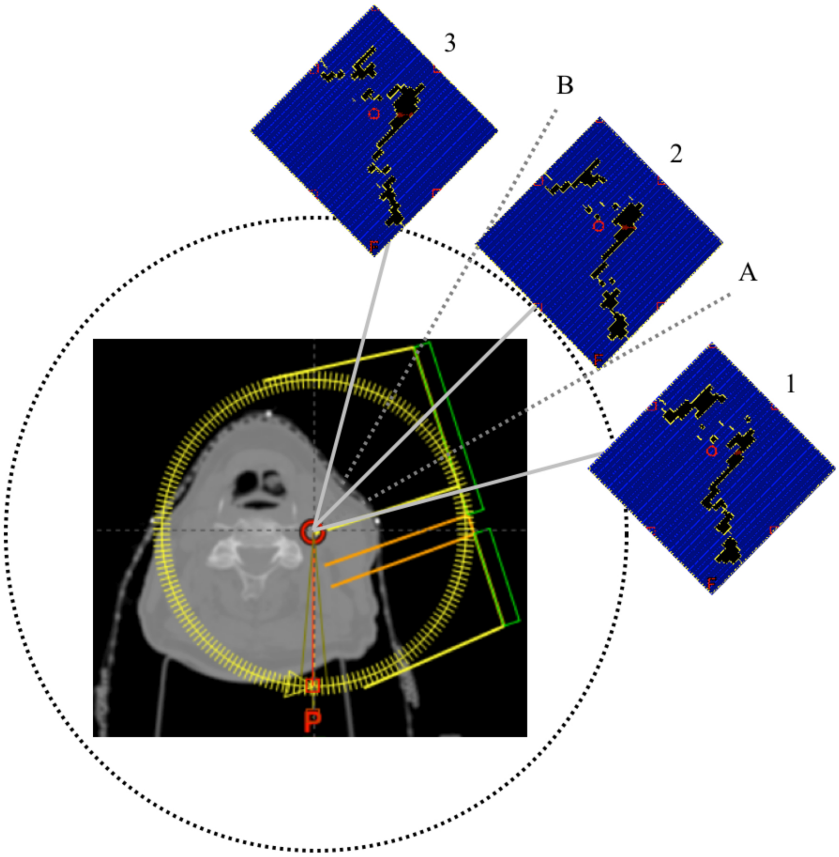

Figure 5.1: Diagram demonstrating the generation of IMRT fields within an arc segment. The RapidArc DICOM files from Eclipse provide values of gantry angles and MLC leaf positions at the gantry angles 1, 2 and 3. VIMC-Arc averages between the given gantry angles 1 and 2 to produce an "effective" gantry angle A, while the gantry angles 2 and 3 are averaged to produce an effective gantry angle B. The MLC leaf positions at points 1 and 2 are used to produce a dMLC file that controls leaf motions from point 1 to point 2 at the gantry angle A. Similarly, the MLC leaf positions at points 2 and 3 are used to produce a dynamic MLC motion pattern for the gantry angle B. The angles as portrayed in this figure are shown for demonstration purposes only; actual RapidArc gantry rotation segments are on the order of 2 degrees.

simulated independently. The number of histories required to simulate in each rotation segment is determined by the same method as per a standard IMRT VIMC plan with multiple fields described by Equation 5.1. VIMC-Arc also has the capability of modeling an arbitrary number of arcs.

The Eclipse TPS has the option of optimization with "avoidance sectors" - arc sectors where radiation has been prohibited during optimization in order to minimize the dose delivered to particularly sensitive structures in a patient. In DICOM plan

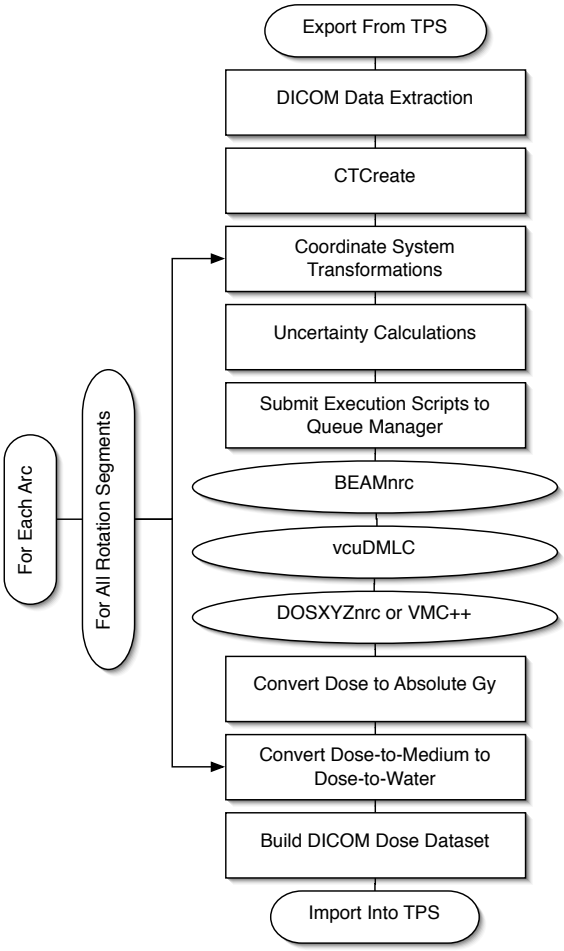

Figure 5.2: Flowchart exhibiting the steps making up the VIMC-Arc process.

files these sectors are recorded as gantry positions with non-increasing beam meter set weights. VIMC-Arc detects such sectors in the DICOM dataset and accounts for them by ignoring MC beam segments for these gantry positions. The number of particles required to achieve the user requested dose uncertainty will then be automatically redistributed between remaining arc segments.

A Condor job submission script is written for each segment to execute BEAMnrc, particle DMLC code, and either of DOSXYZnrc or VMC++. Because each segment is treated by VIMC-Arc as an individual field, each segment produces an independent 3D dose distribution that is subsequently converted to absolute dose. The variable dose rate is accounted for in this conversion by using the DICOM RT parameter

"beam meter weight" that specifies the fractional monitor units (MUs) to be delivered by a given gantry angle within each treatment arc. VIMC-Arc extracts the value of this parameter from the DICOM plan file and calculates the MUs to be delivered in each segment. This is different from the original VIMC process, where the MU for each field would be obtained explicitly from the respective DICOM plan file.

Following the absolute dose conversions applied to the set of 3D dose files, the dose (in Gy) from all 176 rotation segments of each arc are combined into a single arc dose distribution. If requested, this dose distribution is then converted to absorbed "dose to water" and finally written into DICOM dose files, allowing import of the MC calculated dose into a commercial TPS for evaluation. A flowchart showing the steps required to carry out the VIMC-Arc simulation process is displayed in Figure 5.2

5.2.3 VIMC-Arc tests and verifications

Essential components of the VIMC system utilized by VIMC-Arc, have been tested and previously verified. This includes open field profiles and depth dose curves [Gagné and Zavgorodni, 2007], absolute dose calculations including sliding window IMRT [Popescu et al., 2005], sliding window IMRT profiles [Stapleton et al., 2005] as well as IMRT patient dose calculations [Zavgorodni et al., 2007].

Patient plans were calculated by the Eclipse TPS for RapidArc delivery and then transferred to an artificial water-equivalent cylindrical phantom. The plans were designed to demonstrate the applicability of the VIMC-Arc system for

(i) a single-field RapidArc treatment,

(ii) a dual-arc RapidArc treatment,

(iii) a RapidArc plan where avoidance sectors were used during treatment planning.

VIMC-Arc calculations were compared with RapidArc dose distributions produced by the anisotropic analytical algorithm (AAA). As AAA has been proven to

produce accurate dose distributions in homogeneous media [Fogliata et al., 2006], [Gagné and Zavgorodni, 2007], the AAA calculated dose distributions offer a valid comparison measure for the VIMC-Arc system in homogeneous phantoms. A single-arc RapidArc treatment plan was also simulated on an inhomogeneous patient phantom to observe dose differences introduced from phantom inhomogeneities.

5.3 Results

5.3.1 Verification of IEC coordinate transformations for clinical phase-space based VMC++ simulation

A verification of IEC coordinate transformations derived in Section 5.2.1 is made through comparison of two, three field IMRT (non-arc) plans with Eclipse and VIMC. Transverse and sagittal planar comparisons of the dose distributions are displayed in Figures 5.3 and 5.4. This agreement demonstrates the validity of the derived transformations for a set of gantry, collimator and couch angles that cover clinically relevant quadrants. This validation naturally extends to the VMC++ simulation of RapidArc delivery.

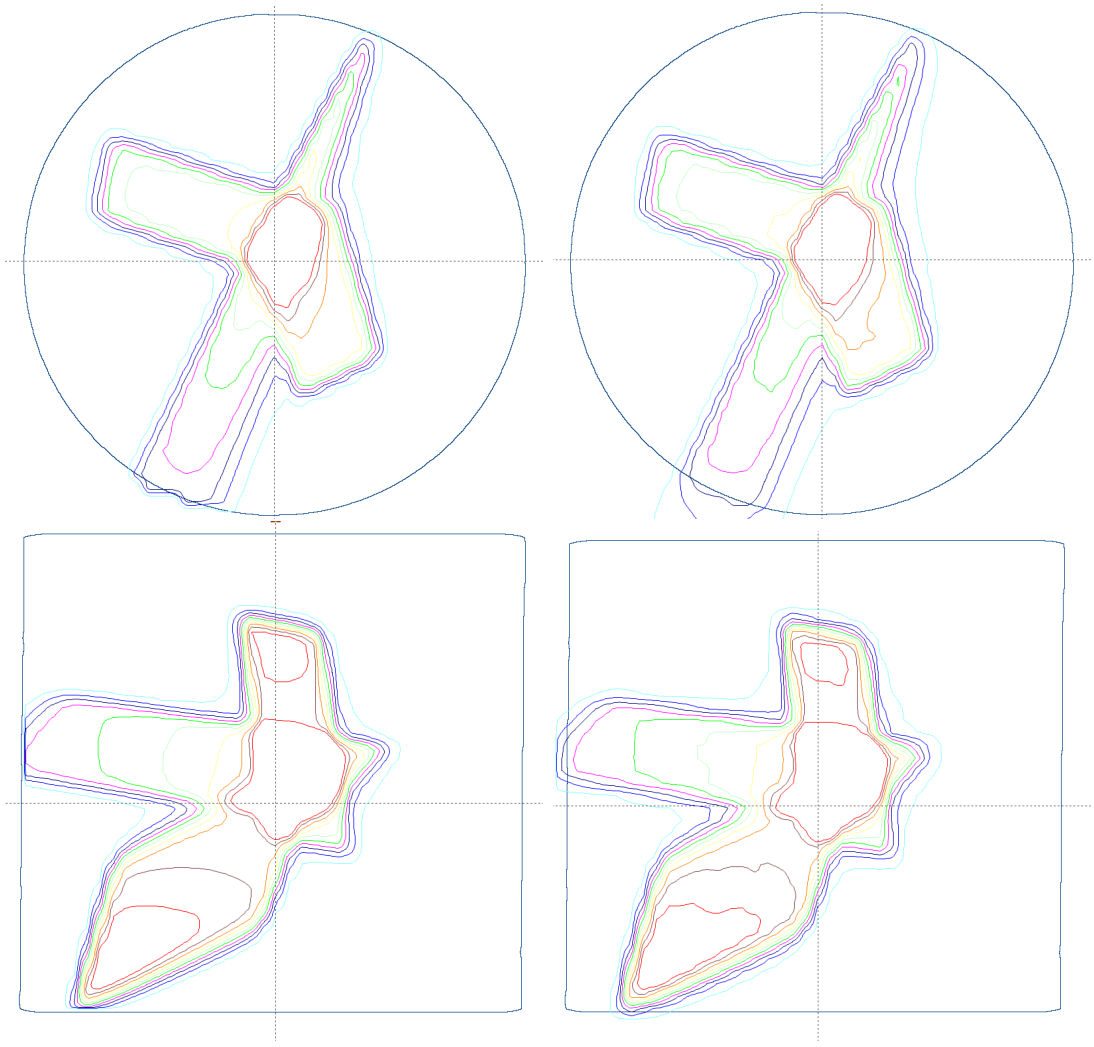

Figure 5.3: Transverse *(top)* and sagittal *(bottom)* cross-sections of dose distributions from three fields calculated by Eclipse *(left)* and VMC++ *(right)* for beam angle parameters defined in Table 5.1. The surface contour of the cylinder is shown in dark blue.

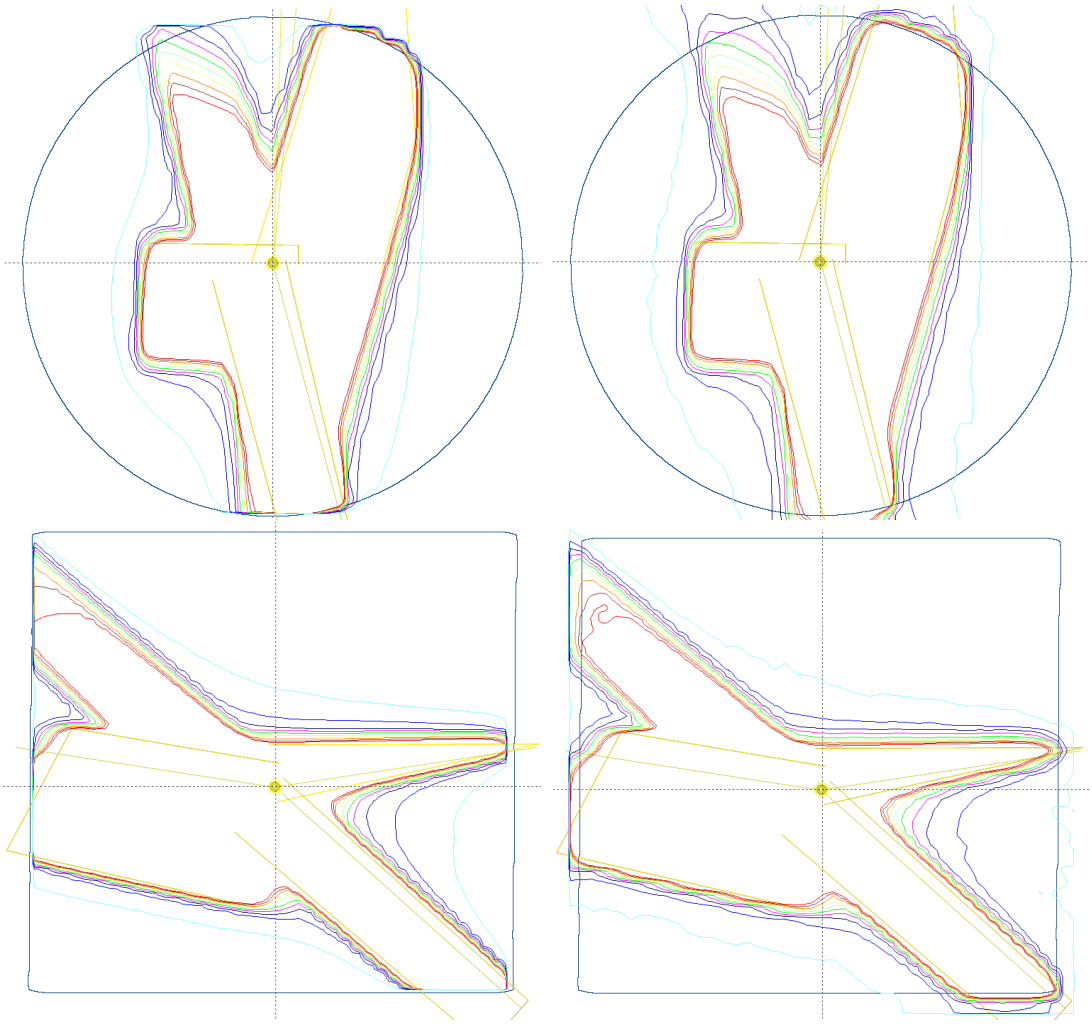

Figure 5.4: Transverse *(top)* and sagittal *(bottom)* cross-sections of dose distributions from three fields calculated by Eclipse *(left)* and Monte Carlo *(right)* for beam angle parameters defined in Table 5.2.

5.3.2 Verification of the VIMC-Arc simulation process

Table 5.3 provides a summary of the test simulations that have been completed specifically for the VIMC-Arc feature of the VIMC system. All plans were calculated on phantoms with $0.5 \times 0.5 \times 0.5$ cm^3 voxels, and the number of particles was calculated by VIMC-Arc to achieve at least 1% uncertainty at isocenter. Table 5.3 also demonstrates the dependence of the number of histories (and hence, the simulation time) on the field size defined by the secondary collimator jaws for MC calculations. This number of becomes approximately constant if normalized per unit area of the secondary collimator aperture. VIMC-Arc dose calculations required an average of approximately 59.5 minutes on a 9-node PC cluster each with a 2.2 GHz CPU, while Eclipse calculations required an average of 4.8 minutes for dose calculations on an 8-core 3.0 GHz workstation.

Table 5.3: Summary of VIMC-Arc verification simulations.

Plan	Beam Area (cm^2)	Histories ($\times 10^9$)	MC Time (minutes)	Eclipse Time (minutes)	Dose Difference
1-Arc Cylinder	254.40	1.652	50	3.50	0.5%
2-Arc Cylinder	228.00	1.481	62	6.82	0.6%
Avd. Sectors	478.01	3.109	69	4.47	-0.8%
1-Arc Patient	254.40	1.652	57	4.38	-0.6%

The last column of Table 5.3 provides a comparison of percentage differences of the dose calculated at the plan's isocentre between VIMC-Arc and Eclipse. Agreement was found to be within MC statistical uncertainties in all cases.

The dose distribution from a single-field RapidArc treatment plan calculated on a water-equivalent cylinder is displayed in Figure 5.5. Agreement between the Eclipse AAA and VIMC-Arc dose distributions was observed.

Figure 5.6 demonstrates VIMC-Arc's ability to model a dual-arc RapidArc treatment. Multiple arcs may be required in practice to extend the effective treatment

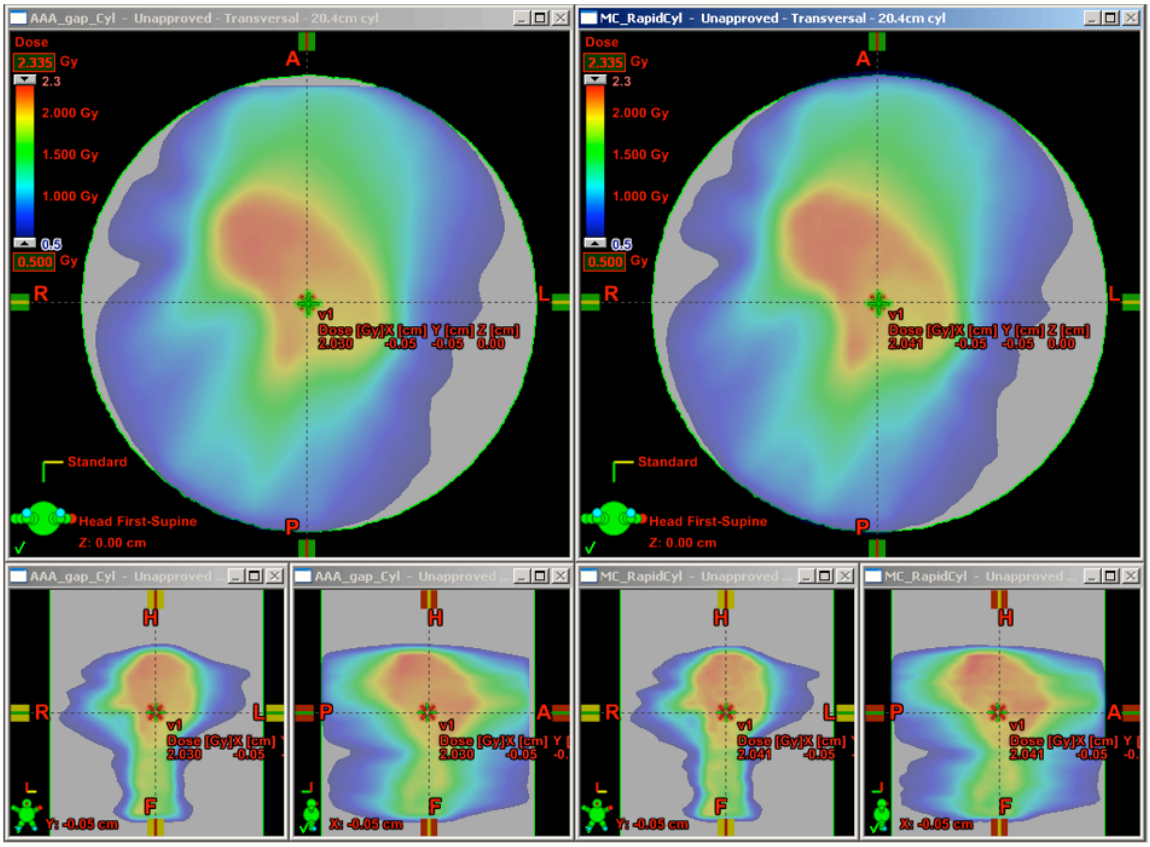

Figure 5.5: Comparison of the AAA *(left)* and VIMC-Arc *(right)* dose distributions from the regular single arc plan on a cylindrical water-equivalent phantom. The uncertainty of MC dose calculation was within 1.0%.

field size, as currently RapidArc does not allow MLC carriage movement. Again, the agreement of VIMC-Arc and Eclipse dose distributions confirms a correct implementation of this treatment option in the system.

The verification plan shown in Figure 5.7 was produced utilizing the sector avoidance option in the Eclipse optimization stage. Good agreement of VIMC-Arc and Eclipse dose distributions was observed, establishing the ability of VIMC-Arc to accurately model this option.

Finally, to observe potential dose calculation differences with the presence of phantom inhomogeneities, dose for a RapidArc patient plan was calculated using the VIMC-Arc system and compared with AAA dose calculations as shown in Figure 5.8. It should be noted that the plan was identical to that used on the verification

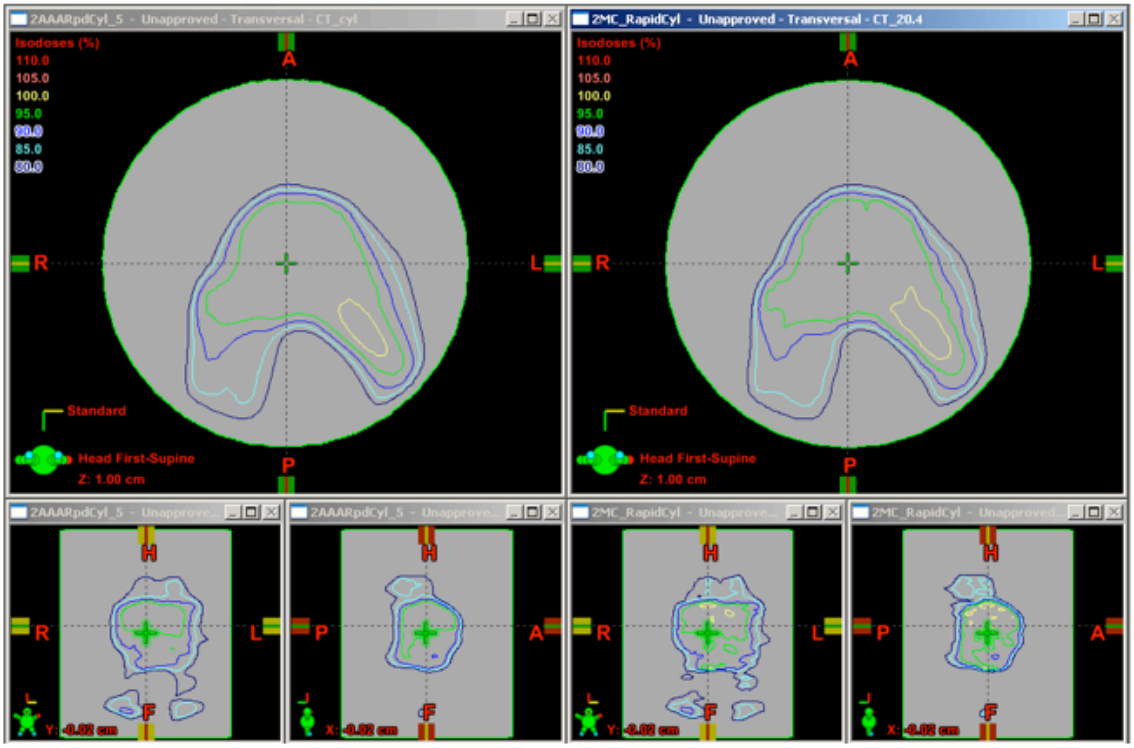

Figure 5.6: Comparison of the AAA *(left)* and VIMC-Arc *(right)* dose distributions from dual-arc plan in water equivalent cylindrical phantom. The uncertainty of MC dose calculation was within 1.0%.

cylinder shown in Figure 5.5. In this case the dose distributions produced by Eclipse and VIMC-Arc are very similar, with minor differences appearing in the regions of tissue inhomogeneities.

Figure 5.7: Comparison of the AAA *(left)* and VIMC-Arc *(right)* dose distributions from a treatment plan using the avoidance sector option. The uncertainty of MC dose calculation was within 1.0%.

Figure 5.8: Comparison of the AAA *(left)* and VIMC-Arc *(right)* dose distributions from a standard single arc plan on a patient. The uncertainty of MC dose calculation was within 1.0%.

5.4 Discussion and Conclusions

RapidArc delivery is among the most complex modern radiotherapy treatment techniques. In this chapter an automated VIMC-Arc system enabling the Monte Carlo dosimetric verification of treatment plans generated by commercial software for RapidArc delivery (Eclipse) has been presented. In addition to dosimetric verification, VIMC-Arc offers the ability to model treatment options that are not yet clinically available, such as variable dose rate delivery combined with simultaneous motion of all movable components of the radiotherapy treatment delivery unit: gantry, MLCs, collimator, jaws, and couch. This potential may allow for future Monte Carlo verifications of highly complex dynamic treatment techniques where traditional pencil-beam-based algorithms will be further challenged for both accuracy and speed.

In its development RapidArc evolved from IMAT and VMAT [Otto, 2008] treatment techniques. Naturally, Monte Carlo verification methods for IMAT would have similarity to those for RapidArc. However, as IMAT has not yet been embraced as widely as fixed gantry IMRT, there are respectively less publications on Monte Carlo modeling of this technique. Recent publications by Gladwish *et al.* and Vanderstraeten *et al.* [Gladwish et al., 2007; Vanderstraeten et al., 2007] do not provide detailed description of the Monte Carlo implementation. An article by Li *et al.* [Li et al., 2001] describes in detail the IMAT Monte Carlo verification process. In their model, approximations were introduced that, although justified for IMAT with its relatively open apertures and gradually changing field shapes, would be insufficient for RapidArc. This includes a fairly coarse angular grid of 10 for gantry positions, the modeling of dynamic IMAT fields as fixed apertures, ignored interleaf leakage and tongue and groove effects. The implementation of VIMC-Arc makes none of these approximations. The dMLC motion is explicitly modeled, including the tongue and groove effect as well as interleaf leakage [Keall et al., 2001; Siebers et al., 2002]. The

number of gantry segments used in the VIMC-Arc system is identical to that in the Eclipse TPS.

Reducing the number of gantry positions modeled in the system would not gain significant calculation speed, and increasing this number would not result in any loss of efficiency. If needed, it is possible to increase the accuracy of the gantry motion modeling in VIMC-Arc by interpolating the 176 rotation segments into several hundred, or even thousands of segments. However, such an increase would inevitably involve interpolating between gantry positions provided in the DICOM plan file used to control the linac motion. Given that all provided gantry segments are already modeled, and the dynamic motion of the MLC leaf motion has been accurately modeled, further increase of the number of gantry segments may only produce minute differences in the calculated dose distribution, and are most likely not required.

It is important to note that the VIMC-Arc system is capable of routine RapidArc plan dose verification where the process requires only minimal user input such as patient ID, required voxel size and requested dose uncertainty. The remainder of the process is fully automated. This provides an excellent platform for investigations of potential dosimetric problems in different treatment sites with varying degrees of tissue inhomogeneity.

Within this chapter the validation of the VIMC-Arc system did not involve direct experimental measurements from a RapidArc delivery. This is because RapidArc capable linacs are not yet available in the author's institution. However, as demonstrated in the Section 5.2.2, all dosimetrically important components of the Monte Carlo system have been verified in previous studies. Good agreement of the VIMC-Arc calculations with AAA in homogeneous phantom, where the AAA is believed to be accurate, were also demonstrated.

It should be reiterated that a quantitative dosimetric analysis of RapidArc dose distributions was not the subject of this chapter. A study of the dosimetric accuracy

of RapidArc for oropharynx radiotherapy has been performed using VIMC-Arc by VIC medical physics researchers [Gagne et al., 2008]. In their paper investigating a cohort of six patients, a dosimetric error of up to 12% near isolated MLC leaf edges and up to 5% at MLC leaf ends was observed. The composite effect of these errors was found to produce a 1.5% error in mean target dose. At present the study of Gagne *et al.* is the only published comparison of AAA and MC dose calculations of RapidArc delivery.

Chapter 6

Monte Carlo Calculated Beamlet Dose Distributions for Advanced Radiotherapy Planning

Based on Bush *et al.*, Phys. Med. Biol. **53**, 18 (2008)

In the previous chapter a framework was established allowing the *verification* of arc therapy treatments with Monte Carlo (MC) dose calculation. In this chapter the initial steps toward introducing MC dose calculation in the *planning* stages of advanced radiotherapy treatments will be investigated.

6.1 Introduction

The importance of accurate dose calculations in the planning stages of IMRT treatments was recently demonstrated by Mihaylov and Siebers [Mihaylov and Siebers, 2008] in their study of optimization convergence errors in pencil beams. The use of MC dose calculation in the IMRT plan optimization process poses several challenges as previously discussed in the literature [Verhaegen and Seuntjens, 2003; Zakarian and Deasy, 2004; Chetty et al., 2007]. Perhaps the most significant, at present date, are the computationally intensive nature of MC simulation and difficulties that can exist in accurately representing the output of the treatment head being modeled.

Several groups thus far have implemented Monte Carlo based beam-element (beamlet) or fluence-element type IMRT optimizations for radiotherapy applications. Jeraj and Keall [Jeraj and Keall, 1999] have used MC beamlets in a Monte Carlo inverse (MCI) treatment planning method. The technique employs a hybrid investigation tool, in which an initial guess of the beam modulation is first derived without electron transport, followed by a forward MC simulation including electron transport. Jeraj and Keall [Jeraj and Keall, 2000] have also investigated the noise convergence error effects specific to the use of MC beamlets in dose optimization. The clinical feasibility of a similar hybrid MC method was also investigated by Wang *et al.* [Wang et al., 2005]. Other groups have used beamlets in fast MC dose calculation engines such as VMC++ and XVMC [Ma et al., 2002; Zakarian and Deasy, 2004; Bogner et al., 2006]. Zakarian and Deasy used a modified version of the XVMC code to simulate beamlets in a homogeneous water medium and investigated the compressibility

of the dose data with wavelet-based multi-resolution (MR) decomposition. Bogner *et al.* developed a non-hybrid, fluence based, inverse MC treatment planning system based on the concept of inverse kernel optimization. Lindsay *et al.* [Lindsay et al., 2007] have also implemented MC beamlets derived from a simplified beam model to analyze an archived dataset of lung plans.

With the exception of Bogner *et al.* a particle source model (PSM) or multi-source model approach was implemented in each of the above methods to generate the particles of each beamlet. Verhagen and Seuntjens [Verhaegen and Seuntjens, 2003] have stated that the nature of such source models inevitably introduce approximations to the radiation field. For accurate modeling of accelerators such as the Clinac 21EX type model, where the multi-leaf collimator is below the secondary collimating jaws, a beamlet PSM originating from the MLC plane would require a source model for all components down to and including the secondary collimating jaw. Many groups have successfully derived PSM's up to but not including the secondary collimating jaws [Ma and Rogers, 1995; Ma, 1998; von Wittenau et al., 1999; Deng et al., 2000; Fix et al., 2000, 2001; Ma et al., 1997]. The absence of cylindrical symmetry below the secondary collimator along with patient dependent variations in field size, make this location less favourable for a source characterization point although models do exist [Chetty et al., 2000; Aaronson et al., 2002].

Conventional dose calculations, i.e. those not employing MC often rely on analytic methods such as pencil beam convolution or collapsed cone convolution for calculation of beamlet dose distributions. Because of the relatively few computations required to calculate beamlet dose distributions with these algorithms, beamlet dose distributions are typically recalculated "on-the-fly" for each optimization iteration to determine the resulting dose from each beamlet weight change. An alternative approach, as suggested by Bogner et al. [Bogner et al., 2006], Zakarian and Deasy [Zavgorodni et al., 2007], and Bush [Bush and Popescu, 2006] is to perform a one-time

calculation of all beamlet dose distributions, store all distributions (in RAM), and weight the stored dose distributions for each optimization. This approach requires significantly more memory than recalculating beamlet dose distributions, something which was not sufficiently available during the peak development of IMRT optimization in the early 1990s. The computational load required for MC dose calculation is significant such that storage of MC calculated beamlet dose distributions is essential for fast optimization. Recalculating beamlet dose distributions with MC simulation is impractical given the required computation.

To determine an estimate of the quantity of uncompressed data required for a typical IMRT treatment plan, one could consider a typical 7 field treatment with an approximate treatment area of 15.0×15.0 cm^2 per treatment field. Using a modest beamlet size of 0.5×0.5 cm^2 one would require approximately 900 beamlets per field or $7 \times 900 = 6300$ beamlets for the entire 7-field plan to cover the planning target volume. Under the assumption of an average number of dose calculation points per beamlet to be on the order of 10 000 (assuming a modest voxel grid of $100 \times 100 \times 100$ and dose data within the PTV and OAR contained in one-tenth of these voxels), the uncompressed memory requirements to store/buffer all dose data would be on the order of > 1.2 gigabytes (GB) with 16-bit precision. For todays most powerful desktop computers this memory requirement is feasible. However, the demands of modern advanced radiotherapy treatments using treatment arcs typically require many more fields (for example a RapidArc treatment plan requiring 177 fields per treatment arc). In addition, the incorporation of a time domain in the planning process may require even more beamlet data storage. It is not feasible to incorporate MC dose calculation in such advanced treatments with the current optimization architecture.

Compression of beamlet dose distribution data has the potential to yield more manageable memory requirements. Zakarian and Deasy [Zakarian and Deasy, 2004] have shown the potential for near lossless compression of up to 100 times using

multi-resolution wavelet decomposition of dose distributions with hard thresholding (i.e. zeroing below a cutoff) of wavelet coefficients below a value of 1% of the maximum. In addition, the decomposed dose distributions were simultaneously de-noised. As implemented by this group, a 2-D discrete wavelet transform was performed on multiple 2-dimensional slices of the 3-dimensional dose distribution using a selection of wavelets (orthogonal and biorthogonal). The wavelet transform was limited to 2 dimensions by the Matlab[1] software used for their analysis. It was suggested by this group that improved compression would come from using a 3-D transform in the decomposition.

In this chapter, a method will be presented to generate Monte Carlo beamlets using a BEAMnrc phase space at the plane of the MLC for use in IMRT, volumetric modulated arc therapy (VMAT), and/or intensity modulated arc therapy (IMAT) optimization. It is expected that MC beamlets generated from the phase space will provide a basis for more accurate modeling of the radiation field. The compressibility of beamlet dose distributions will also be investigated for the first time using a 3-D wavelet transform.

6.2 Materials and Methods

MC simulations were made using the BEAMnrc and DOSXYZnrc Monte Carlo system, based on the underlying EGSnrc particle transport code [Kawrakow and Rogers, 2000]. The following MC transport parameters were used in all simulations [Rogers et al., 2006] [Walters et al., 2005; Sheikh-Bagheri and Rogers, 2002b]: AP=PCUT=0.010 MeV and AE=ECUT=0.700 MeV, where AP and AE are the low-energy thresholds for the production of secondary bremsstrahlung photons and knock-on electrons, respectively, while PCUT and ECUT define the global cutoff energy for photon and electron transport, respectively. Directional bremsstrahlung

[1]The Mathworks, Inc., Natick, MA, USA.

splitting was also used with a splitting factor NBRSPL=1000. The accelerator model, a Varian Clinac 21EX, was defined according to manufacturer specifications.

The process of obtaining MC beamlet dose distributions consists of 3 parts: phase space sorting and beamlet extraction, doselet acquisition, and doselet conversion to absolute dose.

6.2.1 Generating Monte Carlo beamlets from a BEAMnrc phase space

Phase space sorting and beamlet extraction

In the context of this chapter, the term beamlet (or beam element) is defined as a geometrical sub-division of a given radiation field. The basis for sub-division is a two dimensional grid with spacing dx $\times$ dy through which the radiation field passes at normal incidence (Figure 6.1). The placement of this grid along the direction of propagation (Z) is arbitrary, a feature that, as will be discussed, enables additional applications of beamlets beyond intensity modulated radiotherapy (IMRT) planning. The dose distribution deposited in a phantom by all particles of a single beamlet will be referred to as a doselet. This distribution is stored as a 3-D matrix along with the associated dose uncertainties and voxel boundaries.

A phase space file (PSF), in the MC simulation context, can be considered a "snapshot" of a set of particle characteristics for a field of particles crossing a particular two-dimensional plane in space. These characteristics in BEAMnrc simulations include those essential for the continuation of MC particle transport (energy, momentum, type), and others that aid in simulation statistics (weight) and analysis (LATCH). A particle record consists of 7 or 8 (depending on the scoring mode used) 32-bit variables: LATCH, energy (MeV), x coordinate (cm), y coordinate (cm), x direction cosine, y direction cosine, particle weight (which also stores the sign of the z direction cosine), and z coordinate of the last particle interaction (optional). It is important to note that particles are written to the PSF in the order in which they

reach the scoring plane and are in no way ordered by their PSF variables. It is also important to note that the particle density in the PSF changes across the radiation field and is subject to field non-uniformity as well as statistical uncertainty inherent in MC modeling. It is therefore impossible to predict how many particles will be located in each geometrical region.

The LATCH variable can be used to track the origin and interaction history of each particle within the linac model[Rogers et al., 2006]. Up to 23 geometric regions of the accelerator's component modules can be mapped to specific bits (1 to 23) of the 32-bit LATCH variable. In the present work the LATCH variable is used in a somewhat different way to that which it was intended: To map beamlet regions in the phase space (rather than regions in the MC model) to binary beamlet numbers.

The PSF can therefore be indexed by labeling all particles contained within a given beamlet by the corresponding beamlet number. This is accomplished by reading each particle's position, determining the beamlet in which it is located, and embedding the binary representation of the beamlet number into the LATCH variable.

The LATCH variable could not have been used in its original design, since it was limited to a maximum of 23 geometric regions. A schematic overview of the use of the LATCH variable is shown in Figure 6.2.

Once indexed, the method then sorts the PSF by the beamlet number index. Initial implementations of the sorting method used an inclusive/exclusive LATCH bit filter technique similar to that currently available in DOSXYZnrc [Walters et al., 2005]. This method was found to be extremely inefficient in collecting doselets as the entire phase space had to be read and re-read a large number of times to locate all particles of a given beamlet. Efficient sorting of the PSF was crucial to maintaining the overall simulation efficiency.

The new method achieves a sorted phase space in just two passes of the PSF. During the first read (which also performs the indexing of the PSF as described

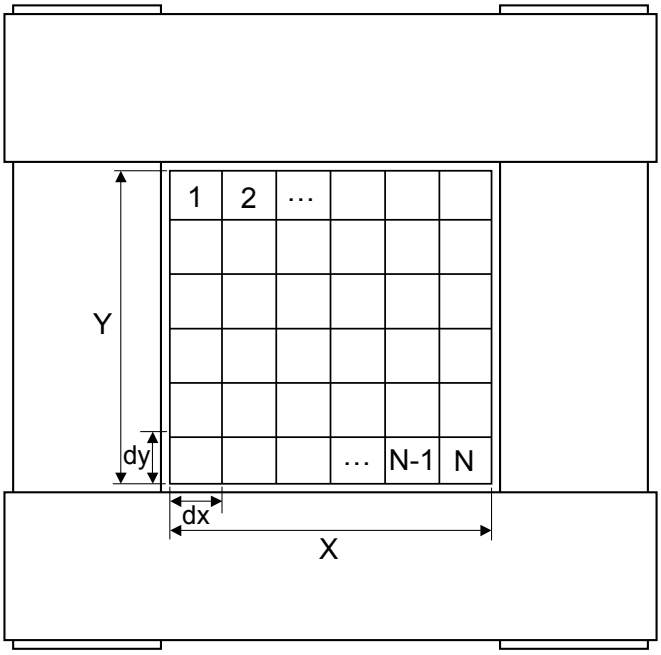

Figure 6.1: Sample grid used to segment the phase space into beamlets. The choice of numbering is completely arbitrary and can be adapted for the specific application. The beamlet numbering scheme is shown in this example starting from the y < 0 and x < 0 quadrant of the secondary collimator coordinate system. All particles positioned outside of the grid form an additional "outer beamlet".

Figure 6.2: Bit regions making up the LATCH variable. In order to index the phase space beamlet numbers are assigned to each particle in the shaded bit region (B). By writing the beamlet numbers into the LATCH variable, the particles of each beamlet and all associated secondary particles can be tracked throughout a simulation.

above) the sorting algorithm determines the number of particles in each beamlet and establishes the appropriate file pointers to the start of each beamlet location's memory address. During the second pass each particle is read from the original PSF and placed in the appropriate location in the sorted PSF.

At runtime each beamlet is quickly extracted from the sorted phase space file into a smaller PSF containing only the particles of a single beamlet. During this process the PSF header for each beamlet is written as required by EGSnrc to reflect the number of particles, photons, minimum electron energy and maximum energy in the single beamlet. The number of particles from the original source, however, is written to reflect that of the complete PSF. This is essential to ensure that dose normalization per incident particle is consistent from beamlet to beamlet.

In total, a grid of N elements produces N+1 beamlets, where the additional beamlet contains all particles outside of the defined beamlet grid. The grid size is generally selected to reflect the secondary collimator setting. Recording the additional beamlet outside of the beamlet grid ensures all particles contributing to the dose are kept and transported, not just those within the defined beamlet grid.

Using the above technique, secondary electrons are unambiguously assigned to the beamlet that caused the primary interactions that set them in motion.

History-by-history uncertainty implications

Sorting the PSF has significant implications for the history-by-history method of uncertainty calculation [Walters et al., 2002]. Using this method, a PSF is generally ordered in groups of correlated parent-child particles. Reordering the PSF by beamlet number breaks the correlated particle ordering. As such, the history-by-history method is not valid with phase space beamlets and thus batch-based uncertainty estimation is used at present.

6.2.2 Doselet acquisition

Following the PSF sorting and beamlet extraction stage, each beamlet PSF is transported separately into a phantom. It should be noted that this can be executed using any MC code capable of handling a PSF input. Each beamlet, as transported into the phantom, provides an individual dose distribution (doselet) in the whole phantom

(the MC analogue of a pencil beam kernel), reflecting accurately any inhomogeneity effects. For storage efficiency purposes, the resulting doselets are appended into a single binary dose file. Once this process is completed, the beamlet PSF's can be removed to conserve hard disk space.

One necessary modification of DOSXYZnrc was made to change the emphasis in the code of simulating an exact specified number of histories; to simulating all particles of a PSF an exact number of recycled times. In the distributed version of DOSXYZnrc, the user requests a specific number of histories be simulated into the phantom. As a result, it is possible that a PSF is not completely used or is restarted and partially rerun. Due to the potentially low number of particles in each beamlet, not running or rerunning even a small number of particles in a beamlet has a potentially dramatic effect on the acquired doselet distribution. For this reason, it was made certain that DOSXYZnrc ran exactly an integer multiple of the number of particles in the PSF. Thus, the number of particles actually simulated is governed by the requested number of recyclings and not by the requested number of histories.

Doselet normalization

When a phase space is used as a source for DOSXYZnrc simulation, the dose in a voxel is normalized by an estimate of the number of particles incident from the original, non-phase space source (NP) [Walters et al., 2005]:

$$NP = NINCSRC\left[\frac{NCASE + nsmiss + (NRCYCL + 1)(nsrjct + nsoutside + ndbsrjct)}{nshist}\right], \tag{6.1}$$

where:

- $NCASE$ is the number of histories to be simulated in a DOSXYZnrc run.
- $nsmiss$ is the number of particles rejected because they missed the geometry.
- $nsrjct + nsoutside + ndbsrjct$ is the total number of particles rejected in DOSXYZnrc because of user defined restrictions (LATCH setting, direction,

crossed the phase space plane more than once, were beyond the user-selected field, or rejected because of directional bremstrahlung splitting).

- $NRCYCL$ is the number of times each particle in the phase space is requested (or calculated) to be recycled.
- *nshist* is the DOSXYZnrc notation for the total number of particles contained in the incident PSF.
- $NINCSRC$ is an estimate of the number of particles incident from the original particle source to generate the PSF.

For transport of the beamlets into the phantom with DOSXYZnrc a slight modification to the dose normalization was made. The new formula reflects the fact that, in the implemented version of the code, all particles present in a single beamlet PSF are recycled the same number of times as every other beamlet PSF. The normalization has been modified to be

$$NP = NINCSRC \cdot (1 + NRCYCL)\,. \tag{6.2}$$

In other words, NP is simply given by the number of particles required to create the incident phase space multiplied by the number of times each particle is to be simulated.

6.2.3 Doselet conversion to absolute dose

The MC calculated doselets are converted to absolute dose using a calibration method that fully accounts for the backscatter to the monitor chamber of any given treatment field [Popescu et al., 2005]. The conversion factors specific to any open field will also apply to each individual beamlet originating from that open field. Therefore the dose to voxel (x, y, z) from a beamlet j ($D^j_{xyz,abs}$), is obtained based on the relation derived by Popescu *et al.* as

$$D^{j}_{xyz,abs} = D^{j}_{xyz} \frac{D^{forward}_{ch} + D^{back(10\times10)}_{ch}}{D^{forward}_{ch} + D^{back}_{ch}} \cdot \frac{D^{cal}_{xyz,abs}}{D^{cal}_{xyz}} \cdot MU, \tag{6.3}$$

where:

- D^{j}_{xyz} is the dose per incident particle to voxel (x, y, z) in doselet j.
- $D^{forward}_{ch}$ is the dose per incident particle deposited in the monitor chamber from the complete set of beamlets traveling though the chamber in the forward direction.
- D^{back}_{ch} is the dose per incident particle deposited in the monitor chamber from the complete set of beamlets scattered back toward the monitor chamber.
- $D^{back(10\times10)}_{ch}$ is the dose per incident particle deposited in the monitor chamber from the complete set of beamlets scattered back toward the monitor chamber for a calibration 10×10 cm^2 simulation.
- D^{cal}_{xyz} is a reference point dose from the 10×10 cm^2 calibration simulation for which to calibrate the dose per incident particles.
- $D^{cal}_{xyz,abs}$ is a physical measurement made at the same point of acquisition as D^{cal}_{xyz}.
- MU is the number of monitor units to be delivered to obtain the complete set of doselets.

6.2.4 Doselet Compressibility

The need for the compression of dose distributions comes from the requirement of storing a large number of dose calculation points within a patient for a large number of beamlets. As discussed earlier, it is currently not feasible to re-simulate and obtain beamlet dose distributions "on-the-fly" during the iterations of an optimization.

A comprehensive introduction to multi-resolution (MR) wavelet decomposition can be found in Mallat, 2008 [Mallat, 2008]. A brief introduction will now be presented.

Wavelet transforms employ basis functions that are localized in both frequency and time. The wavelet transform expresses a given signal in terms of simpler signals built from stretched or contracted versions of a "mother wavelet". Because of their ability to decompose a given signal with variable time-frequency resolution (multi-resolution (MR) decomposition), wavelets are well suited to image (and therefore dose) compression applications.

The 1-dimensional dyadic MR decomposition and reconstruction process is outlined in Figure 6.3. Signal V is passed through high and low pass filters H_D and L_D. The result of each then is downsampled by a factor of 2. The high pass result of wavelet coefficients refers to the details of V while the low pass result is a lower resolution approximation of V. The low pass result is passed through the high and low pass filters again and the process is repeated nl times (decomposition levels). Reconstruction of signal V is achieved through the reverse process.

The 2-dimensional dyadic MR decomposition scheme (used in image compression) operates in a similar way with the addition that 1-D MR decomposition is performed independently along the "row" and "column" directions as well as a "row" then "column" directions of the signal (image). The 3-dimensional dyadic MR decomposition is performed independently along all permutations of the "row", "column" and frame directions of the signal (volume).

Hard thresholding of wavelet coefficients has been used by Zakarian and Deasy which consists of setting all wavelet coefficients below a defined threshold to zero. The same approach is implemented in this research.

The decomposition and thresholding does not compress data in any way. Compression of data would be achieved through the process of quantization and encod-

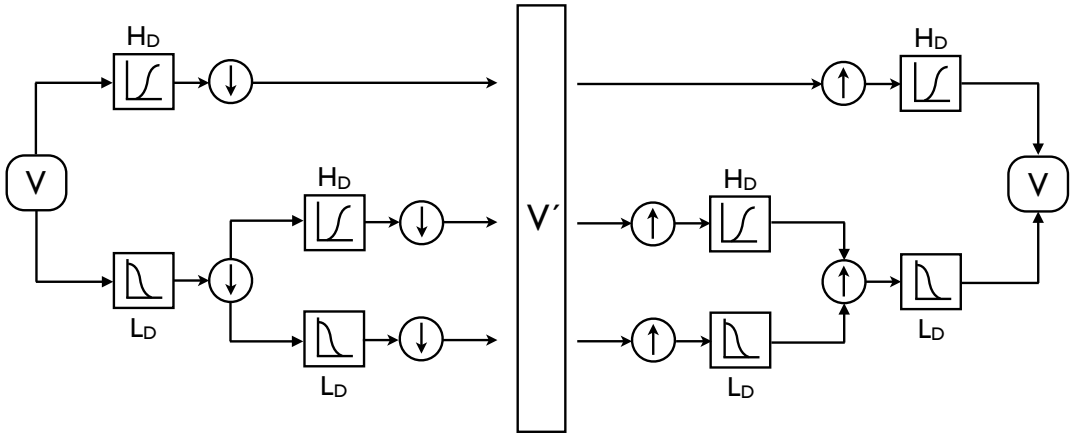

Figure 6.3: 1 dimensional dyadic multi-resolution discrete wavelet decomposition and reconstruction of dose matrix V. H_D and L_D are high and low pass decomposition filters respectfully. H_R and L_R are high and low pass reconstruction filters respectfully. The downward arrow represents downsampling by a factor of two while the upward arrow represents upsampling by a factor of two. V′ are the derived wavelet coefficients.

ing of the transformed result. A large number of acceptable quantization/encoding schemes exist but are beyond the scope of this dissertation as a proper investigation would require a significant body of work on its own. In this chapter a similar level of investigation of wavelet transform based compression of dose data is taken to that performed by Zakarian and Deasy. For the purpose of this research we define the term *compressibility* as *the ratio of the original dose data matrix size in bits / the number of bits describing the non-zero thresholded transform coefficients.* It should be noted that realistic compression ratios would be significantly lower as the zero entries of the dose matrix require a finite number of bits be used as placeholders.

From the resulting wavelet coefficient set, smaller values generally represent small-magnitude rough functions, likely to be either noise or negligible features of real dose distributions. With increasing coefficient size comes decreasing detail and representation of broader signal trends.

For the purpose of comparison with the work previously investigated [Zakarian and Deasy, 2004] two test cases have been used to investigate the compressibility of

the doselet data. In the first test a 6 MV beamlet (0.5 cm × 0.5 cm) was transported through a $100 \times 100 \times 100$ voxel watertank model with uniform pixel spacing of 0.2 cm (overall dimension of $20 \times 20 \times 20$ cm^2). In the MC simulation, 4×10^5 independent histories were transported into the watertank model. The beamlet was incident on the watertank at an angle of 45^o to avoid unrealistic compression results from a doselet parallel to the watertank's surface and therefore containing more zero dose voxels. Based on previous observations by Zakarian and Deasy, the compression of doselets from other energy beams or spectral combinations is not expected to vary significantly.

A second test case, a 6 MV beamlet (0.5 cm × 0.5 cm) was transported through a head phantom that had been constructed from a computed tomography (CT) data set. The CT phantom was identical to that used in previous work by Zakarian and Deasy. The pixel size (and consequently the dose matrix spacing) was $0.16 \times 0.16 \times 0.5$ cm^3 in a matrix size of $251 \times 149 \times 60$ pixels (voxels). In the MC simulation, 4×10^5 independent histories were transported into the CT head phantom model.

The software to perform the discrete wavelet transform (DWT) and inverse discrete wavelet transform (IDWT) of each doselet was coded by the author in the C++ programming language and makes use of QccPack [Fowler, 2000], an open-source library of routines for the quantization, compression and coding of data. Use of the open source library enabled the construction of a 3-D DWT. The method employed for each doselet is a follows:

(i) Perform the separable dyadic 3-D DWT of the three-dimensional signal which is represented as a volume V of *frames*, *rows*, and *columns* using wavelet W.

(ii) Repeat *(i)* on the low-low-low pass octave of volume V for nl decomposition levels.

(iii) Pass the result of *(ii)* through hard threshold filter T, replacing coefficients

below a defined cutoff with zeros. The total number of wavelet coefficients below the cutoff is stored as NC.

(iv) Perform a separable dyadic 3-D IDWT of the three-dimensional signal corresponding to that performed in *(i)* on thresholded volume V'.

(v) Repeat *(iv)* for nl decomposition levels.

(vi) Calculate the root mean square error restricted to dose values greater than 0.5 times maximum dose (RMSE $_{0.5}$) using the following formula

$$\mathrm{RMSE}_{0.5} = 100\% \times \sqrt{\frac{1}{N} \sum_{V<0.5} |V(i,j,k) - V'(i,j,k)|^2} \tag{6.4}$$

This restriction makes the RMSE metric insensitive to low-dose details which are therapeutically less important and is done to allow comparison with results previously published in the literature.

(vii) Calculate the maximum error from the original dose distribution restricted to dose values greater than 0.5 times maximum dose (MAXERR $_{0.5}$) using the following formula

$$\mathrm{MAXERR}_{0.5} = 100\% \times \mathrm{Max}\{|V(i,j,k) - V'(i,j,k)|\}_{V<0.5} \tag{6.5}$$

(viii) Calculate the *compressibility* (C) of the doselet in the following way

$$C = \frac{frames \times rows \times columns}{frames \times rows \times columns - NC} \tag{6.6}$$

To begin, an assessment of the 3-D MR decomposition and reconstruction algorithm defined above is performed without any thresholding (*i.e.* step *iii* of above). In this way an observation of any differences introduced from the transform operations

can be made.

To determine the dependence of compressibility on the number of dyadic decomposition levels, a series of 3-D MR decompositions and reconstructions were made using Haar, Coiflet 6, Daubechies 4, Daubechies 6 and Cohen-Daubechies-Feauveau 5-3 wavelets. The finite impulse response (FIR) sequences from the wavelets used are given in table 6.1. The effect of decomposition level (1, 2, 3, 4, 5, 6) and threshold values (0.5, 1.0, 1.5, 2.0) was observed in terms of the RMSE $_{0.5}$ and MAXERR $_{0.5}$ introduced into the reconstructed dose distributions.

Table 6.1: Finite impulse response (FIR) for wavelets used in QCCPack analysis [Fowler, 2000].

Wavelet	Filter	FIR Sequence					
Haar	Low	0.707107	0.707107				
	High	0.707107	-0.707107				
Coif 6	Low	-0.0156557	-0.0727326	0.384865	0.852572	0.337898	-0.0727326
	High	-0.0727326	-0.337898	0.852572	-0.384865	-0.0727326	0.0156557
Daub 4	Low	-0.12941	0.224144	0.836516	0.482963		
	High	0.482963	-0.836516	0.224144	0.12941		
Daub 6	Low	0.0352263	-0.0854413	-0.135011	0.459878	0.806892	0.332671
	High	0.332671	-0.806892	0.459878	0.135011	-0.0854413	-0.0352263
CDF 5-3	Low	1.06066	0.353553	-0.176777			
	High	-0.707107	0.353553				

To observe the effect of thresholding on the reconstructed doselet a subtraction of the original and reconstructed doselets was performed for the CT head phantom and watertank test cases.

6.3 Results

6.3.1 Selective simulation of the required beamlets

In Figure 6.4 (*top left*), a positional scatter plot of particle positions in a PSF scored at 55.0 cm from the isocenter with a secondary collimator size of 10×10 cm^2 is shown using the BEAMDP software package [Ma and Rogers, 2006]. In Figure 6.4 (*top right*) a beamlet grid of dimension 10×10 cm^2 with a grid spacing of 0.5×0.5 cm^2 has been used to index the PSF. From the resulting $400 + 1$ beamlets, particles beamlet #58 and beamlet #401 have been plotted.

A positional scatter plot of particle positions in a PSF scored at 73 cm from the isocenter is also presented in Figure 6.4 (*bottom left*). Figure 6.4 (*bottom right*) shows beamlet #1601 and six other random beamlets from the PSF that have been indexed using a 40×40 cm^2 beamlet grid with a grid spacing of 1.0 cm. Note, that beamlets #401 and #1601 represent phase-space particles positioned outside of the field size as defined by the secondary collimator.

6.3.2 Dose distributions from single field and from combined doselets

The PS beamlet method is verified by using MC dose distributions from a single 10×10 cm^2 field calculated in a vertical lung interface phantom. This distribution is compared with the sum of doselets derived from the same phase space. The importance of this type of self-consistency test has been emphasized by Jelen *et al.* [Jelen et al., 2005] in their work on analytical finite-size pencil beams. For this simulation, a PS is scored 55 cm from the isocenter as in Figure 6.4 (*top left*) and indexed as in Figure 6.4 (*top right*). The indexed PSF was then decomposed into 401 independent PSF's and simulated independently into the vertical water-lung interface phantom shown in Figure 6.5. In both cases, 2.5×10^8 particles were used from the PSF.

Figure 6.6 shows the resulting depth dose profile (left) and cross-plane profile (right) for both the standard MC simulation and the sum of all 401 doselets. These

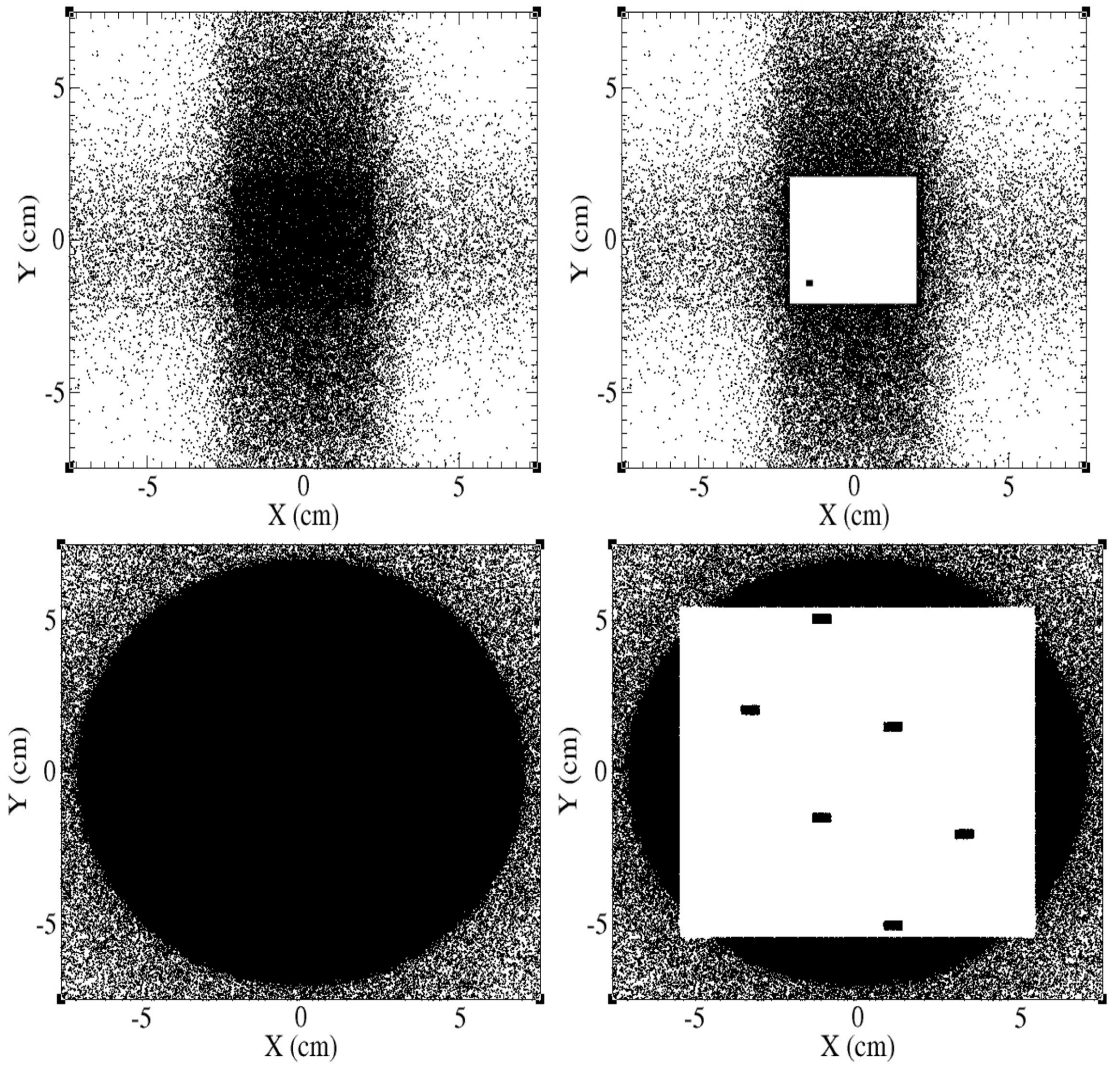

Figure 6.4: XY scatter plot of PS particle position at Z = 45.0 cm from the electron target (below the secondary collimator) for a 10 × 10 cm^2 collimated field (*top left*) and the same phase space showing only beamlet #58 and outer beamlet #401 (*top right*). Also included are XY scatter plots of a PS particle position above the secondary collimator at Z = 27.0 cm (*bottom left*) along with a plot of six random beamlets and outer beamlet #1601 from this PSF (*bottom right*).

profiles confirm that, as anticipated, the beamlet method can be successfully employed in regions of electronic disequilibrium, where non-MC algorithms tend to fail. A somewhat similar consistency check, performed in a water phantom without electronic disequilibrium, has also been performed by Bogner *et al.* [Bogner et al., 2006] for the purpose of studying segment and field size effects.

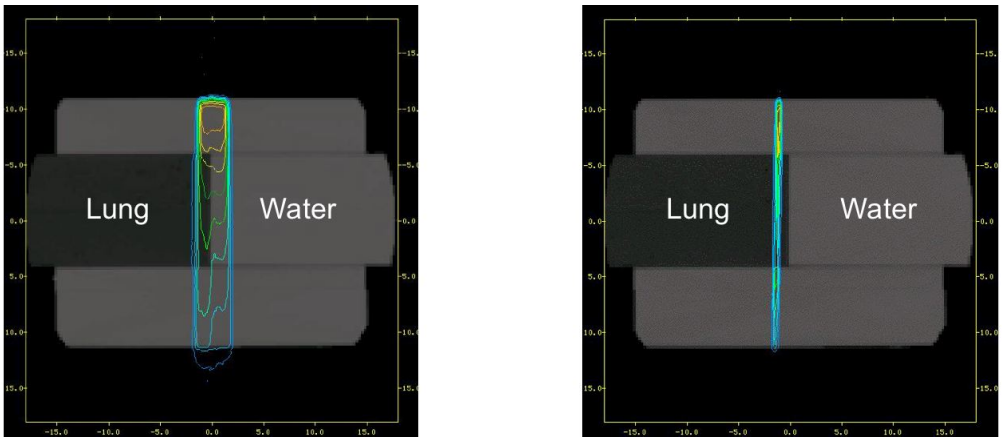

Figure 6.5: Monte Carlo dose distributions for a single field (left) placed with the beam axis along the interface between lung and normal tissue and for a single beamlet (right), which is part of the beam shown on the left.

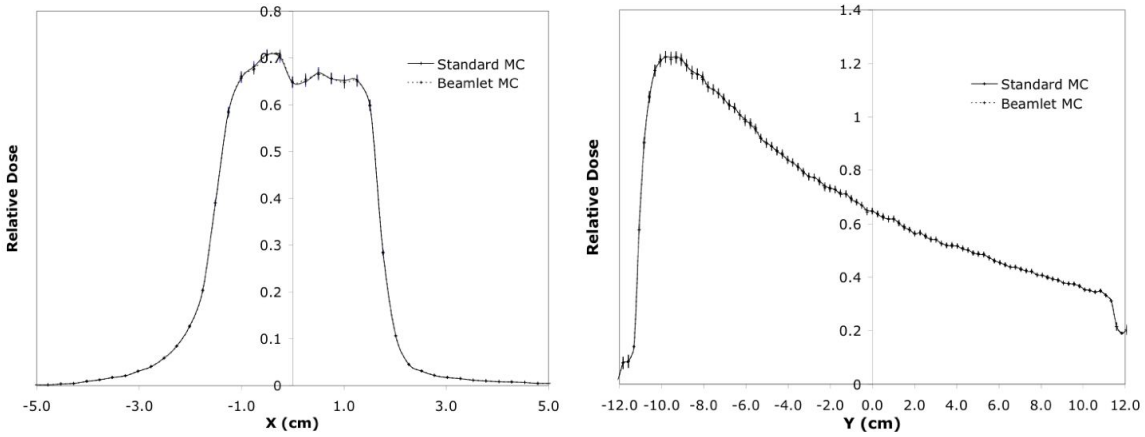

Figure 6.6: Lateral dose profiles (left) and depth dose profiles (right) for a single field calculated with standard MC (solid) and the corresponding set of doselets (dashed) incident on a vertical lung interface phantom. Each method simulated 2.5×10^8 particles.

In Figure 6.7 the dose profiles for an alternating bar pattern IMRT field are shown for both standard MC and beamlet simulations. Agreement of these dose distributions is within the statistical uncertainty of each simulation (1%), confirming application of the method to IMRT applications. Modulation of the field was performed using the method developed by Siebers *et al.* [Siebers et al., 2002].

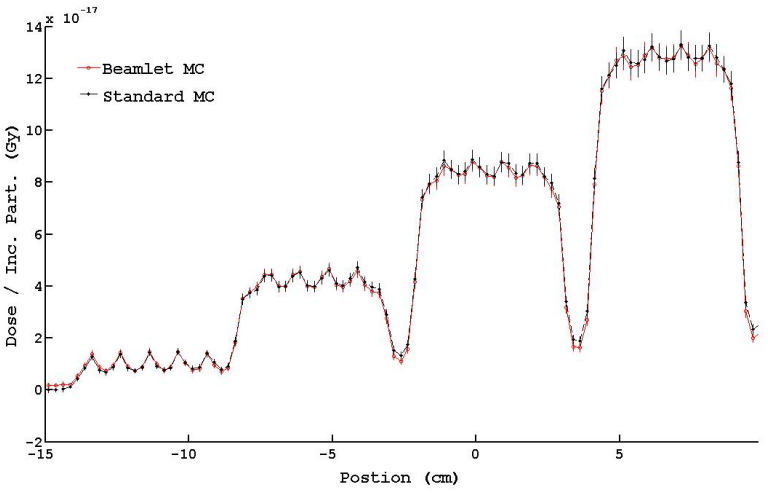

Figure 6.7: IMRT dose verification profile comparison of standard MC and beamlet simulations. In this figure, inter-leaf leakage is visible between the 4-bar MLC delivery patterns and is modeled within statistical agreement of the standard MC dose profile.

6.3.3 Doselet compressibility

The two doselet test cases used in the compressibility analysis are shown in Figure 6.8. On the left, a transverse slice of the dose matrix is shown fused onto the watertank CT density data. On the right, a transverse slice of the dose matrix is shown fused onto the head phantom CT density data. In all doselet figures the Osirix DICOM viewer [Rosset et al., 2004] was used to display the dose and CT data. For display purposes the dose has been normalized to a maximum dose of 65535, the largest binary number made from a 16 bit unsigned integer.

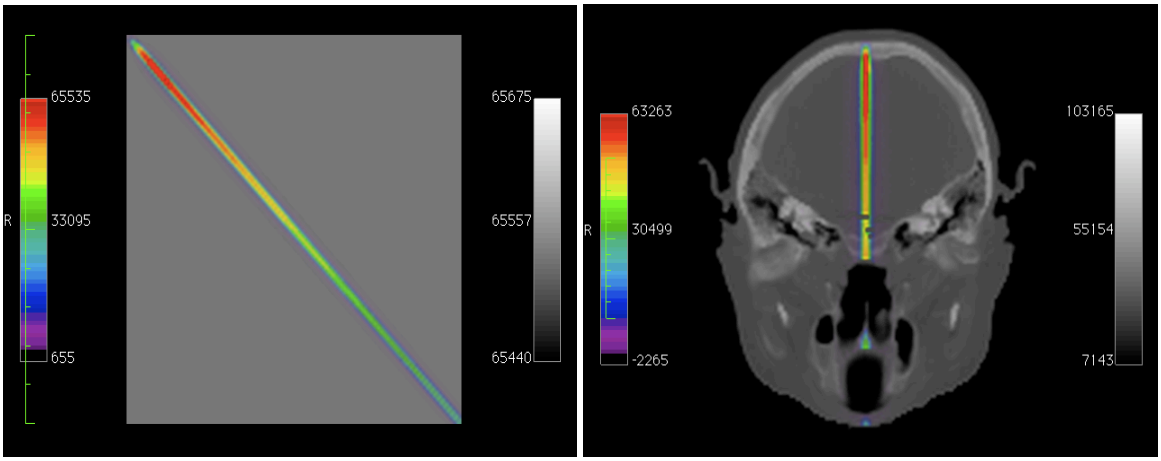

Figure 6.8: Doselet test cases for 3-D discrete wavelet transformation. A single doselet resulting from a beamlet incident at 45^o to a $100 \times 100 \times 100$ cm^3 watertank model *(left)*. A single doselet resulting from a beamlet incident on the posterior face of a head phantom reconstructed from CT data *(right)*.

In Figure 6.9, a low-dose window and level view ($> 0\%$ and $< 0.25\%$) of the head phantom doselet test case *(left)* and the same doselet after performing a 3-level 3-D dyadic multi-resolution decomposition followed by a 3-level 3-D dyadic reconstruction with orthogonal wavelets and symmetric boundary extension *(right)* are shown. These figures demonstrates the ability of the algorithm to accurately decompose and reconstruct the doselet (without thresholding) and not observe a significant loss of signal.

In Table 6.2 the RMSE $_{0.5}$, MAXERR $_{0.5}$, and compressibility ratios of the wa-

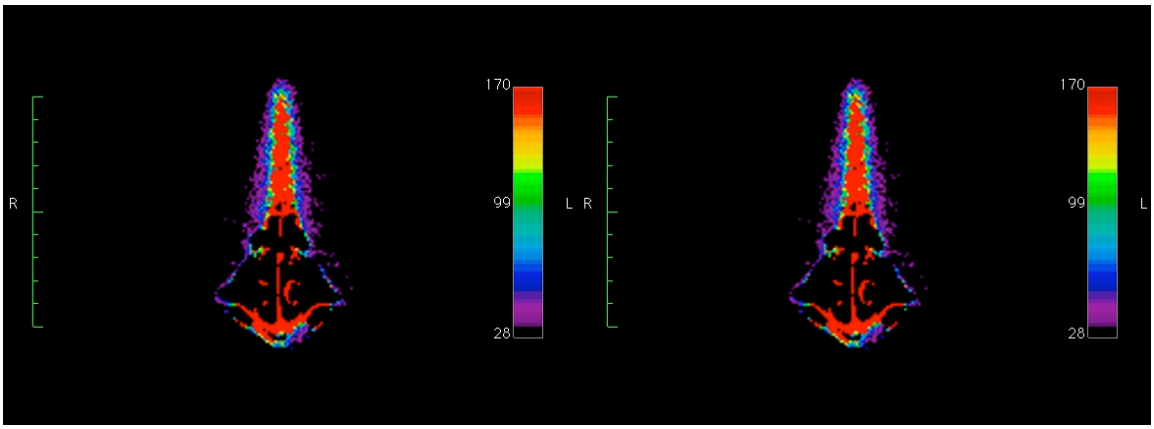

Figure 6.9: Low dose window and level view ($> 0\%$ and $< 0.25\%$) of the head phantom doselet test case *(left)* before and after performing a 3-level 3-D dyadic multi-resolution decomposition and corresponding reconstruction using orthogonal wavelets and symmetric boundary extension *(right)*. No thresholding was used in this example. (RMSE $_{0.5} = 4.8 \times 10^{-14}\%$)

tertank test case for a selection of threshold values are displayed for Haar, Coiflet 6, Daubechies 4, Daubechies 6 and Cohen-Daubechies-Feauveau 5-3 wavelets. The choice of these particular wavelets was made, in part, because they were included with the QccPack distribution. However, the wavelets used also provide tests for both orthogonal and biorthogonal wavelets as well as a commonly used wavelet in JPEG-2000 image compression (Cohen-Daubechies-Feauveau 5-3) [Taubman and Marcellin, 2001].

In Table 6.3 the RMSE $_{0.5}$, MAXERR $_{0.5}$ and compressibility ratios of the head phantom test case for a selection of threshold values are displayed for Haar, Coiflet 6, Daubechies 4, Daubechies 6 and Cohen-Daubechies-Feauveau 5-3 wavelets.

In Figure 6.10 *(left)* a low dose window and level view ($> 0\%$ and $< 2\%$) of the watertank doselet is shown. In Figure 6.10 *(middle)* the same doselet is shown after a 3-level MR decomposition, thresholding (1%), and reconstruction. The inherent noise reduction in the thresholding process is visible. In Figure 6.10 *(right)* a subtraction of the doselets is shown.

In Figure 6.11 *(left)* a transverse slice of the head phantom doselet is shown

Table 6.2: Doselet compressibility results for the $100 \times 100 \times 100$ voxel water tank phantom test case with varying decomposition levels and a hard threshold of 1%. A hard threshold of 1% implies that wavelets with coefcients less than or equal to 1% of the maximum wavelet coefcient are set to zero.

Wavelet	Threshold (%)	RMSE (%)	Maximum error (%)	Compressibility ratio
Haar	0.5	0.00224	0.512	96:1
	1.0	0.00471	0.945	140:1
	1.5	0.00650	1.460	178:1
	2.0	0.00880	2.347	219:1
Coiflet 6	0.5	0.00143	0.463	117:1
	1.0	0.00292	0.680	154:1
	1.5	0.00479	1.162	186:1
	2.0	0.00764	1.969	219:1
Daubechies 4	0.5	0.00131	0.362	115:1
	1.0	0.00290	0.731	154:1
	1.5	0.00445	1.250	180:1
	2.0	0.00755	1.763	206:1
Daubechies 6	0.5	0.00200	0.422	112:1
	1.0	0.00607	1.583	158:1
	1.5	0.0104	2.168	190:1
	2.0	0.0153	2.856	217:1
Coh-Daub-Feauv 5-3	0.5	0.00148	0.639	145:1
	1.0	0.00687	1.592	203:1
	1.5	0.0122	2.129	243:1
	2.0	0.0200	3.538	279:1

passing through the nasopharynx. In Figure 6.11 *(middle)* the same doselet is shown after a 3-level MR decomposition, thresholding (1%), and reconstruction. In Figure 6.11 *(right)* a subtraction of the doselets is shown.

In Figures 6.12, 6.13 and 6.14, the compressibility, RMSE $_{0.5}$ and MAXERR $_{0.5}$ dependence on decomposition level are shown for threshold values of 0.5%, 1.0%,

Table 6.3: Doselet compressibility results for human head CT phantom test case with varying decomposition levels and a hard threshold of 0.01.

Wavelet	Threshold (%)	RMSE (%)	Maximum error (%)	Compressibility ratio
Haar	0.5	0.00101	0.587	372:1
	1.0	0.00193	1.064	540:1
	1.5	0.00263	1.663	735:1
	2.0	0.00296	1.760	898:1
Coiflet 6	0.5	0.00081	0.633	336:1
	1.0	0.00154	1.126	524:1
	1.0	0.00211	1.697	693:1
	2.0	0.00282	2.174	828:1
Daubechies 4	0.5	0.00082	0.559	323:1
	1.0	0.00152	1.000	500:1
	1.5	0.00212	1.704	651:1
	2.0	0.00278	2.028	791:1
Daubechies 6	0.5	0.00094	0.655	286:1
	1.0	0.00144	1.188	443:1
	1.5	0.00173	1.567	567:1
	2.0	0.00237	1.857	691:1
Coh-Daub-Feauv 5-3	0.5	0.00094	0.655	367:1
	1.0	0.00144	1.188	592:1
	1.5	0.00173	1.567	766:1
	2.0	0.00237	1.857	924:1

1.5%, and 2.0%.

In Figure 6.15, the compressibility, $\text{RMSE}_{0.5}$ and $\text{MAXERR}_{0.5}$ dependence on the thresholding used is plotted for Haar, Daubechies-4 and Cohen-Daubechies-Feauveau-5-3 wavelets.

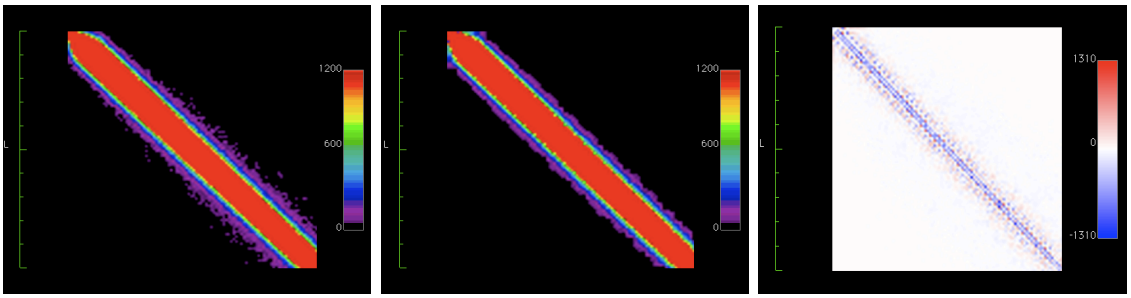

Figure 6.10: Hard threshold example of the watertank test doselet. A 3-level 3 dimensional dyadic multi-resolution decomposition was applied to the original doselet *(left)* with windowing and leveling adjusted to show <2% of the maximum dose) with a Haar wavelet. The resulting wavelet coefficients were thresholded below 1% and then the signal is reconstructed *(middle)*. A subtraction map showing dose differences is also shown *(right)* (RMSE $_{0.5}$ = 0.0029, MAXERR $_{0.5}$ = 0.73%).

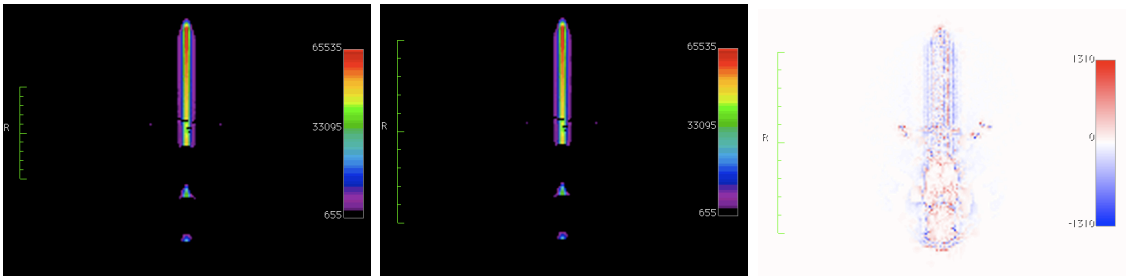

Figure 6.11: Hard threshold example of the head phantom test doselet. A 3-level 3-D dyadic discrete wavelet transform was applied to the original doselet *(left)* with the Cohen-Daubechies-Feauveau-5-3 wavelet. The resulting wavelet coefficients were thresholded below 1% and then the inverse wavelet transform is taken *(middle)*. A subtraction map showing up to ±2% differences from the thresholding is also shown *(right)* (RMSE $_{0.5}$ = 0.0014%, MAXERR $_{0.5}$ = 1.2%).

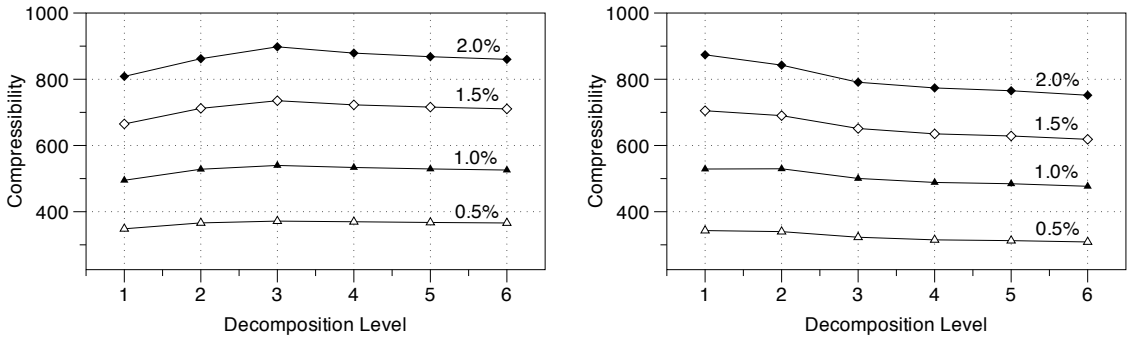

Figure 6.12: Compressibility achieved with varying number of decomposition levels and threshold values of 0.5%, 1.0%, 1.5%, 2.0% for Haar wavelets *(left)* and Daubechies-4 wavelets *(right)*.

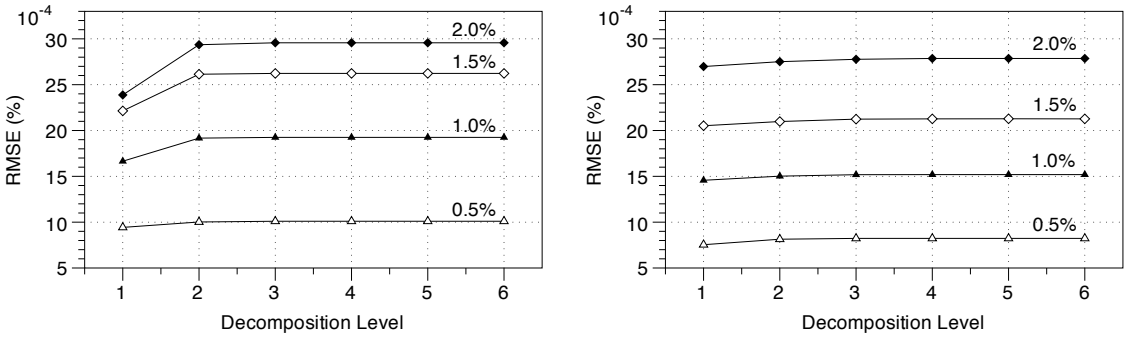

Figure 6.13: Root mean square error (RMSE) calculated with varying number of decomposition levels for threshold values of 0.5%, 1.0%, 1.5%, 2.0% for Haar wavelets *(left)* and Daubechies-4 wavelets *(right)*. In each case the RMSE was calculated with dose values greater than 50% of the maximum dose. This restriction makes the RMSE metric insensitive to low-dose details which are therapeutically less important.

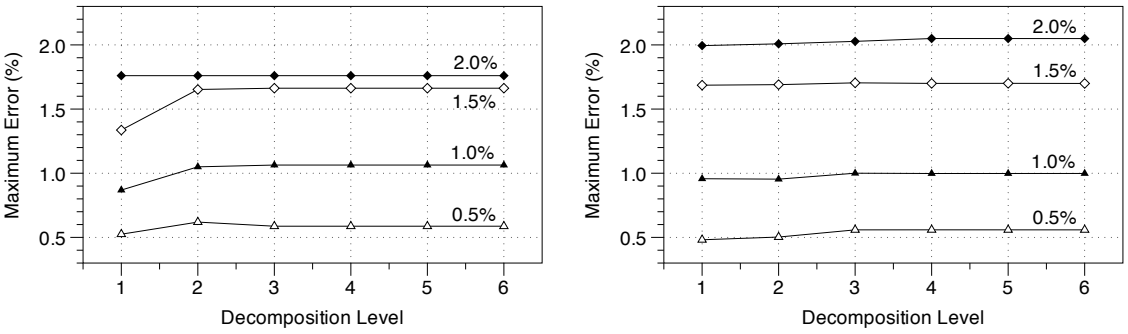

Figure 6.14: Maximum error (MAXERR) calculated with varying number of decomposition levels for threshold values of 0.5%, 1.0%, 1.5%, 2.0% for Haar wavelets *(left)* and Daubechies-4 wavelets *(right)*. In each case the MAXERR was calculated with dose values greater than 50% of the maximum dose. This restriction makes the MAXERR metric insensitive to low-dose details which are therapeutically less important.

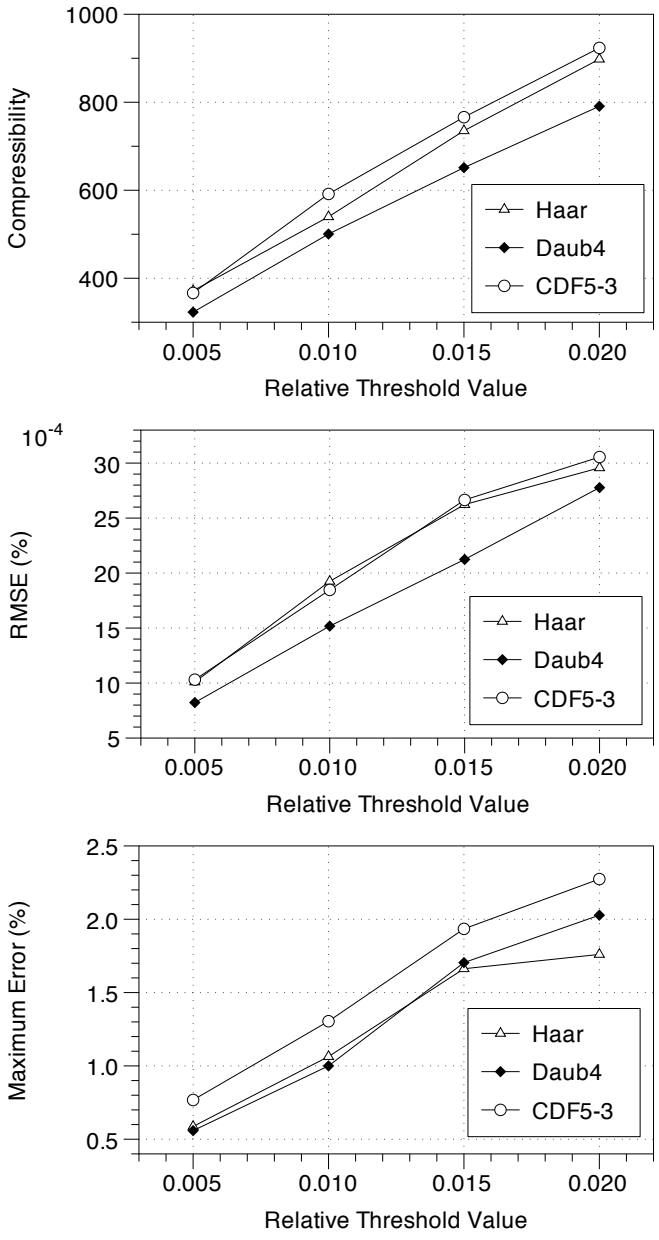

Figure 6.15: Compressibility, root mean square error (RMSE) and maximum error dependence on threshold value for Haar, Daubechies-4 and Cohen-Daubechies-Feauveau-5-3 wavelets. In each case the RMSE and MAXERR were calculated with dose values greater than 50% of the maximum dose.

6.4 Discussion and Conclusions

A method of generating phase space beamlets and resulting doselets has been developed and the compressibility of the dose matrix has been investigated with a 3-D multi-resolution decomposition technique. The method allows a phase space file (PSF) to be used for MC beamlet generation and doselet calculation. The method labels particles of a common beamlet by assigning each particle's LATCH variable to the given beamlet number. It should be noted that indexing the phase space with the LATCH variable is not absolutely required to create individual beamlet PSF's. However, by doing so the powerful features of particle tracking with the LATCH variable are maintained and this variable can be used to track every particle of a given beamlet through BEAMnrc or DOSXYZnrc simulations.

The use of MC methods to calculate beamlet dose distributions was previously deemed to be "exceedingly time consuming" for clinical application [Jelen et al., 2005]. However, the time required to obtain and run a set of MC beamlets using the presented method on a single CPU is slightly more than that of a standard MC simulation. Additional time is a result of sorting the PSF or extracting individual beamlet PSF's. With careful buffering during the writing of particles to the sorted PSF, the method sorts a typical PSF containing ∼5 million particles in roughly 8 seconds on a 2.2 GHz Pentium 4 processor with 1 GB of RAM.

The separation of a single phase space into beamlet phase spaces allows natural parallelization of the dose calculation across a computer network or multiple processor cores. The method currently makes use of the Condor High Throughput Computing software to distribute beamlet calculations across many computers. By doing so, the dose calculation times are greatly reduced below that of a standard MC simulation on a single PC.

The presented method employs the widely available open source MC codes BEAM-

nrc and DOSXYZnrc; it can therefore be easily adopted by any user of these codes. On the other hand the proposed method is flexible enough to allow the use of any MC dose scoring code accepting a phase space as input by eliminating the requirement that the dose scoring code have bit filtering capability. This was one of the motivations for choosing to sort the PSF prior to simulation over using a bit filter at the time of simulation. Another important motivation is that sorting the PSF drastically improves overall simulation efficiency by reducing the number of times the phase space file must be read from N+1 down to just 2. The gain in simulation efficiency boosts as the size of the PSF grows.

An alternative approach to the presented method is to make modifications to the MC dose scoring code to enable the scoring of dose from particles of the same LATCH beamlet number at the time of deposition in the phantom. A similar approach is presented by Bogner *et al.* [Bogner et al., 2006]. This approach has several disadvantages. First, there are large memory requirements to hold dose and uncertainty scoring arrays in RAM for a radiotherapy treatment field with N beamlets and M voxels. As treatments increase in complexity (dynamic arc therapies, Intensity modulated arc therapies, Tomotherapy [Mackie et al., 1993], 4-D IMRT) the number of beamlets continually increases and therefore memory requirements may become prohibitive. Second, access to the source code of the dose scoring routine is not always available.

Obvious applications for generating MC beamlets are in radiotherapy optimization. The beamlet technique has been successfully implemented in MC based inverse treatment planning using direct aperture optimization by Bergman *et al.* [Bergman et al., 2006]. It can be as easily utilized in fluence-based optimization of IMRT or conventional beam portals. In particular, the technique was utilized in optimizations of the open beam MC calculated profiles to match measured data [Bush and Popescu, 2005].

It is important to note that, for use in most fluence based optimization applications, the simulation of beamlets can be a one-off process [Zakarian and Deasy, 2004; Bergman et al., 2006; Bogner et al., 2006]. That is, once the set of all required doselets has been collected, calibrated and stored, the optimization process need not re-simulate beamlets. Treatment planning optimizations can be carried out by simply scaling the doselet contributions by a set of N beamlet weights.

Using a wavelet coefficient threshold of 1%, a maximum compressibility factor of 592 was achieved using a 3-level dyadic decomposition with Cohen-Daubechies-Feauveau-5-3 (biorthogonal) wavelet on the head phantom test case. The thresholding introduced a root mean square error (RMSE) of 0.0014% and maximum error of 1.18% on voxels containg dose greater than 50% of the maximum dose. In comparing these results with those obtained by Zakarian and Deasy [Zakarian and Deasy, 2004] with a 2-D decomposition technique (for the same 1% thresholding value on an identical phantom) a maximum compressibility factor of 50 in the transverse plane of the phantom and maximum compressibility factor of 84 in the sagittal plane were achieved. The RMSE was calculated to be 0.04% with a maximum error of 0.94% on voxels greater than 50% of the maximum dose. From the results of this group, the symlet-2 wavelet (orthogonal) was found to produce the greatest compressibility, albeit by a small amount over other wavelets.

From the results of this chapter on the head phantom test case, a maximum overall compressibility factor of 924 was achieved with the Cohen-Daubechies-Feauveau-5-3 wavelet, a 3-level decomposition and a threshold of 2%. The thresholding resulted in a RMSE = 0.00237% and maximum error = 1.86% on voxels containing greater than 50% of the maximum dose. The biorthogonal wavelet achieved the highest compressibility but also resulted in the highest RMSE and maximum error from thresholding.

The water tank test case yielded, in general, lower compressibility results than

the head phantom test case. This was a direct result of a smaller phantom, as well as the water tank phantom containing less air, and hence a larger fraction of voxels containing dose from the beamlet. A maximum compressibility factor of 203 with a RMSE = 0.00687% and maximum error = 1.59% was calculated on voxels greater than 50% of the maximum dose. Comparing the results to those found by Zakarian and Deasy with a 2-D decomposition, a maximum compressibility factor of 32 was found on a transverse slice and 82 on a sagittal slice (RMSE = 0.046%, maximum error = 0.91% on voxels greater than 50% of the maximum dose).

A comparison of the 3-D compressibility results with the 2-D compressibility results published by Zakarian and Deasy is difficult since the latter were performed on a single 2-D transverse slice and a single 2-D sagittal slice. An adaptive thresholding method was introduced to apply variable thresholding to different slices in the phantom depending on the slice position in the phantom. The adaptive thresholding scheme is only applicable to beamlets that are coplanar or near-coplanar to the voxel boundaries which severely limits the usefulness for any treatment planning use as beamlets are almost never coplanar with voxel boundaries. With 3-D decomposition such adaptive thresholding becomes unnecessary.

The ideal number of decomposition levels was found to depend of the choice of wavelet and the particular dose distribution. A decomposition level of 3 was found to be an optimal balance between compressibility and required CPU calculations for most wavelets tested. The time required to decompose the doselet was found to depend on the size of the dose matrix and was, in general, much less than the time required to buffer the matrix into RAM. For the water tank test doselet, the time required was approximately 0.1 second for both decomposition and reconstruction of the doselet on a Intel 2.4 GHz Core 2 Duo processor with sufficient RAM to buffer the dose matrices. Although highly efficient, the QccPack library could be further streamlined to reduce this computation time.

In this chapter, only the compressibility of the test dose matrices was investigated. Encoding of the transformed and thresholded data is required to achieve actual compression. Future research may include an investigation of optimal encoding schemes for fast decoding and reconstruction during the optimization. Future work may also include investigating methods of using the doselet in its decomposed form during the optimization. Avoiding the need for reconstruction may inevitably lead to faster optimization times.

Chapter 7

Final Conclusions

This dissertation has investigated techniques for the improvement and advancement of dose calculations in external beam radiotherapy using the Monte Carlo (MC) method. The purpose of this research is to further enable the use of MC dose calculation in both verification and planning of advanced external beam radiotherapy treatments such as intensity modulated radiation therapy (IMRT), and arc delivery techniques such as volumetric modulated radiation therapy (VMAT), RapidArc, and IMAT. The dissertation has covered a broad spectrum of topics from commissioning the Monte Carlo accelerator model, to reducing the variance from the use of phase spaces in the Monte Carlo simulations, to enabling the modeling of advanced radiotherapy treatments such as RapidArc for quality assurance purposes, to finally making the required steps toward using Monte Carlo dose calculation in the planning stages of these advanced radiotherapy treatments.

7.1 Dissertation Summary

To begin, a technique was developed to efficiently determine the optimal intensity distribution of the pre-target electron beam in a Monte Carlo (MC) accelerator model able to most accurately reproduce a set of measured photon field profiles for a given accelerator geometry and incident electron beam energy. A novel method has been developed in which an electron beam intensity distribution can be *inferred* allowing an accurate reproduction of measured dose distributions. The method has the ability to reduce the number of simulations required to commission a MC accelerator model and has achieved better agreement with measurement than other methods described in the literature. The method begins from a cylindrically symmetric pre-target electron beam (radius 0.5 cm) of uniform intensity. This beam is subdivided into annular regions of fluence for which each region is individually transported through the accelerator head and into a water phantom. A simulated annealing search is then performed to determine the optimal combination of weights of the annular fluences

that provide a best match between measured dose distributions and the weighted sum of annular dose distributions for a particular pre-target electron energy.

When restricted to Gaussian intensity distributions, the optimization yielded an optimal full-width-half-maximum (FWHM) = 1.34 mm for 18.0 MeV, with a root-mean square error (RMSE) = 0.49% on 40 × 40 cm^2 lateral profiles. When allowed to deviate from Gaussian intensities, a further reduction in RMSE was achieved. For our Clinac 21 EX accelerator MC model (based on the 1996 Varian Oncology Systems, Monte Carlo Project package) the optimal unrestricted intensity distribution was found to be a Gaussian-like solution (18.0 MeV, FWHM = 1.10 mm, 40 × 40 cm^2 profile RMSE = 0.15%) with the presence of an extra-focal halo contribution on the order of 10% of the maximum Gaussian intensity. Using the optimally derived intensity, 10 × 10 cm^2 and 4 × 4 cm^2 profiles were found to be in agreement with measurement with a maximum RMSE = 0.49%. The optimized Gaussian and unrestricted values of the electron beam FWHM were both within the range of those inferred by focal spot image measurements performed by Jaffray *et al*, 1993. The inference of an extra focal pre-target electron component may be an indicator of a deficiency in the MC model and requires further investigation.

It is well known that the use of a phase space in MC simulation introduces a baseline level of variance that cannot be suppressed through the use of standard particle recycling techniques. This variance (termed latent phase space variance by Sempau *et al*) [Sempau et al., 2001] can be a significant limiting factor in achieving accurate, low-uncertainty dose scoring results, especially near the surface of a phantom. A BEAMnrc component module (MCTWIST) was developed to reduce the presence of latent variance in phase space based Monte Carlo simulations by implementing azimuthal particle redistribution (APR). For each recycled use of a phase space particle a random rotation about the beam's central axis was applied, effectively utilizing the cylindrical symmetry of the particle fluence and thereby providing a more accurate

representation of the source. The MCTWIST module is unique in that no physical component was actually added to the accelerator geometry. Beam modifications were made by directly transforming particle characteristics outside of BEAMnrc/EGSnrc particle transport. Using MCTWIST, a theoretical reduction in latent phase space variance by more than a factor of 35 was demonstrated for a 10×10 cm^2 field, when compared to standard phase space particle recycling techniques. The reduction in latent variance enabled the achievement of dramatically smoother in-water dose profiles.

RapidArc radiotherapy technology from Varian Medical Systems is arguably one of the most complex delivery systems currently available, capable of achieving an entire intensity-modulated radiation therapy (IMRT) treatment in a single gantry rotation about the patient. Three dynamic parameters can be continuously varied to create IMRT dose distributions - the speed of rotation, beam shaping aperture, and delivery dose rate. Modeling of RapidArc technology was incorporated within the existing Vancouver Island Monte Carlo (VIMC) system. This process was named VIMC-Arc and it has become an efficient framework for verification of RapidArc treatment plans. VIMC-Arc is a fully automated system that constructs MC beam and patient models from a standard RapidArc Digital Imaging and Communications in Medicine (DICOM) dataset, simulates radiation transport, collects the resulting dose and converts the dose into DICOM format for import back into the treatment planning system (TPS). VIMC-Arc accommodates multiple arc IMRT deliveries and models gantry rotation as a series of segments with dynamic MLC motion within each segment. Several verification RapidArc plans were generated by the Eclipse TPS on a water-equivalent cylindrical phantom and re-calculated using VIMC-Arc. This includes one typical RapidArc plan, one plan for dual arc treatment, and one plan with avoidance sectors. One RapidArc plan was also calculated on a DICOM patient CT data set. Statistical uncertainty of MC simulations was kept within 1%.

VIMC-Arc produced dose distributions that matched very closely to those calculated by anisotropic analytical algorithm (AAA) that is used in Eclipse. All plans also demonstrated better than 1% agreement of the dose at the isocenter. This demonstrates the capabilities of the new MC system to model all dosimetric features required for RapidArc dose calculations.

As radiotherapy treatment planning moves towards MC based dose calculation methods, the MC beamlet is becoming an increasingly common optimization entity. Until now methods used to produce MC beamlets have utilized a particle source model (PSM) approach. In this work the implementation of a phase space based approach to MC beamlet generation was introduced with potential to provide greater accuracy in beamlet dose distributions. In the presented approach a standard BEAMnrc phase space was sorted and divided into beamlets with particles labeled using the inheritable particle history variable. This was achieved with the use of an efficient sorting algorithm, capable of sorting a phase space of any size into the required number of beamlets in only two passes. Sorting a phase space of five million particles was achieved in less than eight seconds on a single-core 2.2 GHz CPU. The beamlets were then transported separately into a patient CT data set, producing an independent set of dose distributions (doselets). Methods for doselet normalization and conversion of the absorbed dose to absolute units of Gy for use in IMRT plan optimization were also presented.

The storage of a large quantity of beamlet dose distributions sufficient for advanced radiotherapies such as VMAT, IMAT, or RapidArc poses a significant challenge to todays computer hardware. Data compression tailored specifically to the 3-D beamlet dose data matrices can significantly reduce the required quantity of data to be stored and or buffered into the treatment planning system's RAM for optimization. This dissertation has developed a 3-D dyadic multi-resolutional decomposition technique, using the discrete wavelet transform, for the purpose of data compression.

The compressibility of beamlet dose distributions has been investigated with respect to the wavelet used and number of decomposition levels. The 3-D decomposition technique has yielded greater compressibility when compared to a 2-D decomposition method developed by another research group and published in the literature [Zakarian and Deasy, 2004].

7.2 Future Work

There are several areas of future research that are a natural progression from the research presented in this dissertation and would like to be explored by the author. With respect to the research presented in Chapter 3 on *inferring the optimal pre-target electron beam parameters in a Monte Carlo virtual linac model*, future research may include investigating the use of alternative shaped fluences other than cylindrical annuli to allow the technique to be applied to accelerator models with non-cylindrical pre-target electron intensity distributions. In addition, the optimization technique may be applied in the commissioning of therapeutic electron beams.

The optimization of the 18 MV Varian Clinac 21EX accelerator as modeled, with the 1996 Varian Oncology Systems Monte Carlo Project package, yielded an optimal intensity distribution containing an extra-focal component peaked off-axis and on the order of 10% of the primary intensity peak. As demonstrated in Chapter 3, measurements of the focal spot performed with the beam passing through the flattening filter would detect the extra-focal component as a broad tail to the central intensity peak. Future work will include performing a measurement of the electron beam focal spot using a slit technique similar to that of Sham *et al* [Sham et al., 2008]. The measurement would ideally be performed with the flattening filter removed. An apparatus has been built and is currently being benchmarked within the BC Cancer Agency - Vancouver Island Center.

Future work with respect to the research presented in Chapter 5 on the *Monte*

Carlo modeling of arc radiotherapy delivery will include a Monte Carlo evaluation of RapidArc treatment plans for head and neck radiotherapy. A Vancouver Island radiotherapy (VIRAD) grant was recently received in part by the author (co-PI) to carry out this study. A first Monte Carlo evaluation of RapidArc dose calculations for oropharynx radiotherapy was recently published using the technique of Chapter 5 [Gagne et al., 2008].

Finally, future work with respect to the research presented in Chapter 6 on *Monte Carlo calculated beamlet dose distributions in advanced radiotherapy planning* will include the investigation of encoding schemes for beamlet dose compression. Techniques to introduce Monte Carlo dose calculation in the optimization of arc therapy planning using the fundamentals developed in Chapter 6 (phase space based beamlet generation and compression of the beamlet dose distributions) will also be investigated.

Bibliography

Aaronson, R. F., DeMarco, J. J., Chetty, I. J. and Solberg, T. D. [2002]. A Monte Carlo based phase space model for quality assurance of intensity modulated radiotherapy incorporating leaf specific characteristics, *Med Phys* **29**(12): 2952–8.

Al-Yahya, K., Verhaegen, F. and Seuntjens, J. [2007]. Design and dosimetry of a few leaf electron collimator for energy modulated electron therapy, *Med Phys* **34**(12): 4782–91.

Berger, M. J. and Hubbell, J. H. [1987]. Xcom: Photon cross sections on a personal computer, *Report NBSIR87-3597, NIST, Gaithersburg, MD, 20899* .

Bergman, A., Bush, K., Milette, M., Popescu, I., Otto, K. and Duzenli, C. [2006]. Direct aperture optimization for IMRT using Monte Carlo generated beamlets, *Med Phys* **33**(10): 3666–79.

Boge, R. J., Tolbert, D. D. and Edland, R. W. [1975]. Accessory beam flattening filter for the varian clinac-4 linear accelerator, *Radiology* **115**(2): 475–7.

Bogner, L., Hartmann, M., Rickhey, M. and Moravek, Z. [2006]. Application of an inverse kernel concept to Monte Carlo based IMRT, *Med Phys* **33**(12): 4749–4757.

Borcherds, P. [2000]. Importance sampling: an illustrative introduction, *Eur J Phys* **21**: 405–411.

Bortfeld, T. and Webb, S. [2008]. Single-Arc IMRT?, *Phys Med Biol* **54**(1): N9–N20.

Box, G. and Muller, M. [1958]. A note on the generation of random normal deviates, *Ann Math Statist* **29**(2): 610–611.

Boyer, A. L. and Yu, C. X. [1999]. Intensity-modulated radiation therapy with dynamic multileaf collimators, *Seminars in radiation oncology* **9**(1): 48–59.

Boyer, A. and Mok, E. [1985]. A photon dose distribution model employing convolution calculations, *Med Phys* **12**(2): 169–77.

Brahme, A. [1988]. Optimization of stationary and moving beam radiation therapy techniques, *Radiotherapy and Oncology* **12**(2): 129–40.

Bush, K. and Popescu, I. [2006]. *M.Sc. Thesis: The generation and application of monte carlo calculated beamlet dose distributions in radiation therapy*, University of Victoria.

Bush, K. and Popescu, T. [2005]. Po-Poster – 07: Commissioning of virtual linacs for Monte Carlo simulations by optimizing photon source characteristics, *Med Phys* **32**(7): 2411–2411.

Bush, K., Zavgorodni, S. and Beckham, W. [2007]. Azimuthal particle redistribution for the reduction of latent phase-space variance in Monte Carlo simulations, *Phys Med Biol* **52**(14): 4345–4360.

Cao, D., Holmes, T. W., Afghan, M. K. N. and Shepard, D. M. [2007]. Comparison of plan quality provided by intensity-modulated arc therapy and helical tomotherapy, *Int J Radiat Oncol Biol Phys* **69**(1): 240–50.

Cheng, J. C., Chao, K. S. and Low, D. [2001]. Comparison of intensity modulated radiation therapy (IMRT) treatment techniques for nasopharyngeal carcinoma, *Int J Cancer* **96**(2): 126–31.

Chetty, I., DeMarco, J. J. and Solberg, T. D. [2000]. A virtual source model for Monte Carlo modeling of arbitrary intensity distributions, *Med Phys* **27**(1): 166–72.

Chetty, I. J., Curran, B., Cygler, J. E., DeMarco, J. J., Ezzell, G., Faddegon, B. A., Kawrakow, I., Keall, P. J., Liu, H., Ma, C. M. C., Rogers, D. W. O., Seuntjens, J., Sheikh-Bagheri, D. and Siebers, J. V. [2007]. Report of the AAPM Task Group No. 105: issues associated with clinical implementation of Monte Carlo-based photon and electron external beam treatment planning, *Med Phys* **34**(12): 4818–53.

Chibani, O. and Ma, C. [2007]. On the discrepancies between Monte Carlo dose calculations and measurements for the 18 MV varian photon beam, *Med Phys* **34**(4): 1206–16.

Chow, J. C. L., Wong, E., Chen, J. Z. and Dyk, J. V. [2003]. Comparison of dose calculation algorithms with Monte Carlo methods for photon arcs, *Med Phys* **30**(10): 2686–94.

Chui, C. S. and Spirou, S. V. [2001]. Inverse planning algorithms for external beam radiation therapy, *Medical Dosimetry* **26**(2): 189–97.

Clivio, A., Fogliata, A., Franzetti-Pellanda, A., Nicolini, G., Vanetti, E., Wyttenbach, R. and Cozzi, L. [2009]. Volumetric-modulated arc radiotherapy for carcinomas of the anal canal: A treatment planning comparison with fixed field IMRT, *Radiotherapy and Oncology* (in press).

Constantinou, C. and Sternick, E. S. [1984]. Reduction of the "horns" observed on the beam profiles of a 6-MV linear accelerator, *Med Phys* **11**(6): 840–2.

Cozzi, L., Dinshaw, K. A., Shrivastava, S. K., Mahantshetty, U., Engineer, R., Deshpande, D. D., Jamema, S. V., Vanetti, E., Clivio, A., Nicolini, G. and Fogliata, A. [2008]. A treatment planning study comparing volumetric arc modulation with

RapidArc and fixed field IMRT for cervix uteri radiotherapy, *Radiotherapy and Oncology* **89**(2): 180–91.

Cranmer-Sargison, G., Beckham, W. and Popescu, I. [2004]. Modelling an extreme water-lung interface using a single pencil beam algorithm and the Monte Carlo method, *Phys Med Biol* **49**(8): 1557–67.

Cygler, J. E., Lochrin, C., Daskalov, G. M., Howard, M., Zohr, R., Esche, B., Eapen, L., Grimard, L. and Caudrelier, J. M. [2005]. Clinical use of a commercial Monte Carlo treatment planning system for electron beams, *Phys Med Biol* **50**(5): 1029–34.

Day, M. J. and Aird, E. G. A. [1996]. The equivalent field method for dose determinations in rectangular fields, Appendix A, Central Axis Depth Dose Data for Use in Radiotherapy, *British Journal or Radiology* (BRJ Supplement 25).

de Gersem, W., Wagter, C. D. and Neve, W. D. [2001]. An anatomy-based beam segmentation tool for intensity-modulated radiation therapy and its application to head-and-neck cancer, *Int J Radiat Oncol Biol Phys* **51**(3): 849–59.

de Smedt, B., Reynaert, N., Flachet, F., Coghe, M., Thompson, M. G., Paelinck, L., Pittomvils, G., de Wagter, C., de Neve, W. and Thierens, H. [2005]. Decoupling initial electron beam parameters for Monte Carlo photon beam modelling by removing beam-modifying filters from the beam path, *Phys Med Biol* **50**(24): 5935–51.

de Walle, J. V., Martens, C., Reynaert, N., Palmans, H., Coghe, M., Neve, W. D., Wagter, C. D. and Thierens, H. [2003]. Monte Carlo model of the Elekta SLiplus accelerator: validation of a new MLC component module in BEAM for a 6 MV beam, *Phys Med Biol* **48**(3): 371–85.

Deng, J., Jiang, S. B., Kapur, A., Li, J., Pawlicki, T. and Ma, C. M. [2000]. Photon

beam characterization and modelling for Monte Carlo treatment planning, *Phys Med Biol* **45**(2): 411–27.

Denny, M. [2001]. Introduction to importance sampling in rare-event simulations, *Eur J Phys* **22**: 403–411.

Ding, G. [2002]. Dose discrepancies between Monte Carlo calculations and measurements in the buildup region for a high-energy photon beam, *Med Phys* **29**(11): 2459–63.

Earl, M. A., Shepard, D. M., Naqvi, S., Li, X. A. and Yu, C. X. [2003]. Inverse planning for intensity-modulated arc therapy using direct aperture optimization, *Phys Med Biol* **48**(8): 1075–89.

Faddegon, B. A., Asai, M., Perl, J., Ross, C., Sempau, J., Tinslay, J. and Salvat, F. [2008]. Benchmarking of Monte Carlo simulation of bremsstrahlung from thick targets at radiotherapy energies, *Med Phys* **35**(10): 4308–17.

Faddegon, B. A. and Blevis, I. [2000]. Electron spectra derived from depth dose distributions, *Med Phys* **27**(3): 514–26.

Fippel, M. [1999]. Fast Monte Carlo dose calculation for photon beams based on the VMC electron algorithm, *Med Phys* **26**(8): 1466–75.

Fippel, M., Kawrakow, I. and Friedrich, K. [1997]. Electron beam dose calculations with the VMC algorithm and the verification data of the NCI working group, *Phys Med Biol* **42**(3): 501–20.

Fix, M. K., Keller, H., Rüegsegger, P. and Born, E. J. [2000]. Simple beam models for Monte Carlo photon beam dose calculations in radiotherapy, *Med Phys* **27**(12): 2739–47.

Fix, M. K., Stampanoni, M., Manser, P., Born, E. J., Mini, R. and Rüegsegger, P. [2001]. A multiple source model for 6 MV photon beam dose calculations using Monte Carlo, *Phys Med Biol* **46**(5): 1407–27.

Fix, M., Keall, P., Dawson, K. and Siebers, J. [2004]. Monte Carlo source model for photon beam radiotherapy: photon source characteristics, *Med Phys* **31**(11): 3106–21.

Flock, S. T. and Shragge, P. C. [1987]. A semianalytical method for the design of a linac x-ray beam flattening filter, *Med Phys* **14**(2): 202–9.

Fogliata, A., Clivio, A., Nicolini, G., Vanetti, E. and Cozzi, L. [2008]. Intensity modulation with photons for benign intracranial tumours: a planning comparison of volumetric single arc, helical arc and fixed gantry techniques, *Radiotherapy and Oncology* **89**(3): 254–62.

Fogliata, A., Nicolini, G., Vanetti, E., Clivio, A. and Cozzi, L. [2006]. Dosimetric validation of the anisotropic analytical algorithm for photon dose calculation: fundamental characterization in water, *Phys Med Biol* **51**(6): 1421–38.

Fogliata, A., Yartsev, S., Nicolini, G., Clivio, A., Vanetti, E., Wyttenbach, R., Bauman, G. and Cozzi, L. [2009]. On the performances of Intensity Modulated Protons, RapidArc and Helical Tomotherapy for selected paediatric cases, *Radiat Oncol* **4**(1): 2.

Fowler, J. [2000]. QccPack: An open-source software library for quantization, compression, and coding, *Applications of Digital Image Processing XXIII* .

Gagne, I. M., Ansbacher, W., Zavgorodni, S., Popescu, C. and Beckham, W. A. [2008]. A Monte Carlo evaluation of RapidArc dose calculations for oropharynx radiotherapy, *Phys Med Biol* **53**(24): 7167–85.

Gagné, I. M. and Zavgorodni, S. [2007]. Evaluation of the analytical anisotropic algorithm in an extreme water-lung interface phantom using Monte Carlo dose calculations, *J App Clin Med Phys* **8**(1): 33–46.

Gardner, J., Siebers, J. and Kawrakow, I. [2007]. Dose calculation validation of Vmc++ for photon beams, *Med Phys* **34**(5): 1809–18.

Gauer, T., Sokoll, J., Cremers, F., Harmansa, R., Luzzara, M. and Schmidt, R. [2008]. Characterization of an add-on multileaf collimator for electron beam therapy, *Phys Med Biol* **53**(4): 1071–85.

Gladwish, A., Oliver, M., Craig, J., Chen, J., Bauman, G., Fisher, B. and Wong, E. [2007]. Segmentation and leaf sequencing for intensity modulated arc therapy, *Med Phys* **34**(5): 1779–88.

Hasenbalg, F., Neuenschwander, H., Mini, R. and Born, E. J. [2007]. Collapsed cone convolution and analytical anisotropic algorithm dose calculations compared to VMC++ Monte Carlo simulations in clinical cases, *Phys Med Biol* **52**(13): 3679–91.

Heath, E. and Seuntjens, J. [2003]. Development and validation of a BEAMnrc component module for accurate Monte Carlo modelling of the Varian dynamic Millennium multileaf collimator, *Phys Med Biol* **48**(24): 4045–63.

Heath, E., Seuntjens, J. and Sheikh-Bagheri, D. [2004]. Dosimetric evaluation of the clinical implementation of the first commercial IMRT Monte Carlo treatment planning system at 6 MV, *Med Phys* **31**(10): 2771–9.

Huang, P. H., Chin, L. M. and Bjärngard, B. E. [1986]. Scattered photons produced by beam-modifying filters, *Med Phys* **13**(1): 57–63.

Huang, V. W., Seuntjens, J., Devic, S. and Verhaegen, F. [2005]. Experimental determination of electron source parameters for accurate Monte Carlo calculation of large field electron therapy, *Phys Med Biol* **50**(5): 779–86.

Hubbell, J. and Øverbø, I. [1979]. Relativistic atomic form factors and photon coherent scattering cross sections, *Journal of Physical and Chemical Reference Data* **8**(1): 69–106.

IMRT Collaborative Working Group [2001]. Intensity-modulated radiotherapy: current status and issues of interest, *Int J Radiat Oncol Biol Phys* **51**(4): 880–914.

Jaffray, D. A., Battista, J. J., Fenster, A. and Munro, P. [1993]. X-ray sources of medical linear accelerators: focal and extra-focal radiation, *Med Phys* **20**(5): 1417–27.

Jelen, U., Söhn, M. and Alber, M. [2005]. A finite size pencil beam for IMRT dose optimization, *Phys Med Biol* **50**(8): 1747–66.

Jeraj, R. and Keall, P. [1999]. Monte Carlo-based inverse treatment planning, *Phys Med Biol* **44**(8): 1885–96.

Jeraj, R. and Keall, P. [2000]. The effect of statistical uncertainty on inverse treatment planning based on Monte Carlo dose calculation, *Phys Med Biol* **45**(12): 3601–13.

Jeraj, R., Wu, C. and Mackie, T. [2003]. Optimizer convergence and local minima errors and their clinical importance, *Phys Med Biol* **48**(17): 2809–27.

Jin, L., Ma, C.-M., Fan, J., Eldib, A., Price, R. A., Chen, L., Wang, L., Chi, Z., Xu, Q., Sherif, M. and Li, J. S. [2008]. Dosimetric verification of modulated electron radiotherapy delivered using a photon multileaf collimator for intact breasts, *Phys Med Biol* **53**(21): 6009–25.

Johansen, S., Cozzi, L. and Olsen, D. [2009]. A planning comparison of dose patterns in organs at risk and predicted risk for radiation induced malignancy in the contralateral breast following radiation therapy of primary breast using conventional, IMRT and Volumetric modulated arc treatment techniques, *Acta Oncologica* pp. 1–10.

Johns, H. and Cunningham, J. [1983]. *The Physics of Radiology*, Charles C. Thomas Publisher.

Kahn, H. [1954]. Applications of Monte Carlo, *USAEC Report Number AECU-3259, The Rand Corporation* .

Karzmark, C. [1984]. Advances in linear accelerator design for radiotherapy, *Med Phys* **11**(2): 105–28.

Karzmark, C. J., Nunan, C. S. and Tanabe, E. [1992]. *Medical Electron Accelerators*, McGraw-Hill Companies Health Professions Division.

Kawrakow, I. and Bielajew, A. F. [1998]. On the representation of electron multiple elastic-scattering distributions for Monte Carlo calculations, *Nuc Instr Meth B* **134**: 325–336.

Kawrakow, I. and Fippel, M. [2000a]. Investigation of variance reduction techniques for Monte Carlo photon dose calculation using XVMC, *Phys Med Biol* **45**(8): 2163–83.

Kawrakow, I. and Fippel, M. [2000b]. VMC++, a fast MC algorithm for radiation treatment planning., *The Use of Computers in Radiotherapy, XIIIth Int'l Conf., Heidelberg* pp. 126–128.

Kawrakow, I., Fippel, M. and Friedrich, K. [1996]. 3D electron dose calculation using a Voxel based Monte Carlo algorithm (VMC), *Med Phys* **23**(4): 445–57.

Kawrakow, I. and Rogers, D. W. O. [2000]. The EGSnrc Code System: Monte Carlo simulation of electron and photon transport, *Technical Report PIRS-701, National Research Council of Canada* .

Kawrakow, I., Rogers, D. W. O. and Walters, B. R. B. [2004]. Large efficiency improvements in BEAMnrc using directional bremsstrahlung splitting, *Med Phys* **31**(10): 2883–98.

Keall, P. J., Siebers, J. V., Arnfield, M., Kim, J. O. and Mohan, R. [2001]. Monte Carlo dose calculations for dynamic IMRT treatments, *Phys Med Biol* **46**(4): 929–41.

Keall, P. J., Siebers, J. V., Libby, B. and Mohan, R. [2003]. Determining the incident electron fluence for Monte Carlo-based photon treatment planning using a standard measured data set, *Med Phys* **30**(4): 574–82.

Khan, F. M. [2003]. *The Physics of Radiation Therapy*, third edn, Lippincott Williams & Wilkins.

Kjaer-Kristoffersen, F., Ohlhues, L., Medin, J. and Korreman, S. [2009]. RapidArc volumetric modulated therapy planning for prostate cancer patients, *Acta Oncologica* **48**(2): 227–32.

Klein, E. E., Vicic, M., Ma, C.-M., Low, D. A. and Drzymala, R. E. [2008]. Validation of calculations for electrons modulated with conventional photon multileaf collimators, *Phys Med Biol* **53**(5): 1183–208.

Knoos, T., Ahnesjo, A., Nilsson, P. and Weber, L. [1995]. Limitations of a pencil beam approach to photon dose calculations in lung tissue, *Phys Med Biol* **40**(9): 1411–20.

Korreman, S., Medin, J. and Kjaer-Kristoffersen, F. [2009]. Dosimetric verification of RapidArc treatment delivery, *Acta Oncologica* **48**(2): 185–91.

Kry, S. F., Howell, R. M., Titt, U., Salehpour, M., Mohan, R. and Vassiliev, O. N. [2008]. Energy spectra, sources, and shielding considerations for neutrons generated by a flattening filter-free Clinac, *Med Phys* **35**(5): 1906–11.

Kry, S. F., Titt, U., Pönisch, F., Vassiliev, O. N., Salehpour, M., Gillin, M. and Mohan, R. [2007]. Reduced neutron production through use of a flattening-filter-free accelerator, *Int J Radiat Oncol Biol Phys* **68**(4): 1260–4.

Lane, R. G. and Paliwal, B. R. [1975]. Extended field treatment flatness filter for 4 MV linear accelerators, *Radiology* **115**(2): 478–9.

Larsen, R. D., Brown, L. H. and Bjärngard, B. E. [1978]. Calculations for beam-flattening filters for high-energy x-ray machines, *Med Phys* **5**(3): 215–20.

Lee, T. K., Rosen, I. I., Gibbons, J. P., Fields, R. S. and Hogstrom, K. R. [2008]. Helical tomotherapy for parotid gland tumors, *Int J Radiat Oncol Biol Phys* **70**(3): 883–91.

Li, X. A., Ma, L., Naqvi, S., Shih, R. and Yu, C. [2001]. Monte Carlo dose verification for intensity-modulated arc therapy, *Phys Med Biol* **46**(9): 2269–82.

Lindsay, P., Naqa, I. E., Hope, A., Vicic, M., Cui, J., Bradley, J. and Deasy, J. [2007]. Retrospective monte carlo dose calculations with limited beam weight information, *Med Phys* **34**(1): 334–46.

Ling, C. C., Zhang, P., Archambault, Y., Bocanek, J., Tang, G. and Losasso, T. [2008]. Commissioning and quality assurance of RapidArc radiotherapy delivery system, *Int J Radiat Oncol Biol Phys* **72**(2): 575–81.

Liu, H. H., Verhaegen, F. and Dong, L. [2001]. A method of simulating dynamic multileaf collimators using Monte Carlo techniques for intensity-modulated radiation therapy, *Phys Med Biol* **46**(9): 2283–98.

Llacer, J., Deasy, J., Portfeld, T., Solberg, T. and Promberger, C. [2003]. Absence of multiple local minima effects in intensity modulated optimization with dose-volume constraints, *Phys Med Biol* **48**(2): 183–210.

Locke, C. and Zavgorodni, S. [2008]. Vega library for processing DICOM data required in Monte Carlo verification of radiotherapy treatment plans, *Australasian physical & engineering sciences in medicine* **31**(4): 290–9.

Loewenthal, E., Loewinger, E., Bar-Avraham, E. and Barnea, G. [1992]. Measurement of the source size of a 6- and 18-MV radiotherapy linac, *Med Phys* **19**(3): 687–90.

LoSasso, T., Chui, C. and Ling, C. [1998]. Physical and dosimetric aspects of a multileaf collimation system used in the dynamic mode for implementing intensity modulated radiotherapy, *Med Phys* **25**(10): 1919–27.

Lutz, W. R., Maleki, N. and Bjärngard, B. E. [1988]. Evaluation of a beam-spot camera for megavoltage x rays, *Med Phys* **15**(4): 614–7.

Ma, C. M. [1998]. Characterization of computer simulated radiotherapy beams for Monte-Carlo treatment planning, *Radiation Physics and Chemistry* **53**: 329–344.

Ma, C. M., Faddegon, B. A., Rogers, D. W. and Mackie, T. R. [1997]. Accurate characterization of Monte Carlo calculated electron beams for radiotherapy, *Med Phys* **24**(3): 401–16.

Ma, C. M., Li, J. S., Pawlicki, T., Jiang, S. B., Deng, J., Lee, M. C., Koumrian, T., Luxton, M. and Brain, S. [2002]. A Monte Carlo dose calculation tool for radiotherapy treatment planning, *Phys Med Biol* **47**(10): 1671–89.

Ma, C. M., Mok, E., Kapur, A., Pawlicki, T., Findley, D., Brain, S., Forster, K. and

Boyer, A. L. [1999]. Clinical implementation of a Monte Carlo treatment planning system, *Med Phys* **26**(10): 2133–43.

Ma, C. M., Pawlicki, T., Jiang, S. B., Li, J. S., Deng, J., Mok, E., Kapur, A., Xing, L., Ma, L. and Boyer, A. L. [2000]. Monte Carlo verification of IMRT dose distributions from a commercial treatment planning optimization system, *Phys Med Biol* **45**(9): 2483–95.

Ma, C. M. and Rogers, D. W. O. [1995]. PIRS-0509C: Beam Characterization: a Multiple-Source Model, *National Research Council of Canada Report* .

Ma, C. M. and Rogers, D. W. O. [2006]. BEAMDP User Manual, *National Research Council of Canada Report* .

Mackie, T., Holmes, T., Swerdloff, S., Reckwerdt, P., Deasy, J., Yang, J., Paliwal, B. and Kinsella, T. [1993]. Tomotherapy: a new concept for the delivery of dynamic conformal radiotherapy, *Med Phys* **20**(6): 1709–19.

Mackie, T., Scrimger, J. and Battista, J. [1985]. A convolution method of calculating dose for 15-MV x rays, *Med Phys* **12**(2): 188–96.

Mallat, S. [2008]. *A Wavelet Tour of Signal Processing*, third edn, Academic Press.

Marsaglia, G. and Tsang, W. [2000]. The ziggurat method for generating random variables, *Journal of Statistical Software* .

Mavroidis, P., Ferreira, B. C., Shi, C., Lind, B. K. and Papanikolaou, N. [2007]. Treatment plan comparison between helical tomotherapy and MLC-based IMRT using radiobiological measures, *Phys Med Biol* **52**(13): 3817–36.

McEwen, M. R., Kawrakow, I. and Ross, C. K. [2008]. The effective point of measurement of ionization chambers and the build-up anomaly in MV x-ray beams, *Med Phys* **35**(3): 950.

McIntosh, A., Read, P. W., Khandelwal, S. R., Arthur, D. W., Turner, A. B., Ruchala, K. J., Olivera, G. H., Jeswani, S. and Sheng, K. [2008]. Evaluation of coplanar partial left breast irradiation using tomotherapy-based topotherapy, *Int J Radiat Oncol Biol Phys* **71**(2): 603–10.

Mesbahi, A. [2007]. Dosimetric characteristics of unflattened 6 MV photon beams of a clinical linear accelerator: a Monte Carlo study, *Applied Radiation and Isotopes* **65**(9): 1029–36.

Mesbahi, A., Mehnati, P., Keshtkar, A. and Farajollahi, A. [2007]. Dosimetric properties of a flattening filter-free 6-MV photon beam: a Monte Carlo study, *Radiation medicine* **25**(7): 315–24.

Mesbahi, A. and Nejad, F. S. [2008]. Monte Carlo study on a flattening filter-free 18-MV photon beam of a medical linear accelerator, *Radiation medicine* **26**(6): 331–6.

Metcalfe, P., Kron, T. and Hoban, P. [2007]. *The Physics of Radiotherapy X-Rays and Electrons*, Medical Physics Publishing Corporation.

Mihaylov, I. B. and Siebers, J. V. [2008]. Evaluation of dose prediction errors and optimization convergence errors of deliverable-based head-and-neck IMRT plans computed with a superposition/convolution dose algorithm, *Med Phys* **35**(8): 3722–7.

Mohan, R., Chui, C. and Lidofsky, L. [1985]. Energy and angular distributions of photons from medical linear accelerators, *Med Phys* **12**(5): 592–97.

Mohan, R., Chui, C. and Lidofsky, L. [1986]. Differential pencil beam dose computation model for photons, *Med Phys* **13**(1): 64–73.

Mohan, R. and Chui, C. S. [1987]. Use of fast Fourier transforms in calculating dose

distributions for irregularly shaped fields for three-dimensional treatment planning, *Med Phys* **14**(1): 70–7.

Motz, J., Olsen, H. A. and Koch, H. W. [1969]. Pair production by photons, *Rev Mod Phys* **41**(4): 581–639.

Munro, P., Rawlinson, J. A. and Fenster, A. [1988]. Therapy imaging: source sizes of radiotherapy beams, *Med Phys* **15**(4): 517–24.

Muzik, J., Soukup, M. and Alber, M. [2008]. Comparison of fixed-beam IMRT, helical tomotherapy, and IMPT for selected cases, *Med Phys* **35**(4): 1580–92.

NCIC [2009]. Canadian Cancer Statistics, pp. 1–110.

Nelson, W., Hirayama, H. and Rogers, D. [1985]. The EGS4 Code System, *SLAC-265* .

Nicolini, G., Vanetti, E., Clivio, A., Fogliata, A., Korreman, S., Bocanek, J. and Cozzi, L. [2008]. The GLAaS algorithm for portal dosimetry and quality assurance of RapidArc, an intensity modulated rotational therapy, *Radiat Oncol* **3**: 24.

Nordell, B. and Brahme, A. [1984]. Angular distribution and yield from bremsstrahlung targets (for radiation therapy), *Phys Med Biol* **29**(7): 797–810.

Otto, K. [2008]. Volumetric modulated arc therapy: IMRT in a single gantry arc, *Med Phys* **35**(1): 310–7.

Palma, D., Vollans, E., James, K., Nakano, S., Moiseenko, V., Shaffer, R., McKenzie, M., Morris, J. and Otto, K. [2008]. Volumetric Modulated Arc Therapy for Delivery of Prostate Radiotherapy: Comparison with Intensity-Modulated Radiotherapy and Three-Dimensional Conformal Radiotherapy, *Int J Radiat Oncol Biol Phys* **72**(4): 996–1001.

Pemler, P., Besserer, J., Schneider, U. and Neuenschwander, H. [2006]. Evaluation of a commercial electron treatment planning system based on Monte Carlo techniques (eMC), *Zeitschrift für medizinische Physik* **16**(4): 313–29.

Peñagarícano, J. A. [2006]. Step-and-shoot IMRT vs. helical tomotherapy: in regard to van Vulpen et al., *Int J Radiat Oncol Biol Phys* **64**(1): 328.

Podgorsak, E. B., Rawlinson, J. A. and Johns, H. E. [1974]. Design of x-ray targets for high energy accelerators in radiotherapy, *American Journal of Roentgenology* **121**: 873–882.

Podgorsak, E., Rawlinson, J. A. and Johns, H. E. [1975]. X-Ray depth doses from linear accelerators in the energy range from 10 to 32 MeV, *American Journal of Roentgenology* **123**: 182–191.

Popescu, I., Shaw, C., Zavgorodni, S. and Beckham, W. [2005]. Absolute dose calculations for Monte Carlo simulations of radiotherapy beams, *Phys Med Biol* **50**(14): 3375–92.

Que, W. [1999]. Comparison of algorithms for multileaf collimator field segmentation, *Med Phys* **26**(11): 2390–6.

Reinstein, L. E. and Orton, C. [1981]. "Horns" on a 6 MeV linear accelerator, *Int J Radiat Oncol Biol Phys* **7**: 111–113.

Ribberfors, R. [1975]. Relationship of the relativistic Compton cross section to the momentum distribution of bound electron states., *Phys Rev B* **12**(8): 3136–41.

Ries, L., Melbert, D., Krapcho, M., Stinchcomb, D., Howlader, N., Horner, M., Mariotto, A., Miller, B., Feuer, E., Altekruse, S., Lewis, D., Clegg, L. and Eisner, M. [2007]. SEER Cancer Statistics Review, 1975-2005, *National Cancer Institute* .

Robert, C. and Casella, G. [2005]. *Monte Carlo Statistical Methods*, second edn, Springer.

Rogers, D. [2002]. Monte Carlo Techniques in Radiotherapy, *Physics in Canada* .

Rogers, D., Faddegon, B., Ding, G., Ma, C., We, J. and Mackie, T. [1995]. BEAM: a Monte Carlo code to simulate radiotherapy treatment units, *Med Phys* **22**(5): 503–24.

Rogers, D., Walters, B. and Kawrakow, I. [2006]. PIRS-0509(A) rev K, *National Research Counsil of Canada Report* .

Rosset, A., Spadola, L. and Ratib, O. [2004]. OsiriX: an open-source software for navigating in multidimensional DICOM images, *Journal of Digital Imaging* **17**(3): 205–16.

Sauter, F. [1931]. Uber den atomaren Photoeffekt in der K-Schale nach der relativistischen Wellenmechanik Diracs, *Annalen der Physik* **11**: 454–88.

Scott, A. J. D., Nahum, A. E. and Fenwick, J. D. [2009]. Monte Carlo modeling of small photon fields: Quantifying the impact of focal spot size on source occlusion and output factors, and exploring miniphantom design for small-field measurements, *Med Phys* **36**(7): 3132.

Sempau, J., Sanchez-Reyes, A., Salvat, F., ben Tahar, H., Jiang, S. and Fernandez-Varea, J. [2001]. Monte Carlo simulation of electron beams from an accelerator head using PENELOPE, *Phys Med Biol* **46**(4): 1163–86.

Sham, E., Seuntjens, J., Devic, S. and Podgorsak, E. B. [2008]. Influence of focal spot on characteristics of very small diameter radiosurgical beams, *Med Phys* **35**(7): 3317–30.

Sheikh-Bagheri, D. and Rogers, D. [2002a]. Monte Carlo calculation of nine megavoltage photon beam spectra using the BEAM code, *Med Phys* **29**(3): 391–402.

Sheikh-Bagheri, D. and Rogers, D. [2002b]. Sensitivity of megavoltage photon beam Monte Carlo simulations to electron beam and other parameters, *Med Phys* **29**(3): 379–90.

Sheng, K., Molloy, J. A., Larner, J. M. and Read, P. W. [2007]. A dosimetric comparison of non-coplanar IMRT versus Helical Tomotherapy for nasal cavity and paranasal sinus cancer, *Radiotherapy and Oncology* **82**(2): 174–8.

Shepard, D. M., Cao, D., Afghan, M. K. N. and Earl, M. A. [2007]. An arc-sequencing algorithm for intensity modulated arc therapy, *Med Phys* **34**(2): 464–70.

Shepard, D. M., Earl, M. A., Li, X. A., Naqvi, S. and Yu, C. [2002]. Direct aperture optimization: a turnkey solution for step-and-shoot IMRT, *Med Phys* **29**(6): 1007–18.

Siantar, C. L. H., Walling, R. S., Daly, T. P., Faddegon, B., Albright, N., Bergstrom, P., Bielajew, A. F., Chuang, C., Garrett, D., House, R. K., Knapp, D., Wieczorek, D. J. and Verhey, L. J. [2001]. Description and dosimetric verification of the PEREGRINE Monte Carlo dose calculation system for photon beams incident on a water phantom, *Med Phys* **28**(7): 1322–37.

Siebers, J. V., Keall, P. J., Kim, J. O. and Mohan, R. [2002]. A method for photon beam Monte Carlo multileaf collimator particle transport, *Phys Med Biol* **47**(17): 3225–49.

Siebers, J. V., Keall, P. J., Nahum, A. E. and Mohan, R. [2000]. Converting absorbed dose to medium to absorbed dose to water for Monte Carlo based photon beam dose calculations, *Phys Med Biol* **45**(4): 983–95.

Sobol, I. M. [1974]. *The Monte Carlo Method*, University of Chicago Press.

Solberg, T. D., DeMarco, J. J., Holly, F. E., Smathers, J. B. and DeSalles, A. A. [1998]. Monte Carlo treatment planning for stereotactic radiosurgery, *Radiotherapy and Oncology* **49**(1): 73–84.

Spezi, E., Lewis, D. G. and Smith, C. W. [2002]. A DICOM-RT-based toolbox for the evaluation and verification of radiotherapy plans, *Phys Med Biol* **47**(23): 4223–32.

Stapleton, S., Zavgorodni, S., Popescu, I. A. and Beckham, W. A. [2005]. Implementation of random set-up errors in Monte Carlo calculated dynamic IMRT treatment plans, *Phys Med Biol* **50**(3): 429–39.

Sterpin, E., Salvat, F., Cravens, R., Ruchala, K., Olivera, G. H. and Vynckier, S. [2008]. Monte Carlo simulation of helical tomotherapy with PENELOPE, *Phys Med Biol* **53**(8): 2161–80.

Sterpin, E., Tomsej, M., Smedt, B. D., Reynaert, N. and Vynckier, S. [2007]. Monte carlo evaluation of the AAA treatment planning algorithm in a heterogeneous multilayer phantom and IMRT clinical treatments for an Elekta SL25 linear accelerator, *Med Phys* **34**(5): 1665–77.

Storm, E. and Israel, H. [1970]. Photon cross sections from 1 keV to 100 MeV for elements Z= 1 to Z= 100, *Nucl Data Sect* **7**: 565–681.

Taubman, D. and Marcellin, M. [2001]. *JPEG2000: Image Compression Fundamentals, Standards and Practice*, second edn, Springer.

Taumann, L. [1981]. The treatment head design for medical linear accelerators, *IEEE Transactions on Nuclear Science* **28**: 1893–1898.

Thain, D., Tannenbaum, T. and Livny, M. [2005]. Distributed computing in practice:

The Condor experience, *Concurrency and Computation: Practice and Experience* **17**(2-4): 323–356.

Thebaut, J. and Zavgorodni, S. [2006]. Coordinate transformations for BEAM/EGSnrc Monte Carlo dose calculations of non-coplanar fields received from a DICOM-compliant treatment planning system, *Phys Med Biol* **51**(23): N441–9.

Thieke, C., Nill, S., Oelfke, U. and Bortfeld, T. [2002]. Acceleration of intensity-modulated radiotherapy dose calculation by importance sampling of the calculation matrices, *Med Phys* **29**(5): 676–81.

Titt, U., Vassiliev, O. N., Pönisch, F., Dong, L., Liu, H. and Mohan, R. [2006]. A flattening filter free photon treatment concept evaluation with Monte Carlo, *Med Phys* **33**(6): 1595–602.

Titt, U., Vassiliev, O. N., Pönisch, F., Kry, S. F. and Mohan, R. [2006]. Monte Carlo study of backscatter in a flattening filter free clinical accelerator, *Med Phys* **33**(9): 3270–3.

Tonkopi, E., McEwen, M. R., Walters, B. R. B. and Kawrakow, I. [2005]. Influence of ion chamber response on in-air profile measurements in megavoltage photon beams, *Med Phys* **32**(9): 2918–27.

Tyagi, N., Martin, W., Du, J., Bielajew, A. and Chetty, I. [2006]. A proposed alternative to phase-space recycling using the adaptive kernel density estimator method, *Med Phys* **33**(2): 553–60.

Tyagi, N., Moran, J. M., Litzenberg, D. W., Bielajew, A. F., Fraass, B. A. and Chetty, I. J. [2007]. Experimental verification of a Monte Carlo-based MLC simulation model for IMRT dose calculation, *Med Phys* **34**(2): 651–63.

Tzedakis, A., Damilakis, J. E., Mazonakis, M., Stratakis, J., Varveris, H. and Gourtsoyiannis, N. [2004]. Influence of initial electron beam parameters on Monte Carlo calculated absorbed dose distributions for radiotherapy photon beams, *Med Phys* **31**(4): 907–13.

Ulmer, W., Pyyry, J. and Kaissl, W. [2005]. A 3D photon superposition/convolution algorithm and its foundation on results of Monte Carlo calculations, *Phys Med Biol* **50**(8): 1767–90.

Van Vulpen, M., Field, C., Raaijmakers, C. P. J., Parliament, M. B., Terhaard, C. H. J., MacKenzie, M. A., Scrimger, R., Lagendijk, J. J. W. and Fallone, B. G. [2005]. Comparing step-and-shoot IMRT with dynamic helical tomotherapy IMRT plans for head-and-neck cancer, *Int J Radiat Oncol Biol Phys* **62**(5): 1535–9.

Vanderstraeten, B., Olteanu, A. M. L., Reynaert, N., Leal, A., Neve, W. D. and Thierens, H. [2007]. Evaluation of uncertainty-based stopping criteria for monte carlo calculations of intensity-modulated radiotherapy and arc therapy patient dose distributions, *Int J Radiat Oncol Biol Phys* **69**(2): 628–37.

Vanderstraeten, B., Reynaert, N., Paelinck, L., Madani, I., Wagter, C. D., Gersem, W. D., Neve, W. D. and Thierens, H. [2006]. Accuracy of patient dose calculation for lung IMRT: A comparison of Monte Carlo, convolution/superposition, and pencil beam computations, *Med Phys* **33**(9): 3149–58.

Vanetti, E., Clivio, A., Nicolini, G., Fogliata, A., Ghosh-Laskar, S., Agarwal, J., Upreti, R., Budrukkar, A., Murthy, V., Deshpande, D., Shrivastava, S., Dinshaw, K. and Cozzi, L. [2009]. Volumetric modulated arc radiotherapy for carcinomas of the oro-pharynx, hypo-pharynx and larynx: A treatment planning comparison with fixed field IMRT, *Radiotherapy and Oncology (in print)* .

Vassiliev, O. N., Titt, U., Kry, S. F., Mohan, R. and Gillin, M. T. [2007]. Radiation

safety survey on a flattening filter-free medical accelerator, *Radiation protection dosimetry* **124**(2): 187–90.

Vassiliev, O. N., Titt, U., Pönisch, F., Kry, S. F., Mohan, R. and Gillin, M. T. [2006]. Dosimetric properties of photon beams from a flattening filter free clinical accelerator, *Phys Med Biol* **51**(7): 1907–17.

Verhaegen, F. and Seuntjens, J. [2003]. Monte Carlo modelling of external radiotherapy photon beams, *Phys Med Biol* **48**(21): R107–64.

von Wittenau, A. E. S., Cox, L. J., Bergstrom, P. M., Chandler, W. P., Siantar, C. L. H. and Mohan, R. [1999]. Correlated histogram representation of Monte Carlo derived medical accelerator photon-output phase space, *Med Phys* **26**(7): 1196–211.

Walters, B., Kawrakow, I. and Rogers, D. [2002]. History by history statistical estimators in the BEAM code system, *Med Phys* **29**(12): 2745–52.

Walters, B., Kawrakow, I. and Rogers, D. [2005]. PIRS-794 revB: DOSXYZnrc Users Manual, *Technical report*.

Wang, B., Goldstein, M., Xu, X. G. and Sahoo, N. [2005]. Adjoint Monte Carlo method for prostate external photon beam treatment planning: an application to 3D patient anatomy, *Phys Med Biol* **50**(5): 923–35.

Wang, L., Chui, C. and Lovelock, M. [1998]. A patient-specific Monte Carlo dose-calculation method for photon beams, *Med Phys* **25**: 867–78.

Webb, S. [1991]. Optimization of conformal radiotherapy dose distributions by simulated annealing: 2. Inclusion of scatter in the 2D technique, *Phys Med Biol* **36**(9): 1227–37.

Webb, S. [1998]. Intensity-modulated radiation therapy: dynamic MLC (DMLC)

therapy, multisegment therapy and tomotherapy. An example of QA in DMLC therapy, *Strahlentherapie und Onkologie* **174 Suppl 2**: 8–12.

Webb, S. [2004]. Direct aperture optimization for a variable aperture collimator for intensity-modulated radiation therapy, *Phys Med Biol* **49**(5): N47–55.

Wieslander, E. and Knoos, T. [2000]. A virtual linear accelerator for verification of treatment planning systems, *Phys Med Biol* **45**(10): 2887–96.

Williams, P. C. [2003]. IMRT: delivery techniques and quality assurance, *British Journal of Radiology* **76**(911): 766–776.

Yu, C. [1995]. Intensity-modulated arc therapy with dynamic multileaf collimation: an alternative to tomotherapy, *Phys Med Biol* **40**(9): 1435–49.

Yu, C. [2006]. Direct aperture optimization of breast IMRT and the dosimetric impact of respiration motion, *Phys Med Biol* **51**(20): N357–69.

Zakarian, C. and Deasy, J. [2004]. Beamlet dose distribution compression and reconstruction using wavelets for intensity modulated treatment planning, *Med Phys* **31**(2): 368–75.

Zavgorodni, S, Bush, K, Locke, C, Beckham and W [2007]. Vancouver Island Monte Carlo (VIMC) system for radiotherapy treatment planning dosimetry and research, *Radiotherapy and Oncology* **84**.

Zavgorodni, S., Bush, K., Locke, C. and Beckham, W. [2008]. Vancouver Island Monte Carlo (VIMC) system for accurate radiotherapy dose calculations, *Proceedings of 16th International Conference on Medical Physics* .

Zimmerman, J., Korreman, S., Persson, G., Cattell, H., Svatos, M., Sawant, A., Venkat, R., Carlson, D. and Keall, P. [2009]. DMLC motion tracking of moving

targets for intensity modulated arc therapy treatment: a feasibility study, *Acta Oncologica* **48**(2): 245–50.